DESIGN, MODELLING AND SIMULATION OFA WIRELESS PRESSURE SENSOR FOR MEDICAL APPLICATIONS

Thesis submitted in accordance with the requirements of the University of Liverpool for the degree of

Doctor in Philosophy

By

Jianhua Zhai

June 2009

Design, Modelling and Simulation of a Wireless Pressure Sensor for Medical Applications

by

Jianhua Zhai

Abstract

Abdominal aortic aneurysm (AAA) is a common clinical problem which primarily affects people aged over 60. It is a weakening in the wall of the lower portion of the abdominal aorta which can rupture with catastrophic consequences. Current treatment methods of AAA include open surgical repair and endovascular aneurysm repair (EVAR). EVAR has the advantages of being less discomfort, shorter hospital stay and faster recovery of the patients over conventional open surgical repair. However, this approach suffers from problems such as stent-graft migration, endoleaks and stent mechanism breakage, resulting in continued pressurisation of the aneurysm sac and further enlargement and rupture of the aneurysm. Current surveillance techniques for AAA patients undergone EVAR are mainly used to monitor the change of aneurysm diameter. They are invasive, costly and unable to measure blood pressure in a repaired aneurysm sac. Therefore, a less-invasive, inexpensive and more effective surveillance technique needs to be developed.

A passive wireless pressure sensor has been designed in this research. It consists of a planar spiral coil and a capacitor, connected in series to form a resonant circuit. When being placed in a time varying magnetic field, the sensor oscillates electrically at its resonant frequency which is dependent upon the inductance and capacitance of the components. By activating the sensor with magnetic field and monitoring it frequency

changes in response to pressure changes, pressure information can be acquired and the needs of wire connection for power supply and data transmission can be eliminated. Two different sensor structures were investigated in this research. Fabrication processes of these two sensors employing microfabrication techniques were also suggested.

In addition, this research explored the use of magnetoelastic material for pressure sensing. A sensor array made of Metglas^{TM} 2826MB was fabricated and tested. The characteristics of MEMS design process were specified and the comparison of the features and design flows of three MEMS software packages were carried out in this thesis.

CONTENTS

FIGURES

TABLES

Acknowledgments

First of all, I would like to express my sincerest gratitude to my wife Min Su for all of the sacrifices she has made to support my graduate study in the UK. I would not have the courage and strength to deal with the difficulties without her support.

I would also like to thank my supervisor, Prof. Bernard Hon for providing invaluable guidance for this project. I feel most fortunate being his student. With his encouragement, understanding and inspiration, I was able to achieve the objectives of the research project.

Finally, I would like to acknowledge Dr. Thien How, a senior lecturer of clinical engineering at the University of Liverpool, who specialises in endovascular repairing of abdominal aortic aneurysm (AAA), for his valuable advice and assistance. He has spared his precious time for discussions on my project. Many thanks also go to Dr. Yi Huang, a reader of the Department of Electrical Engineering and Electronics at the University of Liverpool, who helped with the measurement of the LC resonant circuit and Dr. Derek Gould, a consultant interventional radiologist, for his invaluable suggestions and clinical advice towards the sensor design.

Chapter 1
Introduction

This chapter briefly introduces two methods for abdominal aortic aneurysm treatment and the motivation of developing an implantable, wireless pressure sensor for the surveillance of abdominal aortic aneurysm patients who have undergone endovascular aneurysm repair. Then the medical requirements for the proposed sensor are specified and the challenges of developing such a sensor system are discussed. Finally, the aim and objectives of this research and the layout of this PhD thesis are presented.

1.1 Overview

The trend of miniaturisation driven by current therapeutic and diagnostic procedures, which address the quality of patients care, has increased the demand for miniature sensors for medical applications. Recently, considerable research efforts have been focused on the investigation of innovative wireless medical sensors, which are minimally invasive and can be implanted in the patient to monitor physical and physiological parameters during normal life activities. Wireless sensing systems are preferred for medical purposes because a wired connection between the implanted sensor and the external detection device

through the skin would result into a high risk of inflammatory response and infection and cause pain and discomfort to the patient.

Since Collins first introduced a miniature pressure sensor for intra-ocular pressure monitoring in 1967, a variety of implantable medical devices have been developed for various biomedical applications [Collins, 1967]. Recent advances in Micro-Electromechanical Systems (MEMS) and wireless sensing technologies are providing new opportunities for high performance miniature sensors to be mass fabricated. The development of passive implantable pressure sensors to monitor cerebral ventricle pressure, intra-ocular pressure and intra-aneurysm pressure wirelessly has been undertaken by various investigators [Yoon et al, 2004; Stangel, 2001; Ohki, 2004].

This thesis presents the design, modelling and simulation of a wireless pressure sensor which has the potential for the monitoring of intra-aneurysm sac pressures in the patients undergoing endovascular repair. The final sensor is based on an inductor–capacitor (LC) resonant circuit, formed by a capacitive pressure sensor in series with an internal planar coil. The aneurysm sac pressure can be remotely measured by monitoring the resonant frequency of the LC resonant circuit due to capacitance change caused by the sac pressure.

1.2 Abdominal Aortic Aneurysm and Treatment

1.2.1 Abdominal Aortic Aneurysm

Aneurysm is the weakening part of an arterial wall which can cause it to bulge, forming a localised dilatation. When the artery has dilated to twice its normal diameter, it is considered to be an aneurysm. One of the most common sites for the development of an aneurysm is in the abdominal aorta, usually below the kidneys. Figure 1.1 shows the positions of a normal aorta and an abdominal aortic aneurysm (AAA). Once an aneurysm forms, it tends to grow progressively and eventually rupture if it is not diagnosed and treated. The rupture of an aneurysm is often fatal and the mortality rate is as high as 90% [Morris et al, 2004]. About 6,000 people die a year in England and Wales due to AAA ruptures [VascularWeb, 2007]. This disease affects primarily the adult male population over 65 years with an incidence of 3-6% [Johnston, 1994; Bengtson et al., 1992].

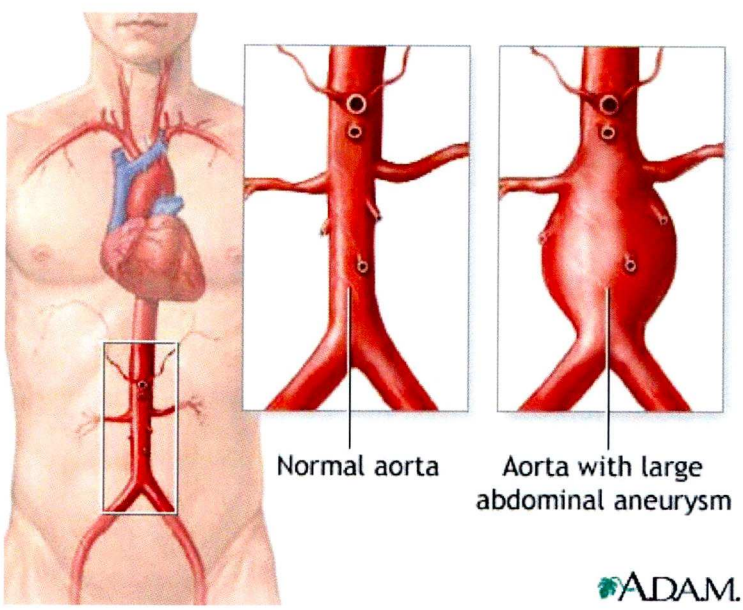

Figure 1.1 Aorta and abdominal aortic aneurysm [MedlinePlus, 2007].

1.2.2 AAA Treatment

Normally AAA needs to be treated when it exceeds 5cm in diameter since the risk of rupture becomes higher than the operative risk [Harthun et al., 2004]. The primary objective of AAA treatment is to prevent the aneurysm from rupture by isolating the aneurysm sac from aortic blood pressure. Current methods of treatment include open surgical repair and endovascular aneurysm repair.

1.2.2.1 Open Surgical Repair

Open surgical repair is the standard procedure for AAA treatment and has been performed routinely for more than 50 years [Dubost, 1951]. In the procedure, a large incision is made in the abdomen or side of the patient to directly visualise the abdominal aorta. Then a fabric tube known as an 'aortic graft' is sewn to the aorta to replace the aneurysm, acting as a replacement blood vessel. Figure 1.2 shows a repaired aneurysm with an aortic graft inside its sac [UCSD, 2007].

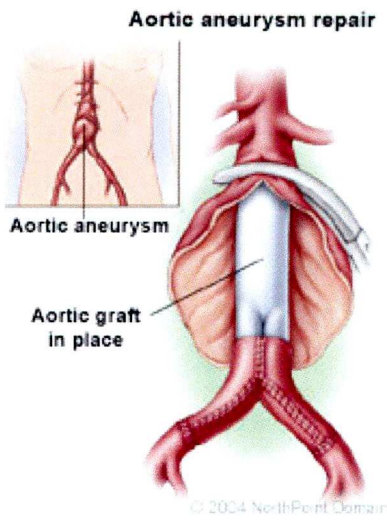

Figure 1.2 Aortic graft and open surgical aneurysm repair [UCSD, 2007].

Open surgical repair is a well-proven surgical procedure and remains in the most common treatment for AAA. However, this approach is a major surgical procedure performed under general anaesthesia and requires stopping of the blood flow through the aorta during the operation. Therefore, it is frequently associated with complications and not all patients can tolerate it. Reports show open AAA repair has an associated 30-day mortality of 4% and can be as high as 14% for high-risk patients [Blankensteijn et al., 2005; Prinssen et al., 2004; Greenhalgh, 2004]. In addition, because large incisions are involved, patients need lengthy hospital stay and recovery time [Rosenberg, 2005].

1.2.2.2 Endovascular Aneurysm Repair

Endovascular aneurysm repair (EVAR) was first introduced in 1990 and has gained widespread popularity as a minimally invasive alternative to open surgical repair. During an EVAR, a small incision is first cut in the femoral artery of the patient. Then a catheter is inserted into the aneurysm sac through the incision. Afterwards a specially designed device known as a "stent-graft", consisting of a metallic stent skeleton and a thin fabric cover, is delivered accurately into the aneurysm sac with the help of x-ray imaging. The graft is then expanded inside the aorta and held in place with metallic hooks presented on the device rather than sutures. The stent-graft seals off the aneurysm and provides a new path through which the blood flows so that the pressure inside the aneurysm sac is relieved and prevented from rupture [Nataraj, 2004; Filipovic et al., 2005].

Figure 1.3 shows the displacement of a stent-graft inside an aneurysm sac [WebBooks, 2007].

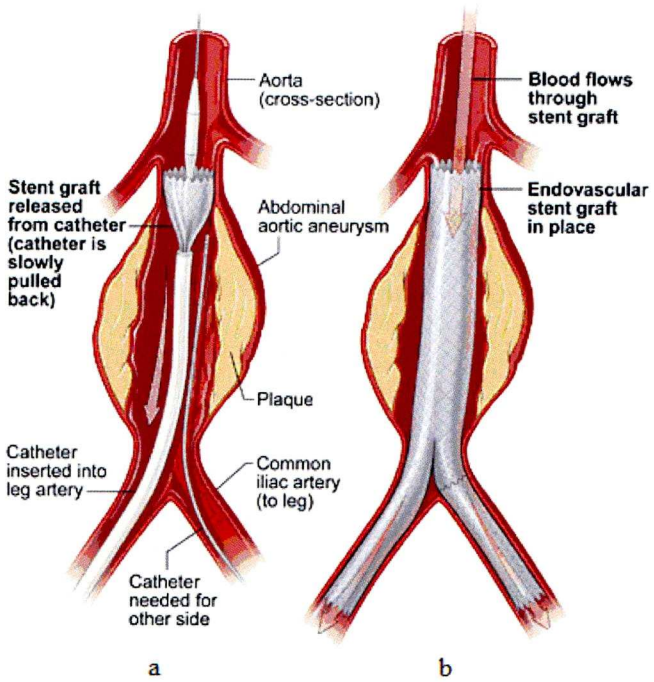

Figure 1.3 The placement of an endovascular stent-graft. (a) catheterization and stent-graft deployment; (b) blood flowing through stent-graft [WebBooks, 2007].

Compared with open surgical repair, EVAR is less invasive and patients need shorter hospital stay and recover faster. Blood loss and need for blood transfusion during the operation are also reduced.

1.2.3 Complication of EVAR

EVAR provides an alternative for AAA patients, especially for patients with significant co-existing medical conditions. However, this treatment approach suffers from problems such as distal migration of stent-graft, which can occur

when the hemodynamic forces exceed the fixation force of the stent graft due to blood pressure and blood flow, breakage of the metallic stent-graft and fabric cover, and endoleak, which is the phenomenon whereby leakage of blood between the stent-graft and the aorta due to inadequate fixation [Carpenter et al., 2001, Fisher et al., 2001, Resch et al., 1999]. These result in continued pressurisation of the aneurysm sac and further enlargement and rupture of the aneurysm. Therefore, patients who have undergone EVAR treatment need lifetime post-operative follow-up to evaluate the stent-graft, aneurysm size and the occlusion of vessels in the treatment area [Rozenblit et al., 2003].

1.2.4 Current Surveillance Techniques and Limitations

Currently, the main follow-up surveillance techniques for AAA patients who have undergone EVAR are computerised tomographic (CT) scan and magnetic resonance imaging (MRI) [Rozenblit et al., 1995; Thurnher et al, 2002; Wolf et al., 2002]. These techniques are used to detect endoleaks as well as monitoring the change if any of the aneurysm diameter. Normally, AAA patients need to have CT scans or MRI two or three times a year. However, both of these techniques have limitations. As CT exposes the patient to ionising radiation and utilises large volumes of contrast agent, which carries a significant risk to allergic patients and patients with impaired renal function, it cannot be repeated frequently. Further more, this technique is not sensitive enough to detect all endoleaks. Schurink reported the presence of increased aneurysm sac pressures even there were no

visible endoleaks on CT exam [Schurink, 1998]. As for MRI, although it is performed without ionising radiation or nephrotoxic contrast media, this procedure is expensive and time consuming. In addition, it is a costly test that requires highly trained staff and the accuracy of this test in detecting stent-graft failure is not well-established [Ohki et al., 2004].

1.2.5 Pressure Monitoring in AAA

The primary goal of AAA treatment is to decrease the aneurysm sac pressure in order to prevent it from rupturing. Both CT and MR angiography are unable to detect blood pressure in an aneurysm sac. Studies demonstrated decreased pressures had been observed in successful excluded aneurysms [Sonesson et al., 2003]. Therefore, it has been speculated that direct measurement of pressure within an excluded aneurysm sac may be the best determinant of a successful repair [Dias et al., 2004]. Previously, in order to acquire the pressure information inside an aneurysm sac, the only way was with direct puncture, which is quite invasive, cumbersome and may cause infection of the aneurysm. Recent advances in remote pressure sensing technology has made it possible to develop an implantable, non-invasive device to take the measurement even at home, without any special preparation and exposing the patient to radiation.

1.3 Medical Requirements for the Proposed Sensor

From a clinical perspective, the proposed wireless pressure sensor should satisfy

the following requirements.

1.3.1 Biocompatibility

The sensor must be compatible to allow long-term implantation. There are strict regulations to ensure the biocompatibility of medical implants, enforced by government organisations such as the Medical Device Agency (MDA) in the UK. Biocompatibility of an implantable wireless sensor should be exhibited from two aspects.

First, the sensor should be biocompatible during the whole life of implantation when it is not in operation. The proposed sensor is expected to remain in the patient for a long period, ideally, the rest of life. Therefore, it must not cause any damage to the body such as inflammation or clots. Also the sensor itself should survive inside the body, which means it should not be affected by the environment in which it is immersed. By choosing appropriate biocompatible sensor material or by coating the sensor with biocompatible material, the sensor long-term compatibility can be achieved. An alternative way is to use encapsulation techniques to separate the sensor from the tissue or liquid it is surrounded by.

Another consideration for sensor biocompatibility is the effect of the signals applied to and generated by the sensor on the tissues in the vicinity of the sensor.

When the sensor receives power or instruction from outside and transmits measured data to an external detection system, it should not disturb normal activities or cause any health hazards to the patient. For example, if the implantable sensor is chosen as an inductor-capacitor resonant type (discussed in Chapter 2 and Chapter 5), the operational frequency of the sensor should be carefully selected in order to avoid problems such as tissue warming or activation of nervous tissue.

1.3.2 Deliverability

The delivery of the proposed pressure sensor should follow two principles: the delivery process should be as simple as possible and should not prolong much of the endovascular procedure; the sensor should be delivered to an appropriate position inside the aneurysm sac so that it can provide a reliable measurement which represents the actual blood pressure inside the aneurysm.

Two approaches can be employed to deliver the proposed sensor. One is to fix the sensor onto the outside lumen of the stent-graft and have it delivered at the same time as the stent-graft deployment. Another approach is to deliver it immediately after the endovascular procedure. Figure 1.4 suggests a possible delivery method in which a guide wire is used to assist the positioning of the implantable pressure sensor onto the outside lumen of the stent-graft. Approach one is compatible with the present endovascular treatment method and does not

need additional delivery procedure. A drawback is that it is difficult to adjust its position when it is necessary. The second approach will inevitably delay the endovascular procedure and a special designed delivery system is needed. However, adjusting the position of the sensor would be much easier.

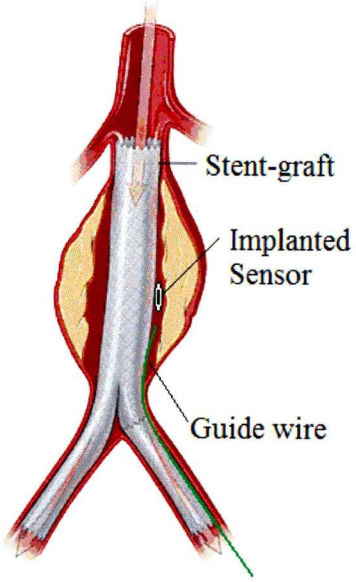

Figure 1.4 The delivery of an implantable pressure sensor using a guide wire.

1.3.3 Miniaturisation

The sensor needs to be miniaturised to minimise the interference with medical procedures and the normal activities of the patient. As discussed in Section 1.3.2, the sensor should be placed inside the aneurysm sac but outside the lumen of the stent-graft. Normally, only an AAA larger than 50mm in diameter needs treatment. A stent-graft is available from about 22 to 36mm in diameter. Therefore, the width of the pressure sensor can be chosen to be larger than 10mm. However, because the sensor is placed in position through a femoral artery of the

patient, the maximum width of the sensor must be less than the diameter of the femoral artery through which the device is delivered. From clinical advice (Dr. Thien How, from Department of Clinical Engineering, University of Liverpool and Dr. Derek Gould, from Department of Interventional Radiology, Royal Liverpool University Hospital) and taking into account the actual size of a squeezed stent-graft during its delivery process, the maximum width and length of the sensor were determined to be less than 6mm and 10mm, respectively.

1.3.4 Sterilisability

The sensor will need to endure at least one of the existing standard sterilisation methods to protect the patient. Common sterilisation techniques include wet heat, dry heat, ethylene oxide and irradiation. However, the chosen sterilisation method will restrict the materials and construction techniques that can be used in the device. For instance, dry heat sterilisation is not generally regarded as a suitable method for polymers because of the low thermal transmission properties. In addition, most polymers will degrade during prolonged dry heat sterilisation or after exposure to gamma radiation.

1.3.5 Pressure Measurement Range

The sensor must be able to measure the blood pressure of the patient. The normal blood pressure is 120mmHg (systolic) /80mmHg (diastolic) [Vaughn, 2007]. High blood pressure is defined as 140/90mmHg. For patients suffering from

hypertension, this can be as high as 210/120mmHg. Some may even reach 250mmHg systolic pressure. Considering safety factor and some special occasions such as diving, the sensor should measure pressure range from 0 to 350mmHg relative to atmospheric pressure.

1.3.6 Other Requirements

In order to achieve long-term implantation with high performance, the pressure sensor to be developed also needs to exhibit the following characteristics:

- Ability for real-time, continuous monitoring;
- Ability to frequently repeat measurements;
- Long-term stability and accuracy;
- Robust wireless data communications with external interrogating/receiving system;
- Minimal interference with other medical devices.

1.4 Research Challenge with Power Supply

Although there are many challenges for developing such a sensing system which exhibits the above characteristics, the major problem remains the power supply requirement. An implanted sensor requires some form of energy to operate. This energy is used for operating the sensor, processing the information and data communication.

There are three possible options to supply power to the implanted unit. The first one is to use wires to connect the sensor with an external power source and signal recording device. However, this approach would not be acceptable for long-term monitoring as there is high risk of infection at the site where the wires pass through the skin. It is therefore important that the whole sensor system is entirely implanted in the aneurysm sac.

The second option is to integrate a power supply to the sensor, such as a battery. For medical applications, an implanted sensor is expected to remain in operation for several years, ideally, the whole life of the patient. However, because of the small overall physical size of the pressure sensor, no existing technology can be employed to develop such a small battery to operate for a sufficiently long period inside the body. Furthermore, it is impractical to replace the battery because of the restriction of medical procedures and the associated risks. The feasibility of using battery for the power supply will be discussed in detail in Chapter 2.

The third option for power supply is an external wireless power source. However, the small physical size and the absence of wires have narrowed the options for an efficient and sufficient wireless power supply. Wireless power supply techniques for a medical implant will be reviewed in Chapter 2.

Another constraint with regard to power supply in implanted medical sensors is

the dissipated heat from using the power. The sensor needs to consume energy as low as possible to avoid generating excessive heat to damage the tissue surrounding the sensor.

1.5 Research Aim and Objectives

The overall aim of this research project was to design a wireless pressure sensor which can be used for the continuous measurement of aneurysm sac pressure variations after an EVAR as well as wireless information transmission. The research had two major objectives:

- To design, model and simulate an implantable, non-invasive wireless pressure sensor element for long-term monitoring of patients;
- To analyse the sensor performance based on the designed model.

1.6 Layout of the Thesis

The thesis consists of seven chapters:

Chapter 1 introduces current treatment methods for abdominal aortic aneurysm and the desire to develop a wireless pressure sensor for pressure monitoring after an endovascular aneurysm repair. Then the feasibility and requirement for developing such a sensor is specified.

Chapter 2 presents a literature review on wireless power supply and wireless data communication techniques in a medical implant system. Three types of wireless

pressure sensors based on different principles, including inductor-capacitor resonant circuit, magnetostrictive effect and surface acoustic wave, are reviewed. At the end of this chapter, Micro-Electro-Mechanical Systems (MEMS) and its future market are briefly introduced. Some commonly used micro-fabrication techniques are reviewed.

Chapter 3 explains the working principle of magnetoelastic sensors. A pressure sensor array was developed and tested.

Chapter 4 introduces the features of MEMS design process and three leading software packages for MEMS products modelling and simulation: CoventorWare, IntelliSuite and MEMS Pro.

Chapter 5 deals with the design and modelling of the wireless pressure sensor employing inductor-capacitor (LC) resonant frequency technology. Design considerations of the coil and the capacitor are presented.

Chapter 6 suggests the fabrication process of the LC resonant frequency type pressure sensor. These include coil and capacitor fabrication processes as well as final bonding process. Two experiments were performed to verify the feasibility of the sensor detection.

Chapter 7 summarises the results, discusses limitations and gives recommendations for future work.

References

Bengtsson H., Bergqvist D. and Sternby N. H., Increasing prevalence of abdominal aortic aneurysms, *European Journal of Surgery*, 1992, 158:19-23.

Blankensteijn J. D., et al., Two-year outcomes after conventional or endovascular repair of abdominal aortic aneurysms, *N Engl J Med*, 2005, 352: 2398-405.

Carpenter J. P., Neschis D. N., et al, Failure of endovascular abdominal aortic aneurysm graft limbs, *European Journal of Vascular and Endovascular Surgery*, Volume 21, Issue 6, June 2001, pp. 520-528.

Collins C., Miniature passive pressure transensor for implanting in the eye, *IEEE Trans. Biomed. Eng.* BME-14(2), 1967, pp. 74-83.

Dias N.V., Ivancev K., et al., Intraaneurysm sac pressure measurements after endovascular aneurysm repair: differences between shrinking, unchanged, and expanding aneurysms with and without endoleaks, *J Vasc Surg 2004*, 39:1229–35.

Dubost C., Allary M. and Oeconomous N., Treatment of aortic aneurysm; removal of the aneurysm; re-establishment of continuity by grafts of preserved human aorta, *Mem Acad Chir (Paris)*, 1951, 77: 381-83.

Filipovic M., Goldacre, M. J., et al., Trends in mortality and hospital admission rates for abdominal aortic aneurysm in England and Wales, 1979-1999, *Br J Surg 2005*, 92 : 968-75.

Fisher R. K., How T. V., et al, Harnessing Hemodynamic Forces for the Suppression of Anastigmatic Initial Hyperplasia: the Rationale for Rebuffed Grafts, *European Journal of Vascular and Endovascular Surgery*, Volume 21, Issue 6, June 2001, pp. 520-528.

Greenhalgh R. M., Brown L. C., et al, Comparison of endovascular aneurysm repair with open repair in patients with abdominal aortic aneurysm (EVAR trial 1), 30-day operative mortality results: randomised controlled trial, *Lancet*, 2004, 364:843-848.

Harthun N. L., Prevalence of abdominal aortic aneurysm and repair outcomes on the basis of patient sex : Should the timing of intervention be the same ? *The Journal of Thoracic and Cardiovascular Surgery*, 2004, 127:325-8.

Johnston K. W., Influence of sex on the results of abdominal aortic aneurysm repair, *Journal of Vascular Surgery*, 1994, 20:914-23.

MedlinePlus,
website: http://www.nlm.nih.gov/medlineplus/ency/imagepages/18072.htm,
accessed in December 2007.

Morris L., et al., A mathematical model to predict the in vivo pulsatile drag forces acting on bifurcated stent grafts used in endovascular treatment of abdominal aortic aneurysms (AAA), *Journal of Biomechanics 37* (2004), pp. 1087-1095.

Nataraj V., Endovascular abdominal aortic aneurysm repair, *Continuing Education in Anaesthesia, Critical Care & Pain*, Volume 4, No. 3, 2004, pp. 91-94.

Ohki T., Stern D., Allen M., and Yadav J., Wireless Pressure Sensing of Aneurysms, *Endovascular Today*, April 2004, pp. 47-52.

Prinssen M., Verhoeven E. L., et al, A Randomized Trial Comparing Conventional and Endovascular Repair of Abdominal Aortic Aneurysms, *The New England Journal of Medicine*, 2004, 351:1607-1618.

Resch T. and Ivancev K., Distal migration of stent-grafts after endovascular repair of abdominal aortic aneurysms, *Journal of Vascular and Interventional Radiology*, 1999, Vol. 10, Issue 3, pp. 257-264.

Rosenberg B. L., Endovascular abdominal aortic aneurysm repair is more profitable than open repair based on contribution margin per day, *Surgery*, March 2005, 137: 285-92.

Rozenblit A. and Marin M. L., Endovascular Repair of Abdominal Aortic Aneurysm: Value of Postoperative Follow-up with Helical CT, *American Journal of Radiology*, 1995, 165:1473-1479.

Rozenblit A. M. and Patlas M., Detection of Endoleaks after Endovascular Repair of Abdominal Aortic Aneurysm: Value of Unenhanced and Delayed Helical CT Acquisitions, *Journal of Vascular and Interventional Radiology*, 2003, 227:426-433.

Schurink G. W. and Aarts N. J., Wilde J., et al., Endoleakage after stent graft treatment of abdominal aneurysm: implications on pressure and imaging—an in vitro study, *J Vasc Surg. 1998*, 28:234-241.

Sonesson B., Dias N., Malina M., et al., Intra-aneurysm pressure measurements in successfully excluded abdominal aortic aneurysm after endovascular repair, *J*

Vasc Surg. 2003; 33:733-738.

Stangel K., et al, A Programmable Intraocular CMOS Pressure Sensor System Implant, *IEEE Journal of Solid-State Circuits*, Vol. 36, July 2001, pp. 1094-1100.

Thurnher S. and Cejna M., Imaging of aortic stent grafts and endoleaks, *Radiol Clin North Am*, 2002, 40:799-833.

UCSD, University of California, Medical Centre, Interventional Radiology, Website: http://www.ucsd.vasculardomain.com/handler.cfm?event=practice,template&cpid=5815, accessed in October 2007.

VascularWeb, provided by the Society for Vascular Surgery, website: http://www.vascularweb.org/_CONTRIBUTION_PAGES/Media/What_Is_Vascular_Disease.html, accessed in March 2007.

Vaughn Aubuchon, website: http://www.vaughns-1-pagers.com/medicine/blood-pressure.htm, accessed in August 2007.

WebBooks, website: http://www.web-books.com/elibrary/medicine/Cardiovascular/Aneurysm_Treatment.htm, accessed in May 2007.

Wolf Y. G., Tillich M., et al., Changes in aneurysm volume after endovascular repair of abdominal aortic aneurysm, *Journal of Vascular Surgery*, 2002, 36:305-9.

Yoon H. J., et al, Micro devices for a cerebrospinal fluid (CSF) shunt system, *Sensors and Actuators*, A110(2004), pp. 68-76.

Chapter 2
Literature Review

This chapter surveys literature on wireless power supply and data communication techniques. Three types of wireless pressure sensors based on different technologies are described including inductor-capacitor resonant, passive surface acoustic wave, and magnetoelastic thick-film pressure sensors. In addition, MEMS and its future market, as well as some micro-fabrication techniques are briefly introduced at the end of this chapter.

2.1 Wireless Power Supply Methods

A medical implant needs power in order to perform its functions. For the proposed sensor, the power is used to detect the aneurysm pressure and to transmit the measured data to the outside world. A cable connection between a medical implant and an external measurement system is not advisable because of the risk of infection at the site where the cable passes through the skin. However, wireless power supply is a major challenge for any implantable medical device. The employment of an active transponder system which contains a power supply such as batteries has the limitation of lifetime issue of the implant, especially when the implant is required to be of small size to suit medical procedures. An

example is a sensor in the eye to detect intraocular pressure. The maximum allowable physical size for this sensor is approximately 4mm×4mm. It would be impractical to integrate a battery into the sensor by employing existing technologies.

The provision of power for medical implants can be divided into two categories. One is that the required power is generated by the implant itself. The movement of the body or the mechanical vibration of the body part where the implant is to be embedded can be used to generate the required power. Several researchers have reported the generation of power utilising kinetic energy from movement [Williams, 1996; Meninger, 2001; Sterken, 2002]. Another method is that the power is delivered from outside wirelessly. Magnetic fields and optical sources are the two common methods for remote power delivery [Suzuki, 1999; Sakakibara, 2001; Lam, 2003].

Ijntema described seven techniques which have the potential to generate power for an implantable eye pressure sensor. These techniques are shown in Figure 2.1 [Ijntema, 1992]. The first method is to utilise the vibrations of the eye called tremors to generate electrical energy. These vibrations have a frequency of about 80Hz and amplitude of 1-2μm. As shown in Figure 2.1.1, a membrane with a fixed positive charge is placed parallel near an electrode with a fixed negative charge. The membrane vibrates due to the eye tremors. This vibration generates a

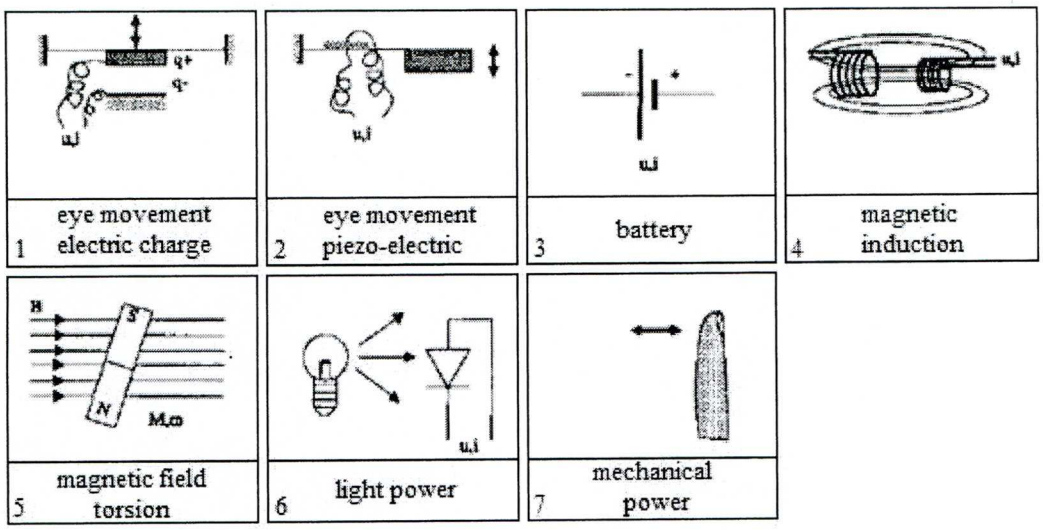

Figure 2.1 Possible power sources for an implantable eye pressure regulator [Ijntema, 1992].

current and a voltage, which can be accumulated in a capacitor in the form of electrical energy. The second approach also employs the vibrations of the eye. However, as shown in Figure 2.1.2, a thin layer of piezoelectric material is used to transform this mechanical energy (vibration) into an electrical energy. In Figure 2.1.4, the energy transfer is accomplished by means of two coupled coils. Figure 2.1.5 shows that mechanical power can be cordlessly generated through torsion produced by a magnet in a magnetic field. The employment of photodiode to transform the light energy into electrical energy is shown in Figure 2.1.6. In Figure 2.1.7, mechanical power is produced by pressing a button in the eye with a finger to close or open a valve in the eye pressure regulator.

Acquiring power from a light source needs optically transparent environment which is not available in the case of AAA as the proposed pressure sensor is

embedded deep inside the body. The energy generated from motion still needs to be transferred wirelessly into the body. It is also unclear whether the other techniques described above can reliably generate the amounts of energy required.

Other references also suggested the use of infrared (IR) signal or fuel cells powered by one of the biological energy metabolism cycles [Uno et. al, 1997; Lam, 2003; Lam, 2006]. However, IR is also bound by line of sight; that is, the receiver must be visible to the transmitter. Biochemical fuel cells would be an ideal power source for a device implanted within a biological organism, but this technique remains a long-term goal and is not a practical alternative for medical implants at present. Therefore, wireless power delivery through magnetic fields offers the most attractive solution for our AAA pressure sensor unit.

2.2 Wireless Pressure Sensing Techniques

Pressure sensor generally relies on the measurement of the deflection of a flexible diaphragm when subjected to pressure. The deflection of the diaphragm which is related to the applied pressure can be determined directly using capacitive or optical approaches [Akar, 2001; Atkins, 1995]; or indirectly using piezoresistive or resonant techniques to measure the change of resistance or frequency caused by the displacement [Søndergård, 1996; Eklund, 2000]. However, as described in the previous chapter, implantable wireless pressure sensors impose additional requirements for energy supply and signal processing,

which emphasize the needs for the elimination of a physical connection to power source and data acquisition equipment.

The survey of literature shows that three different technologies can be employed for the development of the implantable pressure sensor. They are inductor-capacitor (LC) resonant, passive surface acoustic wave (SAW), and thick-film magnetoelastic pressure sensing technologies [Dehennis, 2005; Clasbrummel, 2004; Grimes, 1999]. The operational principles of these technologies and suggested sensor structures will be presented in the following sections. Because this research is focused mainly on LC pressure sensors, more details of this technique will be presented in terms of the sensor structures from previous researchers.

2.2.1 Inductor-Capacitor Resonant Pressure Sensor

Inductor-capacitor (LC) resonant pressure sensors have been suggested by a number of researchers for miniature and long-term implant systems [Rosengren, 1994; Stangel et al., 2001]. The main advantage of LC resonant sensor is its high resolution. Pressure sensitivity as high as 120kHz/mmHg was reported in literature [Akar, 2001]. Other advantages include low temperature sensitivity, simplicity in structure and wide pressure measurement range.

Inductively coupled coils are the critical components in a wireless LC resonant pressure sensing system. Wireless energy transferring in inductively coupled coils is accomplished by means of the mutual inductance between these coils. Figure 2.2 shows the principle of inductive coupling. When an AC current flow through the primary coil, it generates a magnetic field. The magnetic field induces a current in the secondary coil and can be used to operate a connected implant.

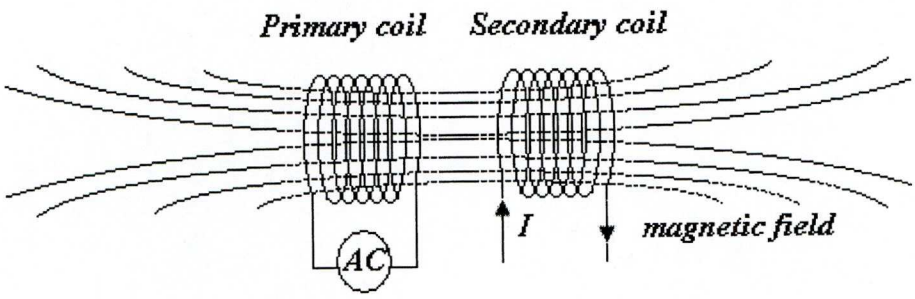

Figure 2.2 Energy transfer in RF Inductively coupled coils.

2.2.1.1 The Principle of Operation

An LC resonant sensor consists of a capacitor connected in parallel with an inductor as shown in Figure 2.3. It oscillates electrically at its resonant frequency which is dependent upon the capacitance and inductance of the components. The characteristic resonant frequency of an LC circuit is given by the following equation [Akar, 2001]:

$$f = \frac{1}{2\pi}\frac{1}{\sqrt{LC}} \tag{2.1}$$

where L is the inductance of the coil and C is the capacitance of the capacitor.

The resonant frequency of an LC resonant pressure sensor varies because of the change of capacitance of the capacitor. This capacitive change could be a result of changes in dielectric properties or geometric changes, which result from the changing pressure. By remotely sensing this resonant frequency, this pressure information can be determined.

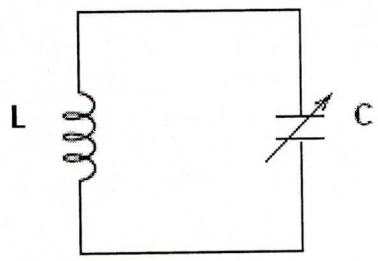

Figure 2.3 An LC resonant circuit.

2.2.1.2 Different Structures of LC Medical Pressure Sensor

The first implantable medical sensor based on LC resonant principle was suggested by Colins [Colins, 1967]. It was intended for implantation in the eye. However, the long-term stability of this sensor was poor [Van Schuylenbergh, 1996].

Rosengren and colleagues described an implantable sensor for intraocular pressure measurement [Rosengren, 1992]. The sensor structure and its resonant frequency response are shown in Figure 2.4. It consists of a micro-fabricated pressure-sensitive capacitor, which is formed by two silicon wafers, and a small hand-wound coil. One of the wafers is covered with 1.0μm thick SiO_2 as an

insulating layer. The diameter of the coil is 4mm and it has 10 turns which is fabricated using a 50μm diameter gold wire insulated with silicon rubber. The gap between two electrodes is 10μm. The sensor was designed to measure pressure range of 0-250mmHg.

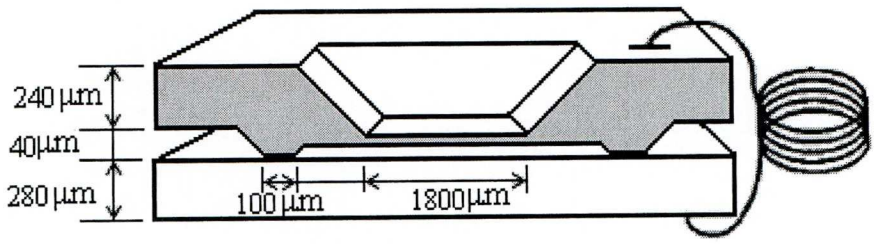

Figure 2.4 An intraocular pressure sensor and resonant frequency response [Rosengren, 1992].

Rosengren stressed that the purpose of the research was to demonstrate the feasibility of this particular sensor structure in terms of the overall performance. Several achievements have been made including sensor long-term stability and high linearity. The problem of creep and different thermal expansion is also avoided as a result of using the same material for the entire sensor structure. However, this prototype suffers from a high stray capacitance which resulted in poorly controlled pressure sensitivity. This is due to the thin SiO_2 layer between the two electrodes. The quality factor Q (see page 121, §5.3.1.2) of the sensor is only 5.5, owing to the high series resistance contributed by the support wafer. The low Q value makes it difficult to detect the resonant frequency which restricts its practical use. Another problem is the low pressure sensitivity which

results from the relatively large gap between the two electrodes of the capacitor. In order to solve these problems, Rosengren later optimised the design by increasing the resistivity of the top silicon wafer and decreasing the resistivity of the pressure sensing diaphragm [Rosengren, 1994]. It was aimed to have the overall impedance dominated by the capacitance of the air gap between the diaphragm and the bottom wafer. A significant improvement was achieved in terms of the sensor quality factor (Q>100) according to his report.

Akar developed a wireless capacitive pressure sensor for implantable medical applications [Akar, 2001]. Figure 2.5 shows the structure and the electrical equivalent circuit of this sensor.

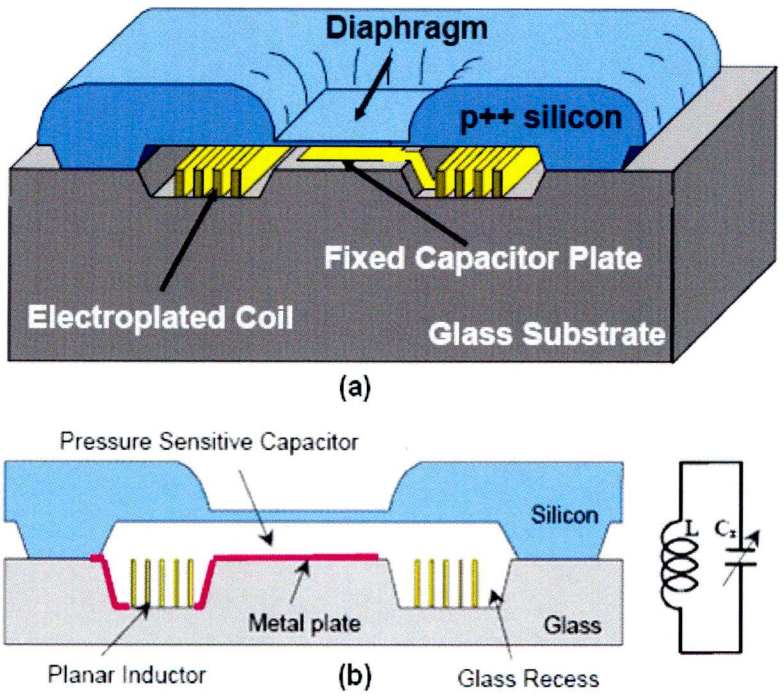

Figure 2.5 Schematic of a wireless pressure sensor. (a) Sensor structure; (b) cross-sectional view and its electrical equivalent circuit [Akar, 2001].

The complete sensor measures 2.6mm×1.6mm in size and incorporates a 24-turns gold-electroplated coil that has a measured inductance of 1.2μH. It consists of a boron-doped silicon diaphragm and a glass substrate connected together by anodic bonding. The diaphragm has a thickness of 6μm and is suspended over the glass by two anchors. It is electrically conductive and acts as the upper electrode of the capacitor. The glass substrate is etched to form the pressure reference cavity. An adhesive layer followed by a gold layer are deposited and patterned to form the planar coil and the lower electrode. The gap between the two electrodes is only 2μm in order to obtain high sensor pressure sensitivity. The sensor was designed to measure the pressure range of 0-50mmHg. The expected corresponding resonant frequency responses were 103-95MHz with a pressure sensitivity of 160kHz/mmHg. The actually measured values were 76-70MHz and the pressure sensitivity was 120kHz/mmHg.

The major advantage of this sensor configuration is that the capacitor and the coil are integrated on the same chip. There is no need for lead transferring from the cavity to outside. Therefore, batch fabrication of the sensor can be realised at the wafer level. Another advantage is that the sensor does not need a special package because the sensor is self-hermetically sealed.

Puers described an intraocular pressure sensor with the similar structure as Akar's design (Figure 2.6) [Puers, 2000]. The overall size of the sensor is

4mm×4mm×0.7mm. It consists of two silicon wafers which are coated and patterned with copper to form the inductor component as well as the capacitor component of an LC circuit. The pressure-sensitive diaphragm is etched with a boss in the centre to increase the linearity of pressure response.

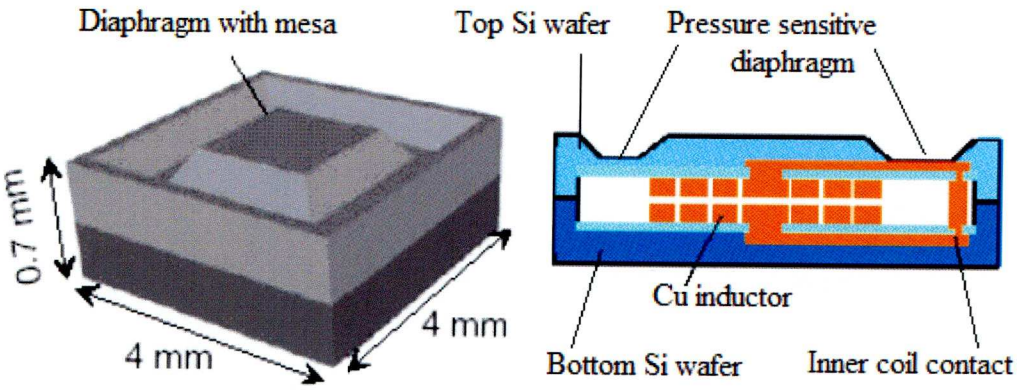

Figure 2.6 A passive LC resonant pressure sensor [Puers, 2000].

The advantage of this structure is that the sensor can be fabricated in a compact size with high quality factor. However, one problem is that the inductance of the coils does not remain constant and changes with increasing pressure. Therefore, the resonant frequency shift of the sensor is not only the result of capacitive changes but also the result of inductive changes. In order to make the sensor of practical use, the capacitance change of the capacitor due to pressure change needs to be designed to dominate the performance of the sensor.

Fonseca reported two types of flexible pressure sensors which were intended for acute and chronic use in AAA pressure wireless measurement [Fonseca, 2006].

The purpose of making the structure flexible is to be able to roll or fold the sensor into a compact shape as required by the catheter-based delivery process. Figure 2.7 shows the delivery system and the rolled and unrolled shapes of the sensor for the delivery.

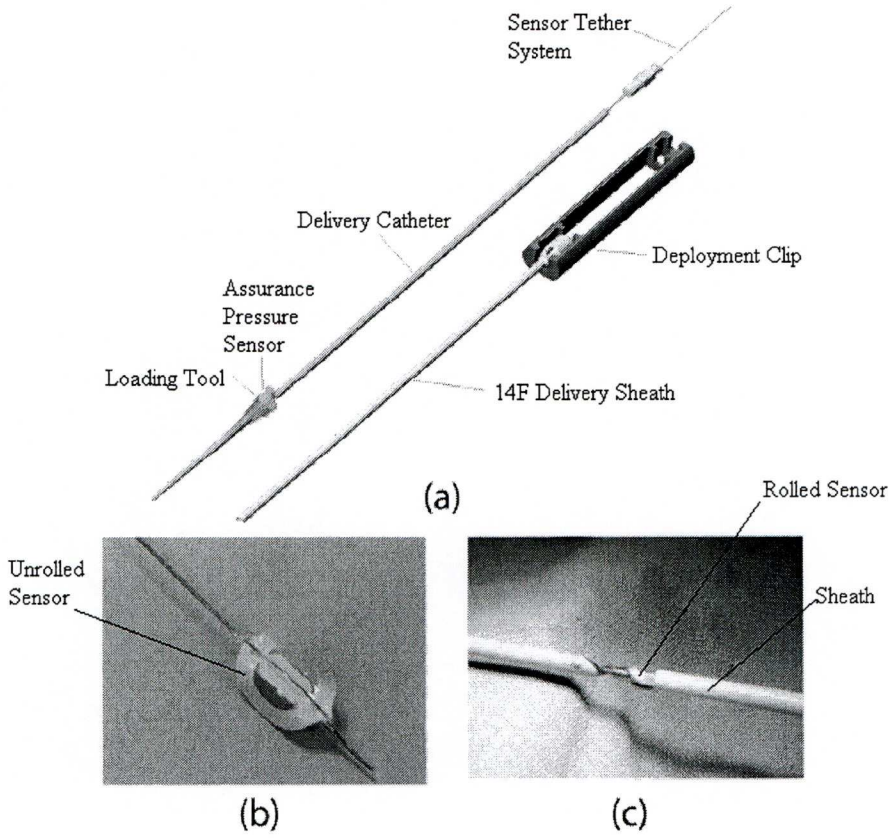

Figure 2.7 Sensor delivery system. (a) Schematic of delivery system; (b) sensor on tether; (c) sensor rolled up into sheath prior to implantation [Fonseca, 2006].

The sensor structure designed for acute use is shown in Figure 2.8. It was fabricated from laminated sheets of copper-clad Liquid Crystal Polymer (LCP) and expanded polytetrafluoroethylene (PTFE)-based inner bonding layer. The diameter of the sensor is about 8mm. Two spiral planar coils were fabricated from the copper-clad LCP layers through standard lithography and wet-chemical

etching process. Each coil has 12 turns with a line width of 60μm, line thickness of 18μm, and line spacing of 80μm. After cutting with laser, the PTFE inner bonding layer was assembled and laminated with the two LCP layers to form the pressure sensor.

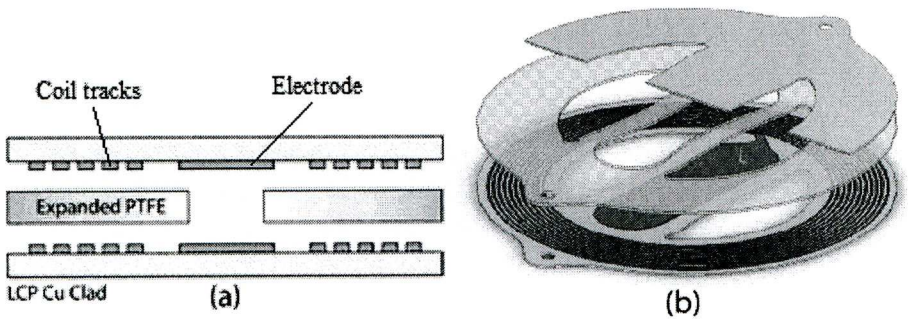

Figure 2.8 Sensor lay up for acute use. (a) Cross-sectional view and (b) perspective view of the LCP sensor design [Fonseca, 2006].

The sensor designed for chronic use has the same physical dimensions as the LCP based sensor. However, the sensor structure and material are different. It was fabricated from PTFE layers and Fluorinated Ethylene Propylene (FEP) copolymer inner adhesive layer (Figure 2.9). A ceramic chamber was used to house the hermetic pressure reference. It was fabricated through the use of sintered layers of zirconia ceramic powders. The gap between the two electrodes is 38μm.

The feature of being flexible makes it possible to realise a larger sensor size so that the readable distance can be increased. Another advantage is that a larger capacitance of the capacitor can be achieved. Therefore, the overall performance

of the sensor can be dominated by the capacitance of the capacitor rather than the parasitic capacitance of the coil. This approach results in a self-packaged structure in which only a polymer outer surface is exposed to the environment.

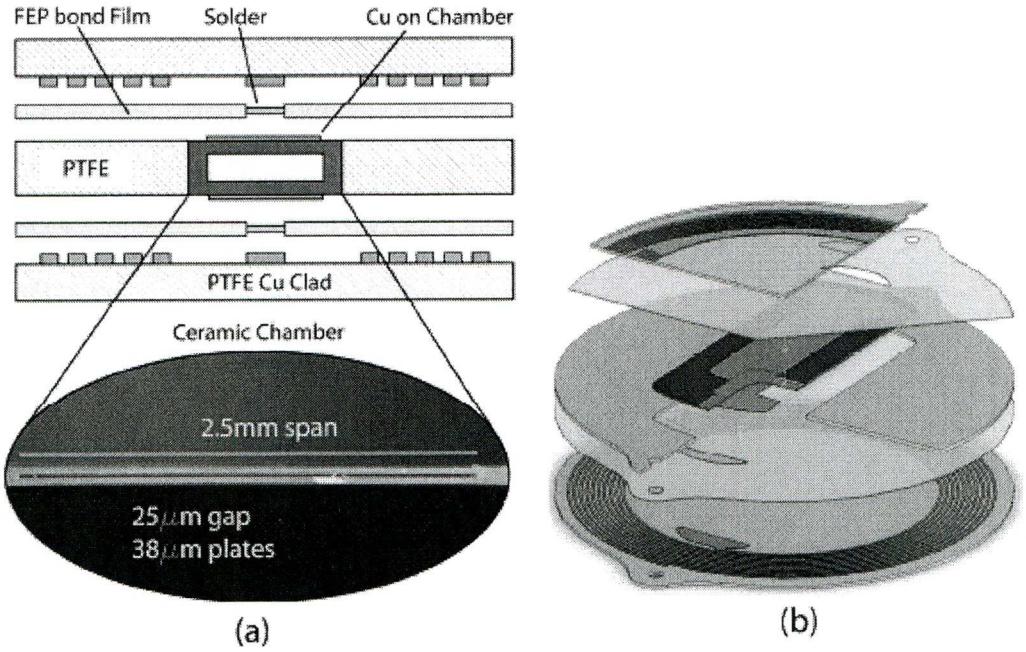

Figure 2.9 Sensor lay up for chronic use: (a) Cross-sectional view; (b) perspective view for the PTFE/Ceramic chamber sensor design [Fonseca, 2006].

However, the pressure sensitivities of these two sensors are relatively low. The linear pressure sensitivities for LCP-based sensor and PTFE-based sensor were found to be between 1 to 20kHz/mmHg and 0.5 to 1.5kHz/mmHg respectively. This is due to the large gap between the electrodes of the capacitors. The LCP-based sensor has the problem of drift and is not suitable for long-term implantation. The sensor for chronic use has higher Q value but lower pressure sensitivity than the sensor intended for acute use, resulting from the increased modulus of the ceramic layer of the pressure sensitive diaphragm.

From literature survey, it shows that the LC resonant circuit is the most common method suggested for wireless pressure sensing inside the human body. One reason for this is because of its relatively simpler structures comparing with other feasible wireless pressuring sensing technologies. This unique feature makes it more suitable for medical implantation purpose than other technologies.

2.2.2 Passive Surface Acoustic Wave Pressure Sensor

Surface acoustic wave (SAW) devices were first used in radar and communication equipment as filters and delay lines [Lewis, 2005]. They have gained widespread popularity in the sensor community over the past 30 years. Sensors for measuring physical, chemical, or biological quantities have been suggested in the literature. Recently, significant progress has been made in passive wireless SAW sensor technology. Innovative passive sensors for the measurement of torque, force, acceleration, humidity, displacement, vibration and acceleration have been developed [Reindl, 2004; Scholl, 1998; Scherr, 1996; Seifert, 1994; Wolff, 1996; Pohl, 1997].

2.2.2.1 Passive SAW Sensors Operation Principle

SAW is a special sound wave that propagates along the surface of an elastic solid. SAW devices usually consist of a polished piezoelectric substrate (e.g., quartz) with metallic structures such as inter-digital transducers (IDTs) and reflectors built on its surface [Pohl, 1998]. The operating principle of a passive SAW

sensor is shown in Figure 2.10.

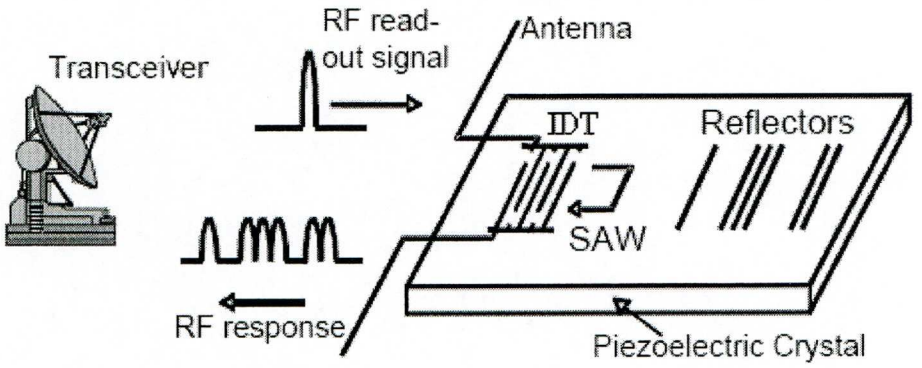

Figure 2.10 Passive SAW sensing principle [Reindl, 2004].

When a RF readout signal is transmitted from a local radar transceiver, it is partially received by the antenna of the passive SAW sensor. Due to the piezoelectric effect, the IDT, which is connected to the antenna, transforms the received RF signal into a SAW. The SAW propagates along the elastic solid surface and is partially reflected back to the IDT by the reflectors placed in the acoustic path. The reflected waves are reconverted into a RF output signal at the IDT because of inverse piezoelectric effect. This RF signal is received by the same transceiver and is analysed [Reindl, 2004].

The wavelength of the SAW is determined by the spacing of the fingers of the IDT, while the propagation speed is determined by the substrate orientation. When physical quantities acting on the piezoelectric substrate varies, the velocity of the SAW is affected by this variation. By measuring the time from the interrogation signal to the response or the time between two or more reflected

signals, this physical quantity can be determined.

2.2.2.2 Passive SAW Pressure Sensor Structures

Passive SAW pressure sensors rely on the detection of variations of the SAW propagation velocity caused by pressure. Therefore, most sensing elements are combined on pressure sensitive diaphragms. Scholl and his colleagues developed a passive SAW pressure sensor which is shown in Figure 2.11 [Scholl, 1998]. The diaphragm of the sensor is made of quartz with 10 reflectors on it as the reflective delay lines. The quartz diaphragm is attached to a quartz cover plate using epoxy adhesive to form a sealed cavity for a reference pressure. The reason to choose a quartz cover-plate is to minimise thermal stress so as to reduce the sensor temperature sensitivity.

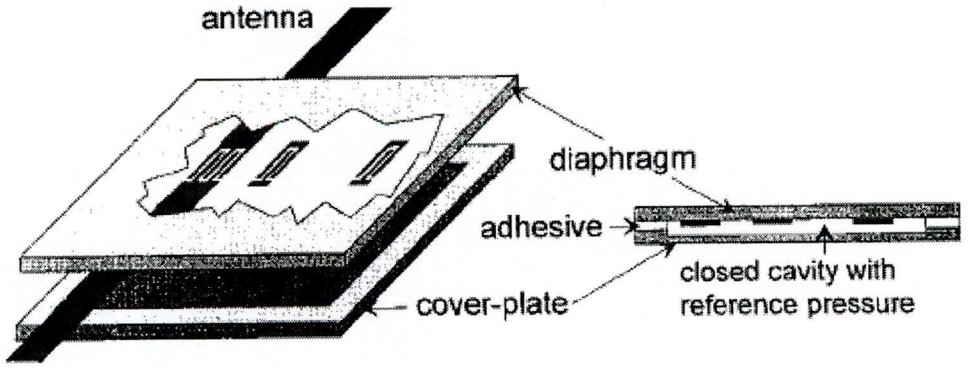

Figure 2.11 Schematic drawing of a SAW pressure sensor [Scholl, 2001].

Buff designed a system using the differential frequency out from two SAW resonators for remote temperature and pressure measurement [Buff et al., 1998].

The two SAW resonators are mounted on a 35° Y cut quartz diaphragm with different SAW propagation directions (Figure 2.12). The two resonators are designed with different resonant frequencies and have a differential frequency of 970 kHz at 0 bar pressure. The use of a dual SAW resonator configuration is to achieve a higher sensitivity and accuracy. An improvement in the system accuracy of 51.5 dB was reported by Buff.

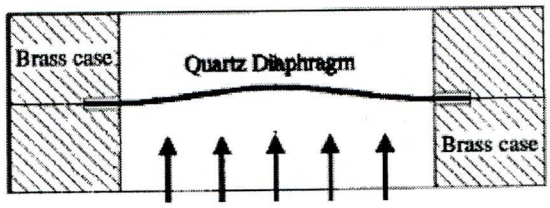

Figure 2.12 A SAW temperature/pressure sensor [Buff, 1998].

2.2.2.3 Advantages and Disadvantages of Passive SAW Sensors

SAW devices have played a key role in consumer electronics such as TV sets or mobile phones. They have also been in practical use for wireless radio frequency identification (RFID) systems for nearly twenty years [Bulst, 2001]. This success is due to their high performance, small size, and good reproducibility.

Passive SAW devices are very compact. This is because SAW can perform signal processing in a physically compressed space. Brocato compared the wavelengths of a RF wave and a SAW with the same frequency travelling through free space and a piezoelectric substrate respectively [Brocato, 2006]. A 3 GHz RF wave propagating in free space has a wavelength of 10cm, while a 3 GHz SAW

propagating in lithiumniobate ($LiNbO_3$) has a wavelength of only 1.16×10^{-4} cm. Therefore, signal processing can be performed efficiently in a very small space in SAW devices. Another advantage of passive SAW sensors compared to conventional telemetry devices is the large readout distance. Distance of several meters had been reported even through non-metallic housings [Scholl, 1998]. In addition, SAW sensors exhibit high stability. This is because they are fabricated on highly stable single crystals, which are robust and show a very slow ageing rate. Passive SAW sensors can be operated in a noisy and harsh environment. These features make them extremely suitable for implantation purposes in medical applications. Researchers in Imperial College and Oxford Brookes University suggested the use of SAW technology for developing an implantable pressure sensor to monitor the AAA sac pressure [Franklin, 2005].

However, passive SAW sensors are not widely used nowadays and their application is restricted to special fields. The main reason is that the SAW propagation path can be affected by a variety of environmental parameters which has been described in the previous section. This means that unwanted environmental variables have to be separated from the parameter to be measured, which is often difficult.

2.2.3 Magnetoelastic Thick-film Pressure Sensor

Some materials change their physical dimensions when subjected to a magnetic

field. This phenomenon is known as magnetostrictive effect. Conversely, a physical deformation of the material will produce a change of magnetisation in the material, namely inverse magnetostrictive effect [Karl, 2000]. Common magnetostrictive materials used for sensing are iron-rich amorphous alloys such as $Fe_{40}Ni_{38}Mo_4B_{18}$ and $Fe_{81}B_{13.5}Si_{3.5}C_2$. These materials have a high magnetoelastic coupling coefficient, as high as 0.98, which allows efficient conversion between magnetic and elastic energies and vice versa [Grimes, 2002]. Magnetoelastic thick-film sensors have attracted the attention of the sensor community during the last decade. Sensors for the measurement of multiple environmental parameters including temperature, pressure, humidity, liquid viscosity and density have been developed [Jain, 2000; Kouzoudis, 2000; Grimes, 2002].

2.2.3.1 Operation Principle

Magnetoelastic sensors are usually made of thin, ribbon-like strips of materials. They mechanically vibrate when placed in a time varying alternating current magnetic field. The characteristic resonant frequency of the vibration f_0 is given by the following equation [Jain et al., 2001]:

$$f_0 = \frac{1}{2L}\sqrt{\frac{E}{\rho(1-\nu^2)}} \tag{2.2}$$

where L is the length of the sensor strip; ρ is the density of the sensor material; ν is the Poisson's ratio and E is Young's modulus of the material. The resonant frequency of a magnetoelastic pressure sensor varies with the change of

its surrounding pressure and the change of frequency can be detected.

2.2.3.2 Detection Methods

The detection of the resonant frequency change of a magnetoelastic sensor can be achieved through different methods. Grimes suggested three approaches to track the resonant frequency shift of a magnetoelastic sensor [Grimes, 2002]. Figure 2.13 shows these approaches of wireless detection. The first approach is to measure the magnetic flux emitted from the sensor. When a magnetoelastic sensor mechanically vibrates in a time varying magnetic field, it emits a time varying magnetic flux because of inverse magnetostrictive effect. This magnetic flux can be detected with a pick-up coil. The second method is to monitor the sound wave generated by the sensor during vibration with a microphone in air or a hydrophone in liquid. Another method of detection is to employ a phototransistor to detect the intensity change of a laser beam which is reflected from the sensor surface. However, as the proposed sensor will be embedded deep in the body, the last two detection methods are impractical in this case.

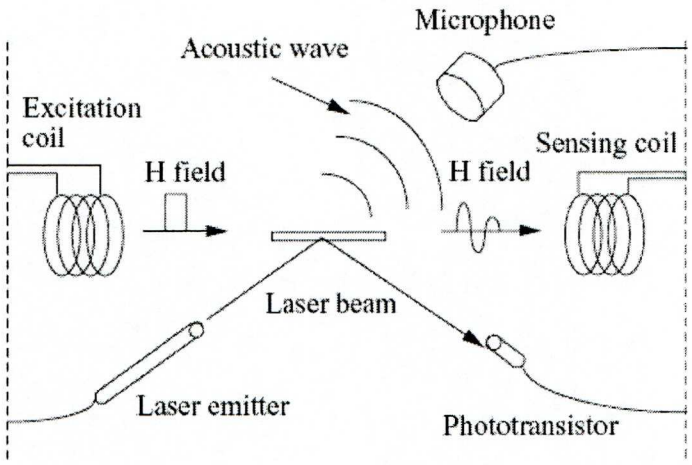

Figure 2.13 Wireless detection methods of magnetoelastic sensor [Grimes, 2002].

2.2.3.3 Pressure Sensor Structures

Grimes developed a magnetoelastic sensor array for simultaneous measurement of temperature, pressure and fluid flow velocity which is shown in Figure 2.14 [Grimes, 2002]. The sensor consists of four sensor elements mounted on a tube at its support tabs. Two of them were made of Metglas^{TM} 2826MB, a commercially available iron-rich alloy, and another two elements were made of Metglas^{TM} 2605SC. The sensors are of slightly different lengths so that their characteristic resonant frequencies do not overlap. For each alloy, one sensor is flat and the other one is curved. The reason for making this configuration is that a flat sensor is insensitive to pressure changes. Therefore, the effect of pressure change can be excluded when measuring other parameters of interests.

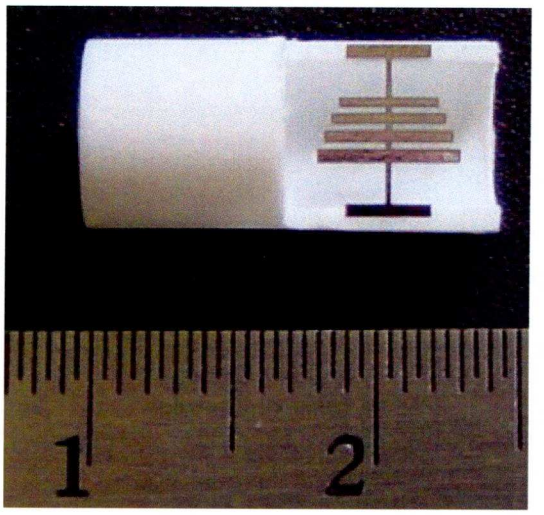

Figure 2.14 A magnetoelastic sensor array [Grimes, 2002].

2.3 Commercial AAA Wireless Pressure Sensors

Currently there are two different types of wireless sensors commercially available for the monitoring of the pressure inside an endovascular-repaired AAA sac. These two sensors use different principles to measure the sac pressure and to transmit the measured data to a detection device which is placed adjacent to the patient. The following section briefly introduces these two products as well as comparing their benefits and drawbacks.

2.3.1 ImPressure

ImPressureTM (Remon Medical Technologies) is the first implantable wireless sensor used for AAA pressure monitoring. It measures 3mm × 9mm × 1.5mm in size. This sensor consists of a piezoelectric membrane and two electrodes which are connected to the membrane to form a capacitor. The piezoelectric membrane can convert ultrasound waves into current for the sensor power supply. It also

senses ambient pressure and generates an ultrasound signal which can be detected by a detection device.

During an endovascular repair operation, the sensor is physically attached to a stent-graft and is delivered to the AAA sac together with the stent-graft. As for the measurement, a hand-held probe is used to send an ultrasonic signal to activate the embedded sensor. The sensor then transmits the sac pressure information out of the body in the form of ultrasonic signals and these signals are picked up by the same probe.

2.3.2 EndoSure

EndosureTM wireless AAA pressure sensor is a product from CardioMEMS. It consists of a micro-coil and a capacitor to form a tuned resonant circuit. Radio frequency rather than ultrasound is used to energise the implanted sensor and transmit the measured pressure information. It has a size of 5mm × 30mm × 1.5mm.

As the sensor is slightly longer and wider than the ImPressrue sensor, it is difficult to attach it to the stent-graft and have it delivered to the AAA sac using the same procedure as the stent-graft. Therefore, a separate delivering procedure has to be required for the implantation.

2.3.3 Comparison of the AAA Pressure Sensors

Ultrasound has been widely used in medical application for many years. It is a very safe technique for the patients when properly used by medical professionals. Ultrasound can easily transverse a fluid environment and soft tissues and therefore is suitable for transmitting measured data out of the body. However, since ultrasound does not travel through air, a contact media such as ultrasonic gel needs to be used between the hand-held probe and the patient's skin. Another drawback of using ultrasound is that it may have difficulties to communicate with the embedded sensor in a patient with calcified AAA sac. This is because ultrasound waves cannot pass through solid objects.

Radio frequency waves can travel through air, liquid and solids. They are frequently used for wireless power and data transmission. However, RF waves can be absorbed by the body and may cause problems such as tissue warming. As the absorption rate of the RF energy increases with the increase of the frequency, the determination of the operating frequency of the sensor is critical for minimising the damage to the tissue and optimising the energy transmission efficiency. Another advantage of using RF technique is that the detection device does not need to directly contact with the patient's body. The measurement can be carried out by the patient at home. The following table (Table 2.1) lists the differences of these two sensors:

Table 2.1 Comparison of the two commercially available AAA pressure sensors

	ImPressure	**EndoSure**
Size	3×9×1.5mm	5×30×1.5mm
Cost	unknown	$3500
Monitoring technology based	Ultrasound	RF
Advantages of technology used	A well-proved safe method for medical applications	RF wave can travel through air, liquid and solids
Disadvantages of technology used	May have problems with fat patients or calcified artery	Tissue warming especially at high radio frequencies
Structural Material	Piezoelectric material	Fused silica, silicone
Quality factor	Not available	50 -90
Delivery process	Delivered at the same time as the Stent-graft	A separate process needed
Measurement location	Hospital	Hospital or home
Sensitivity (kHz/mmHg)	Unknown	5 to 15

2.4 MEMS and Microfabrication Techniques

It was intended to fabricate the pressure sensor using MEMS technology. Hence it is necessary to have some knowledge on MEMS technology and micro-fabrication techniques. The following sections briefly introduce MEMS and its future market as well as some microfabrication techniques which will be used to develop the LC resonant type pressure sensors introduced in Chapter 5.

2.4.1 Introduction to MEMS

MEMS is the acronym of Micro-Electro-Mechanical Systems. It is the integration of mechanical elements, sensors, actuators, and electronics on a common substrate such as silicon, quartz, polymers, plastics or ceramics. MEMS devices claim to be the smallest functional machines currently engineered by

humans [Korvink, 2006]. Their size can range from a few dozen microns to several millimetres.

MEMS technology evolved from microelectronics fabrication technology. Inevitably, many of the MEMS fabrication techniques are 'borrowed' from integrated-circuit (IC) industry [Hsu, 2002]. However, because these techniques are mainly for building two-dimensional electronics while MEMS devices are frequently involved in three-dimensional structures. Therefore, a number of techniques and processes have been specially developed for creating MEMS devices during these years. Examples include surface micromachining, wafer bonding, electroplating, thick-film screen printing, LIGA (a German acronym of Lithographie, Galvanoformung and Abformung, meaning lithography, electroplating, and moulding), deep reactive ion etching and thick photo-resist moulding etc.

MEMS devices are widely used in a number of commercial applications such as RF switches used in mobile communications, sensors that trigger automobile air bags, medical diagnosis and drug dispensing devices, satellite systems, and ink jet printers. The rapid advance in micro-fabrication technologies has enabled many new MEMS products to emerge in the marketplace. According to a report from Yole Development, a leading company in the analysis of the globe MEMS market based in France, the market for MEMS totalled US$48 billion (£24

billion) in 2005 and is expected to top US$95 billion (£47.5 billion) by 2010 [Yole, 2005]. Table 2.2 shows the global markets and forecast for MEMS devices, materials and equipment.

In order to develop the proposed sensor, a deeper knowledge about MEMS and other up-to-date manufacturing technologies is required. The following sections introduce some commonly used MEMS fabrication techniques, materials and manufacturing technologies.

Table 2.2 Global Markets and Forecasts for MEMS Products [Yole, 2005]

Markets	**2005 (US$, Million)**	**2010 (US$, Million)**	**Compound Annual Growth Rate**
MEMS Materials	385	771	15%
MEMS Equipment	631	861	6%
MEMS Devices	5.3	9.9	13%
MEMS Systems	48	95	15%

2.4.2 Basic MEMS Micromachining Process

Similar to the fabrication processes used in IC industry, a conventional MEMS micromachining process comprises of three basic fabrication techniques: deposition, lithography and etching. Deposition, as the name indicates, is the process whereby thin films of material are deposited onto a substrate. In

lithography, a patterned mask is applied on top of the films by lithographic imaging technique. Etching is to remove unwanted materials or layers selectively. A basic MEMS micromachining process is usually a structured sequence of these operations to form actual devices. Figure 2.15 shows the process of a simple MEMS structure fabricated by using these techniques.

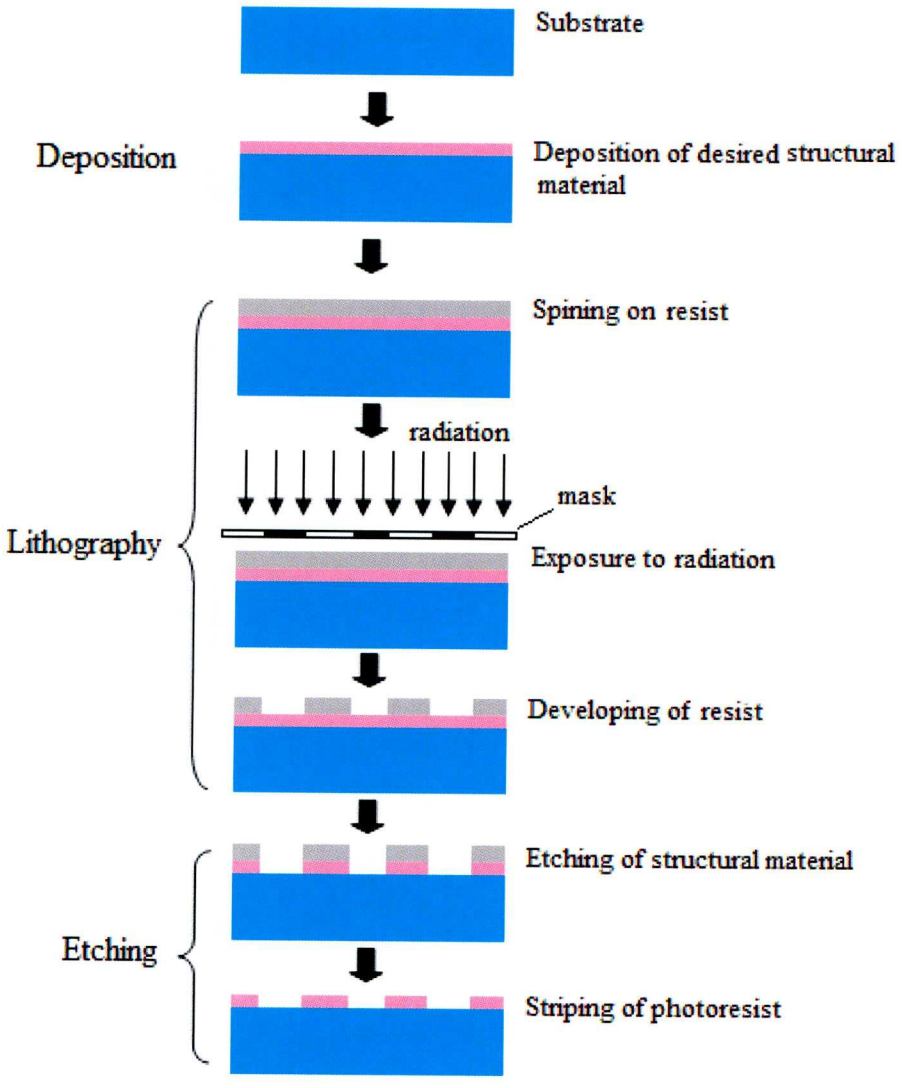

Figure 2.15 Basic MEMS micromachining process.

The process starts from depositing a thin-film of structural material onto a wafer, which is followed by spinning or spraying a layer of material called resist on it. Afterwards, this resist layer is exposed to a radiation source such as x-ray or ultraviolet (UV) light through a pattern-carrying mask. Because resist is radiation-sensitive, it changes its chemical resistance to a certain chemical solution after the exposure. Therefore, the pattern on the mask is transferred to the resist. The wafer is then immersed in the chemical solution to release the pattern. Subsequently, this pattern is etched into the structural thin film using either a wet etching or dry etching technique. Finally, the resist is lifted off. A number of different techniques are used in the deposition and etching processes. Some of the commonly used techniques are introduced in the following sections.

2.4.2.1 Silicon Wet Anisotropic Etching

Solid material exists either in a crystalline state or an amorphous state. Crystalline materials have different properties in different directions while the properties of amorphous materials are almost identical in all directions. Wet anisotropic etching is a process used to etch crystalline materials in desired directions through chemical reactions.

Pure silicon is a single-crystalline material. It has a diamond cubic crystal structure. There are three principal planes in silicon crystal which is shown in Figure 2.16. It can be seen that the angle between plane (100) and plane (110) is

45°. Angle between plane (100) and plane (111) is 54.74°, Directions which are normal to plane (100), (110) and (111) are expressed as <100>, <110> and <111>, respectively. The orientations of silicon wafers are based on these directions.

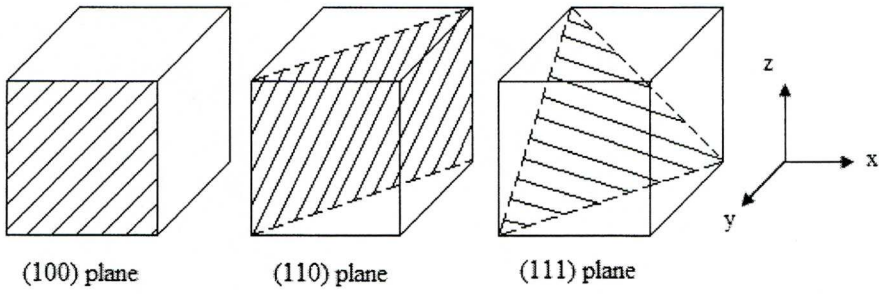

Figure 2.16 Three principal planes on single-crystalline silicon.

Wet anisotropic etching of silicon is one of the key processes in MEMS micromachining. It is also referred to as 'bulk micromachining'. Figure 2.17 shows the plain and cross-section views of a <100> oriented silicon wafer etched by a wet anisotropic etching.

The most common anisotropic etchants used in MEMS industry are potassium hydroxide (KOH), ethylene-diamine mixed with pyrocatechol (EDP), and tetra methyl ammonium hydroxide (TMAH) [Hsu, 2002]. The selection of an anisotropic etchant for a particular silicon wet etching process needs to consider a number of factors. Among them, 'etch rate' and 'selectivity ratio' are the two important parameters. The etch rate is defined as the material thickness etched

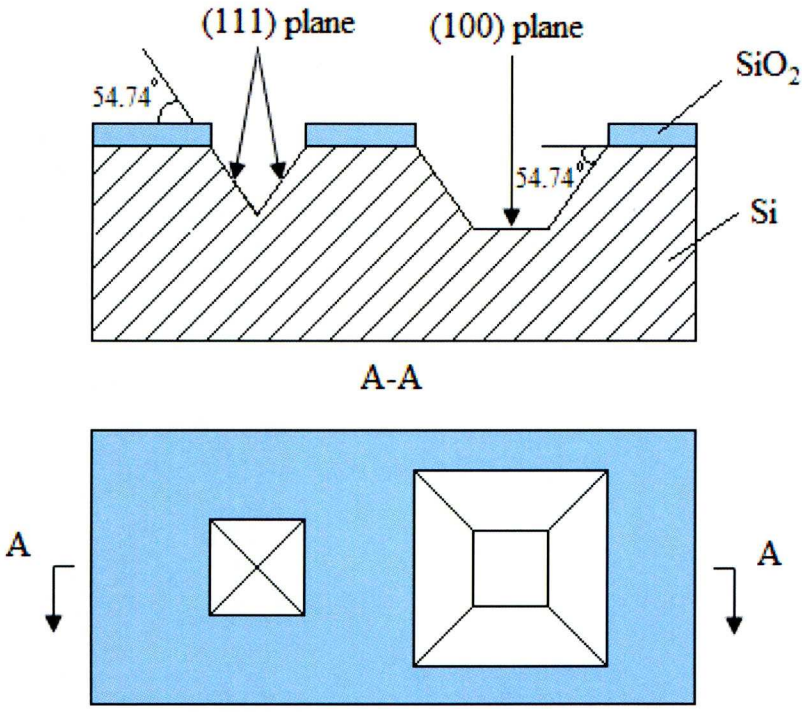

Figure 2.17 The plain and cross-sectional views of a <100> oriented silicon substrate after anisotropic wet etching.

per unit time, while the selectivity ratio is the ratio between the etch rate of the material to be etched and the etch mask material. Table 2.3 gives the etch rates and selectivity ratios of these three etchants. Among these, TMAH has the highest SiO_2 selectivity ratio and KOH has the lowest selectivity ratio. Therefore, in a silicon wet anisotropic etching process, if SiO_2 is used as the etch mask, TMAH is generally the preferred etchant.

Table 2.3 Characteristics of three commonly used etchants [Chollet, 2007]

Solution	**Temp.** (°C)	**Si <100> etch rate** (μm/min)	**SiO_2 etch rate** (nm/min)	**SiO_2 selectivity ratio**
KOH (KOH 44g / H_2O 100ml)	85	1.4	3.5	400
EDP (ethylene-diamine 750ml/pyrocatecol 120g/ H_2O 240ml)	115	1.25	0.5	2500
TMAH (TMAH 28g/ H_2O 100ml)	90	1	0.2	5000

2.4.2.2 Electroplating

Electroplating is the deposition of a metallic layer onto a substrate using electrical current. It is usually employed to form thick films of metals or alloys on substrates.

A typical electroplating process starts from coating a thin seed layer onto the substrate to make it electrical conductive. Because some metal films do not adhere well with the substrates, this seed layer also acts as an adhesive layer which bonds the underlying substrate and the metal layer to be deposited. The substrate is then attached to a negative charge and is immersed into a solution which contains a salt of the metal to be deposited. The metallic ions of the salt carry a positive charge and are attracted to the coated surface of the substrate.

They change to metallic form at the surface after receiving the electrons provided by the negative charge.

Although a number of metals and alloys can be electrodeposited using this technique, the most commonly used metals for MEMS microstructures are nickel, gold, copper and nickel-ferrite alloy [Beeby, 2004(2)]. Copper is used extensively in forming high Q micro-coils because of its high electrical conductivity as well as its wide availability. In addition, copper electroplating is compatible with an IC process which makes it an attractive material for semiconductor industry.

Electroplating is an effective way to deposit thick metal films on silicon substrates. It is inexpensive and is suitable for batch micro-fabrication. The main problem of this technique is that the need of the adhesive seed layer, which is typically formed by a sputtering process, provides a poor step coverage. However, this problem can be solved by an extra surface polishing process.

2.4.2.3 Deep Reactive Ion Etching and Thick-Resist Moulding

In order to obtain a patterned electroplating layer, a mould must be formed on the substrate before electroplating. The mould can be the substrate itself or an applied resist layer which is subsequently wet or dry etched to form the desired

pattern. Deep reactive ion etching and thick resist moulding are the two commonly used techniques for forming moulds with high aspect ratio and near vertical walls.

Aspect ratio is the ratio of height to width of a microstructure. For this research, the metal lines of the coils of the LC resonant pressure sensors (discussed in Chapter 5) need to be constructed with high aspect ratio in order to minimise the series resistance of the coil. Traditional etching process such as chemical wet etching or plasma etching is either unable to build the near vertical sidewalls or the etch rate is relatively low. In the mid 1990s, deep reactive ion etching and thick-resist moulding were developed to overcome these difficulties [Lorenz, 1997; Maluf, 2004]. They have been used to create deep, steep-sided features with high aspect ratio. The following sections will introduce these fabrication techniques.

a. Deep Reactive Ion Etching

Deep reactive ion etching (DRIE) is usually used to create deep trenches and holes on silicon substrates, with aspect ratios up to of 20:1 or more. There are two main technologies for high-rate DRIE known as Cryogenic process and Bosch process. Bosch process is the most common approach currently used, in which a fluoropolymer is used to passivate the etching of the sidewalls. Figure 2.18 demonstrates the principle of the Bosch process.

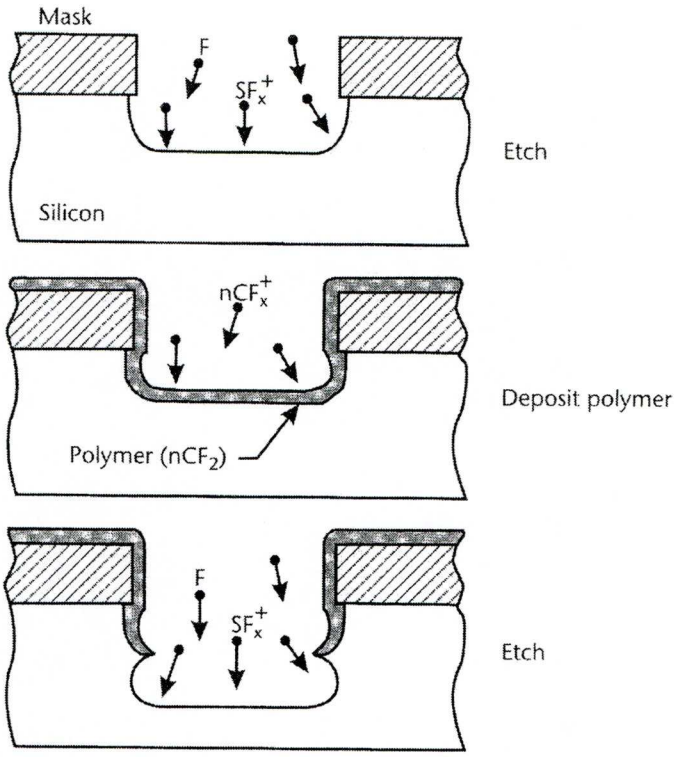

Figure 2.18 Profile of a DRIE trench using the Bosch process [Maluf, 2004].

First, sulphur hexafluoride (SF_6) is used to supply highly reactive fluorine radicals to etch silicon. Then a fluorocarbon polymer is plasma-deposited using C_4F_8 as the source gas. This passivation layer protects the entire substrate from further chemical attack and prevents further etching. In the following etch step, the vertically oriented ions (SF_x^+) bombard the passivation layer at the bottom of the trench, exposing it to the chemical etchant. The sidewalls remain relatively intact during the process. The repetitive alternation of these etch/deposit steps results in a nearly vertical structures with high etch rates from 1 to over 15μm/min, depending on the recipes and the power of the RF sources.

Compared to wet etching, DRIE is too expensive to be readily available to most researchers and many institutions. Another limitation is that the etch rate is dependent on the aspect ratio of the trench. As shown in Figure 2.19, the etch rate decreases with increasing trench aspect ratio. It drops significantly with narrow trenches.

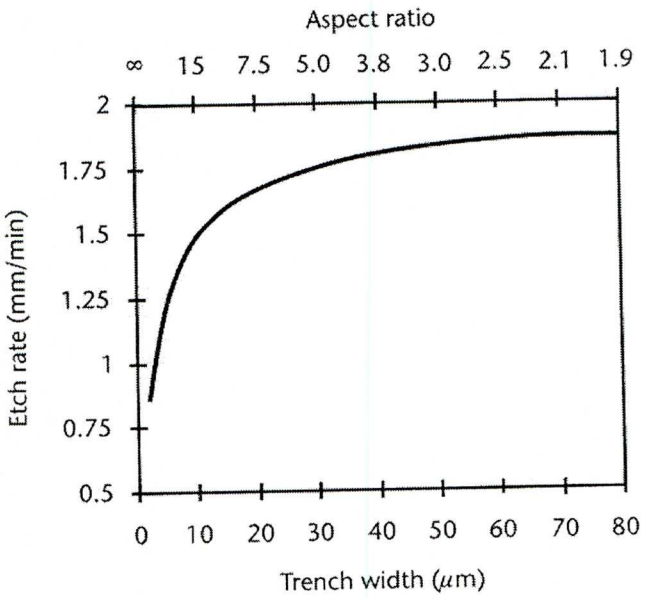

Figure 2.19 Etch-rate dependence on feature size and aspect ratio for a typical DRIE recipe at 600W [Maluf, 2004].

b. Thick-Resist Moulding

Restricted by the thickness of the wafer, moulds with large heights are normally acquired from etching thick-applied resist layers. Resist is a coating material used to mask or protect selected areas of a pattern from the action of an etchant. In general, resists are classified into two groups: positive resist and negative resist, depending on its response to the radiation. After the exposure to radiation,

if the exposed material is etched away in the developer solution and the unexposed region remains, the resist is considered to be positive. On the other hand, if the exposed part remains while the unexposed part is etched away, then it is negative. There are a number of different resists widely available in the commercial marketplace. Commonly used thick resists include SU-8, polyimide, polymethyl methacrylate (PMMA), and AZ-9260 etc.

SU-8 is an epoxy-based negative photo-resist. When exposed to near-ultraviolet (UV) light, SU-8 polymerises and becomes insoluble in liquid developers. Polymerised SU-8 is highly chemically and thermally stable. SU-8 has been of increasing use in various applications such as micro-moulding, micro-fluidics and other thick film MEMS devices. It can produce structures with aspect ratios of up to 20:1 and single layer thickness can range from 1 to 100μm depending on the spin speed and viscosity of the formulation used [Sameoto et al., 2006, Yang, 2004]. Lorenz described the use of SU-8 to build a copper-electroplated coil with tracks aspect ratio of 5:1 to reduce ohmic losses (Figure 2.20) [Lorenz, 1997]. The width and thickness of the coil lines are 8μm and 40μm, respectively.

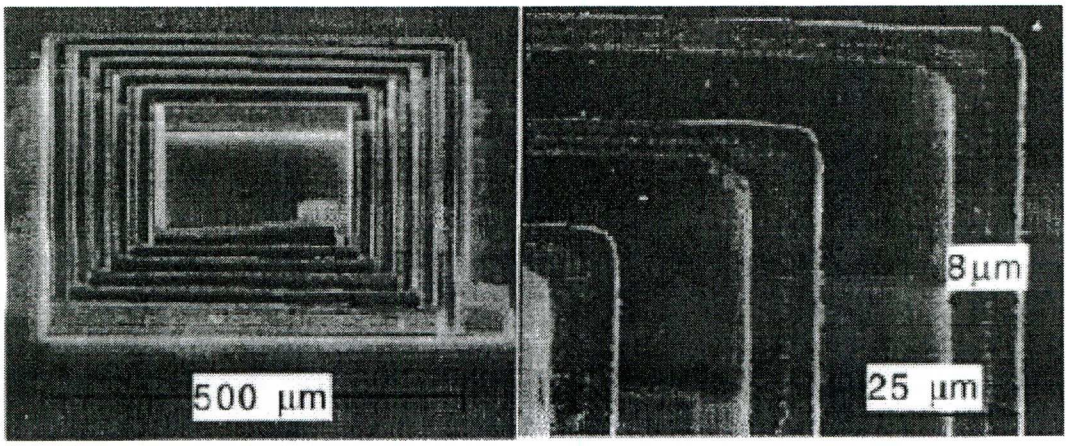

Figure 2.20 An electroplated copper coil produced with SU-8 photo-resist [Lorenz, 1997]

Compared to conventional thick resist material polymethyl methacrylate (PMMA) used in LIGA process, SU-8 processing does not need a synchrotron light source which is too expensive and not readily available for many laboratories and companies. While UV source is inexpensive and is widespread, therefore, sometimes SU-8 micro-moulding is called 'poor man's LIGA' [Lorenz, 1997].

However, SU-8 has also been found to have several significant disadvantages. One of them is the removal of SU-8 after post-baking and development. When used for electroplating mould, the highly cross-linked epoxy remaining after development is difficult to remove reliably from high aspect ratio structures without damage or alteration to the electroplated metal. In order to overcome this difficulty, some researchers reported the use of electrically conductive SU-8 to build micro-components [Jiguet, 2004]. Silver nano-particles were dispersed into SU-8 to enhance the electrical properties of the polymer. However, the electrical

conductivity of the SU8/silver composite is relatively low (around 10^3 to 10^6 $S.m^{-1}$) compared with the conductivity of copper (5.62×10^7 $S.m^{-1}$) or gold (4.13×10^7 $S.m^{-1}$).

Photosensitive polyimide is also frequently used as a thick resist. It is a negative type and can form microstructures with heights and aspect ratios up to 50μm and 10:1, respectively [Frazier, 1992]. But the development of polyimide often relies on expensive dry etching processes such as reactive ion etching (RIE), which is unfavourable for a low-cost manufacturing process. PMMA is a positive tone resist and is often used to form the mould in a LIGA process. It can achieve extremely high aspect ratio (up to 100:1) and large thicknesses (more than 300μm) [Wu, 2003]. The main drawback of this process is the cost. The exposure of PMMA needs an X-ray source which is expensive and is not readily available.

AZ9260 is a positive photoresist developed by Clariant Corp., America. This resist allows thicknesses of up to 100μm at a high resolution and very steep side walls. A comb structure formed by AZ9260 is illustrated in Figure 2.21 [Kohlmeier, 2004]. It has a thickness of 92μm and the minimum space between the comb legs is 10μm.

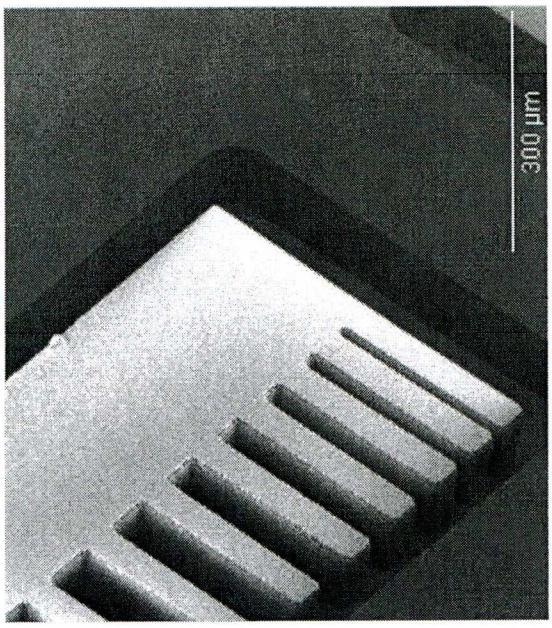

Figure 2.21 A comb structure formed by AZ9260 photoresist [Kohlmeier, 2004].

AZ9260 has been optimised for coil electroplating. The uses of this photoresist to form thick electroplating moulds for micro-coils have been reported in a number of researches [Beeby, 2004(2); Kohlmeier, 2004; Toh, 2005]. Rojanapornpun described the fabrication of a monolithic 2-layer micro-coil which employed AZ9260 as the photoresist mould [Rojanapornpun, 2006]. A high aspect ratio of 6:1 has been achieved in his research. In addition, he also used this photoresist as masks for wet etching and reactive ion etching (RIE) during the fabrication process. Unlike SU-8, AZ9260 can be easily removed after the development using trichloroethylene, acetone, methanol or AZ400K Developer, a potassium-based buffered alkaline solution provided by Clariant Corp.

Other thick resists include JSR THB series negative tone photo-resists from JSR Corp., Japan and DiaPlate 133 from CSEM, Switzerland have also been reported for constructing high thicknesses and aspect ratios of microstructures [Rao, 2006; Niedermann, 2003; Gonin, 2004]. Table 2.4 lists some commercially available thick resists along with their lithographic processes and polarities.

Table 2.4 Commercially available thick resists

Resist	**Lithography**	**Type**
SU-8	Near-UV light, E-beam or X-ray	Negative
Photosensitive polyimide	UV light	Negative
AZ-9260	UV light	Positive
DiaPlate 133	UV light	Negative
JSR THB series	UV light	Negative
Poly methyl methacrylate (PMMA)	E-beam or X-ray	Positive

2.4.2.4 Wafer Bonding

As its name implies, wafer bonding is a technique used to bond two or more wafers in order to form desired three-dimensional structures. There are many different wafer bonding processes currently available such as silicon fusion bonding, anodic bonding, eutectic bonding, adhesive bonding, vacuum bonding and bond aligning etc [Beeby, 2004(1)]. The first two techniques which will be used in the fabrication of the wireless pressure sensor will be discussed in the following sections.

a. Silicon Fusion Bonding

Silicon fusion bonding is a technique used to bond two silicon wafers. First, the two silicon wafers are pre-treated to make the two surfaces planar, clean and hydrophilic. The hydrophilisation step can be performed by boiling the two wafers in nitric acid (HNO_3) or ammonia water. The two wafers are then aligned and joined together at room temperature. Because the bond of the two wafers is caused by 'van der Waals force', it is weak and needs to be strengthened by a thermal annealing process. The annealing temperature is typically above 800°C and the bond strength is a function of this temperature. Fusion bonding technique can be also used to bond silicon and oxidised silicon wafers, silicon and silicon nitrides wafers or two surface oxidised silicon wafers. The maximum allowed thickness of the silicon dioxide film is about 4μm and the annealing temperature is typically 1100°C [Gardner, 2001]. Table 2.5 reveals the relationship of the operation temperature and the bond strength between different wafer bonding structures [Harendt, 1992].

Silicon fusion bonding takes the advantage of the perfectly matched thermal expansion coefficients of the two wafers. Therefore, little or no residual stress appears in the bonded wafer structures. It can achieve a seamless bond with exceptional strength and hermeticity. The main drawbacks of this technique are the required excellent flatness of the wafer surface and the high operation

Table 2.5 Bond strength at different operation temperatures [Harendt, 1992]

Structure	**Annealing temperature(°C)**	**Bond strength (Jm^{-2})**
Si/Si	450	0.5
Si/Si	800	0.6
Si/Si	1000	2.6
Si/Si_3N_4 (140nm)	800	0.9
Si/Si_3N_4 (140nm)	1000	Cleavage
Si/Si_3N_4 (300nm)	1000	Cleavage

temperature which make it difficult for bonding pre-processed wafers. To deal with this problem, low temperature silicon wafer bonding techniques have been developed in recent years. Tan suggested the bonding of two silicon wafers coated separately with PECVD SiO_2 and thermal SiO_2 at one surface of each wafer [Tan, 2005]. A chemical-mechanical polishing step was performed to increase the smoothness of the surfaces. By using these techniques, a strong bond was formed between these two wafers at the annealing temperature of 300°C. Some researches introduced the use of intermediate bonding layer, such as glass, gold, polydimethylsiloxane or polymethylmethacrylate in the bonding process [Brooks, 1972; Eaton, 1994; Ma, 1999]. Low annealing temperatures from room temperature to 200°C were reported. However, the introduction of the intermediate bonding material inevitably results in the increase of the residual stress in the structure, especially when the thermal expansion coefficient of this material is much different from silicon.

b. Anodic Bonding

Anodic bonding, also known as electrostatic bonding, is the most commonly used MEMS bonding technique for attaching silicon wafers to glass wafers. Electrostatic attraction force is employed to form the chemical bond. In this process, a glass wafer and a silicon wafer are aligned and clamped together using two metal electrodes. They are then placed onto a hotplate to be heated to a temperature of 350 to 500 ℃. A high DC potential (up to ~1kV) is applied between the electrodes, with the negative electrode connected to the glass wafer. This DC potential results into an electrical field which penetrates the wafers. Because the glass wafer contains a number of positive ions (mainly sodium), these ions become extremely mobile at the elevated temperature. The electrical field makes these positive ions drifting towards the glass wafer surface which is connected to the negative electrode, leaving a negative charge on the other side of the glass wafer. Due to electrostatic forces, the two wafers are pulled together and a solid chemical bond is formed. Figure 2.22 shows the process of anodic bonding [Beeby et al., 2004(1)].

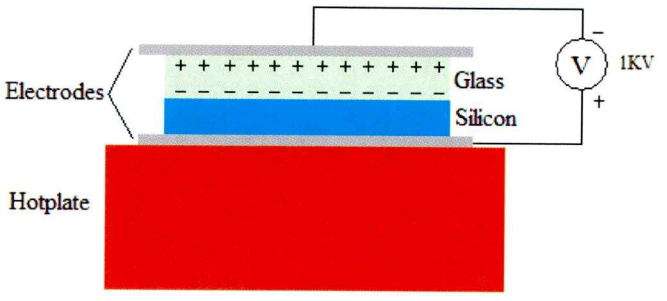

Figure 2.22 Schematic of anodic bonding [Beeby et al., 2004(1)].

Anodic bonding is attractive to MEMS community because of its low operation temperature requirement. It is frequently used to form hermetically sealed cavities for pressure sensors [Akar, 2001; Yoon, 2004; Saran, 2006]. Although this technique is mainly for bonding silicon and glass wafers, surface oxidised silicon wafers with SiO_2 thickness up to 100nm were bonded successfully to glass wafers using anodic bonding [Beeby, 2004(1)]. However, anodic bonding is incompatible for active devices because of the high electrostatic force [Park, 2006]. The difference of the thermal expansion coefficients of the two wafers also results into a stress in the structure. Nevertheless, this stress can be minimised if the thermal expansion coefficient of the selected glass wafer material is matched closely to that of silicon. A good example is Pyrex glass which will be discussed in Section 5.5.2.

2.4.2.5 Chemical Mechanical Polishing

Chemical mechanical polishing (CMP) is a surface planarisation process for wafers. During this process, the wafer is held by a wafer chuck and is pressed against the surface of a polisher pad. A slurry, which contains abrasive and corrosive chemicals, is applied underneath. The wafer and the polisher pad are then counter rotated to remove unwanted materials on the wafer both mechanically and chemically as shown in Figure 2.23 [Smith, 1999].

CMP is critical for some wafer bonding processes to achieve a seamless bond between the wafers. It is also necessary to set up the wafer for the subsequent micro-fabrication processes. For example, in a copper damascene electroplating process (discussed in Section 6.1.1); CMP is used to remove the surface copper layer for multilevel interconnections.

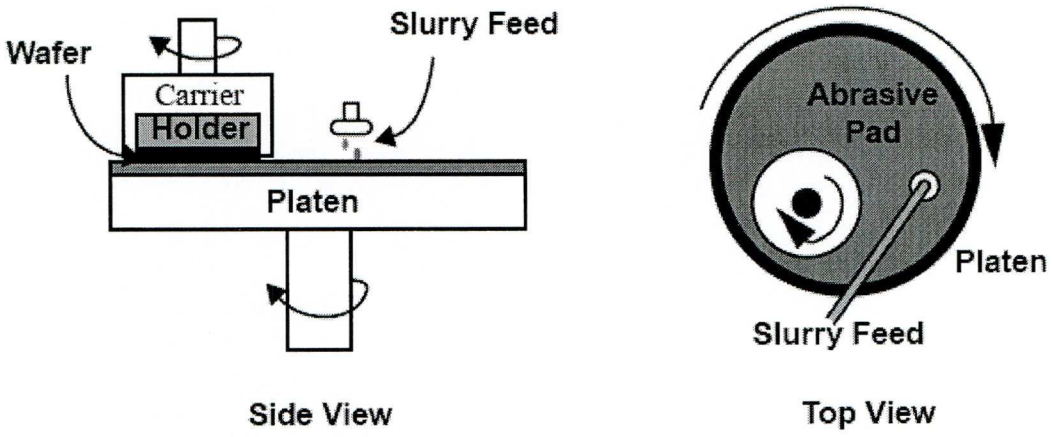

Figure 2.23 Chemical mechanical polishing tool configuration [Smith, 1999].

2.4.2.6 Evaporation and Sputtering

Evaporation and sputtering are two micro-fabrication techniques which are frequently used to deposit thin metallic films on substrate surfaces. They are sometimes referred as physical vapour deposition (PVD) in contrast to the CVD technique.

In the evaporation process, wafers and a block of source material are placed inside a high vacuum chamber (10^{-6} to 10^{-7} torr in pressure, 1 torr = 1mmHg).

Then a heating source such as an electron beam or a tungsten filament is used to heat the source material to a boiling point. The source material starts to evaporate and condense on all the exposed cool surfaces of the chamber and the wafer [Gardner, 2001].

The operation temperature in an evaporation process depends on the melting point of the material to be deposited. For metals with high melting points, e.g., tungsten, this deposition technique is impractical as the high operation temperatures may cause the damage of the evaporation device. Another problem of this technique is that the residual stresses in evaporated films are quite large. Therefore, evaporation is typically used to deposit metal films with thicknesses less than 0.5μm [Guisbiers, 2005]. The deposition rate in this process is about a few nanometres per second which is relatively low compared to other metal deposition techniques.

Similar to the evaporation deposition process, a sputtering deposition also takes place in a high vacuum chamber (10^{-6} to 10^{-8} torr in pressure) loaded with wafers and a block of source material. An inert gas (usually argon) is then introduced into the chamber at low pressure (about a few millitorr). A plasma of the inert gas is ignited using an RF power source, causing the gas to become ionised. The energetic ions of the plasma bombard the surface of the source material, resulting

into some of its atoms escaping from the surface. These escaped atoms then condense on all the exposed surfaces of the chamber including the wafers' surfaces to form the desired thin films.

Compared with evaporation technique, the operation temperature in a sputtering process is much lower due to the high-energy plasma introduced. As a result, materials with high melting points can be deposited without any difficulties using this technique. Sputtered films tend to have better uniformity than evaporated ones. Stresses in the deposited films can be tensile or compressive depending on the operation parameters such as the chamber pressure, inert gas pressure and the RF power [Chiu, 1999]. If these parameters are properly controlled, the stresses can be managed at a low level. Sputtering can produce films up to 3μm thick.

2.4.3 Introduction of Polymer MEMS

As introduced in previous section, silicon has been the dominating material for the fabrication of MEMS devices since the beginning of this new technology. However, during these years some other materials such as polymers, glasses, diamond, ceramics and quartz etc. are also frequently used for substrate or (and) structural materials in MEMS. Among these, polymer has become the most attractive material for MEMS sensors and actuators in recent years [Huang, 2005; Fonseca, 2006; Schneider, 2007].

Polymer materials include elastomers, plastics and fibres. They are widely used in agriculture, industry, medicine, sports and other applications. Commonly used polymers in MEMS are polydimethylsiloxane (PDMS), SU-8 epoxy, polyimide, liquid crystal polymer (LCP) and polyurethane etc. Liu concluded that polymers have several advantages over traditional MEMS material silicon [Liu, 2007]:

a. Polymers are more flexible than silicon. Although silicon has excellent mechanical properties such as large Young's modulus, it is too brittle to be used in applications where large displacements are required.

b. Most polymer materials are much cheaper than silicon and some fabrication processes can be accomplished without the need of clean-room. These make them extremely suitable for making disposable devices in medical applications.

c. Unlike silicon substrate, which is only available in wafer format, polymer substrate can be derived in arbitrary sizes and forms. Therefore, polymer MEMS devices can be realised in larges sizes.

d. There are more choices of the fabrication process for polymer MEMS than traditional silicon processing. These include thick film processing, casting and moulding, spraying and screen printing etc.

e. Polymers have some unique chemical or biological properties which can be used in some specific fields. An example is that PDMS is widely used in micro-fluidic devices because of its excellent biocompatibility, optical

transparency and simple processing features.

2.4.4 Laser Direct Writing

As its name implies, Laser direct writing is a fabrication technique for making microstructures on different substrates using laser beams. It is frequently used for making micro-channel networks, metallic structures or patterns for micro moulding on a variety of substrates such as silicon, polyimide, quartz or even fabrics [Kam, 2006; Huang, 2008; Ng, 2008]. Depending on the desired structures and applications, lasers used for micromachining can be chosen from nanosecond lasers to ultrafast lasers or from infrared (IR) lasers to ultraviolet (UV) lasers [Kam, 2006].

Laser direct writing is a simple and inexpensive micromachining technology. Pan described the use of a 248nm excimer laser to create micro-coil patterns for electroless copper plating [Pan, 2004]. First, a 2.5×2.5 cm^2 polyimide specimen was used as the substrate. Coil patterns were created through 248 nm KrF excimer laser projection ablation. Mask used for the pattern transmission was made of quartz coated with chromium (Cr). After the ablation, the polyimide substrate was immersed in sodium dodecyl sulfate (SDS) for pre-treatment and then cleaned with distilled water, nitric acid and acetone. The patterned substrate was subsequently immersed in electroless copper plating solution to generate the

micro-coils and finally cleaned with distilled water. Figure 2.24 shows the patterns of the micro-coils and the fabricated micro-coils [Pan, 2004].

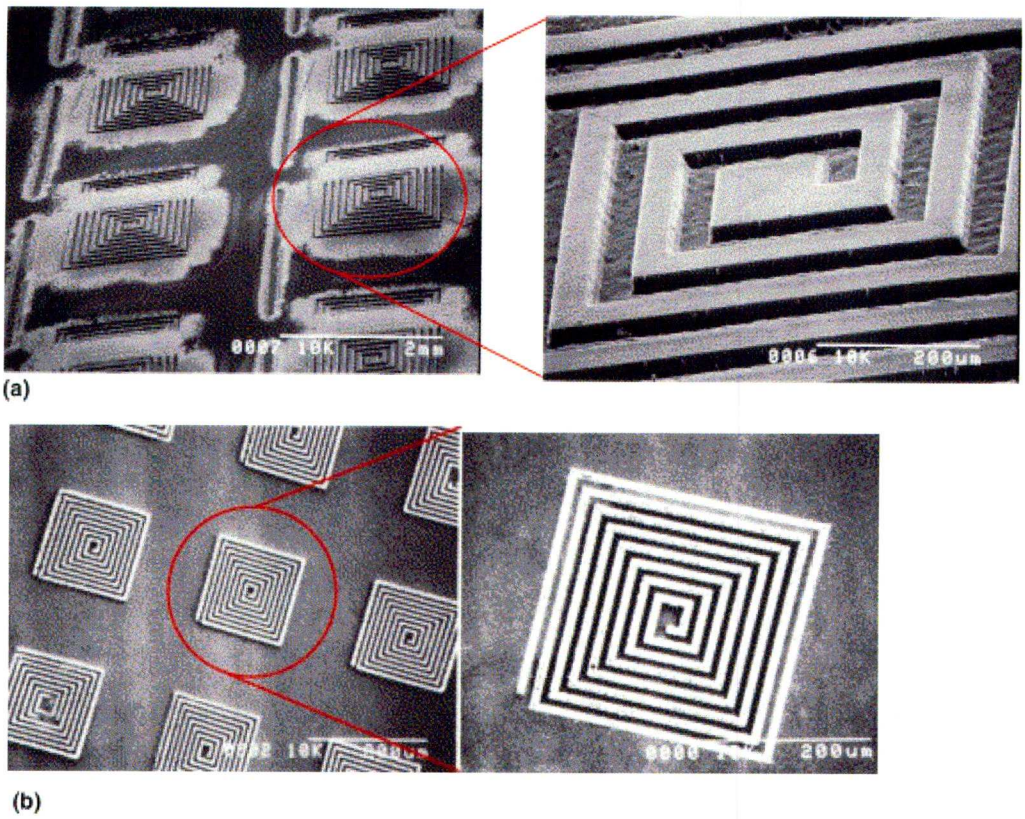

Figure 2.24 Micro-coil patterns and micro-coils fabricated by excimer laser and electroless plating (a) Micro-coil patterns with 2.5 × 2.5 cm^2 in area. (b) Micro-coils on polyimide substrate through electroless copper plating [Pan, 2004].

Comparing with conventional lithography process of forming planar coil patterns on substrate, this method simplifies the manufacturing process. However, the ablation depth of the substrate is restricted to several microns. Although greater ablation depth can be achieved with higher laser energy, it may destroy the Cr film on the quartz mask and degrade the adjacent polyimide substrate. Therefore, this method is not suitable for fabricating planar coils with thick tracks.

References

Akar O., Akin T., Najafi K., A wireless batch sealed absolute capacitive pressure sensor, *Sensors and Actuators A95*, (2001) 29–38.

Aref S. H., Latifi H., et al., Fiber optic Fabry-Perot pressure sensor with low sensitivity to temperature changes for down-hole application, *Optics Communications*, Vol. 269, Issue 2, Jan. 2007, pp. 322-330;

Beeby S. P., et al., *MEMS Mechanical Sensors*, Artech House, Inc., Norwood, America, 2004(1).

Beeby S. P., et al., Micro-machined silicon Generator for Harvesting Power from Vibrations, *Proceedings of the 4th International Workshop on Micro and Nanotechnology for Power Generation and Energy Conversion Applications,* 2004 (2), Kyoto, Japan, pp. 104-107.

Brooks A. D., Donovan R. P., and Hardesty C. A., Low-temperature electrostatic silicon-to-silicon seals using sputtered borosilicate glass, *Journal of Electrochemical Society*, 119, 1972, pp. 545-546.

Buff W., Klett S., et al., Passive Remote Sensing for Temperature and Pressure Using SAW Resonator Devices, *IEEE Transactions on Ultrasonics, Ferroelectrics, and Frequency Control*, Vol. 45, No. 5, Sep. 1998, pp. 1388-1392;

Bulst W. E., Fischerauer G., State of art in wireless sensing with surface acoustic waves, *IEEE Transaction on Industrial Electronics*, Vol. 48, No. 2, Apr. 2001.

Chiu, K. P., Barber, Z. H., and Smoekh, R. E., The control of film stress using ionised magnetron sputter deposition, *Thin Solid Films 343-344*, 1999, pp. 39-42.

Chollet F., Liu HB., *A (not so) short Introduction to Micro Electromechanical Systems*, F. Chollet, HB. Liu, version 2.0.1, accessed in Mar. 2007, Website: http://memscyclopedia.org/introMEMS.html

Collins C., Miniature passive pressure transensor for implanting in the eye, *IEEE Trans. Biomed. Eng.* BME-14(2), 1967, pp. 74-83.

DeHennis A. D., Wise K. D., A wireless micro-system for the remote sensing of pressure, temperature, and relative humidity, *Journal of Microelectromechanical System*, Vol. 14, No. 1, Feb. 2005, pp.12-22.

Eaton W. P., Risbud S. H., and Smith R. L., *Silicon Wafer-to-Wafer Bonding at T<200 °C with Polymethylmethacrylate, Applied Physics Letters*, 65, (1994), pp. 439-441.

Eklund A., A resonator sensor for measurement of intraocular pressure-evaluation in an in vitro pig-eye model, *Physiological Measurement,* 21 (2000), pp. 355-367.

Fonseca M. A., Flexible wireless passive pressure sensors for biomedical applications, *Solid-State Sensors, Actuators, and Microsystems Workshop*, Hilton Head Island, South Carolina, June 4-8, 2006, pp. 37- 42.

Frazier A. B., Allen M. G., Metallic microstructures fabricated using photosensitive polyimide electroplating molds, *Journal of Microelectromechanical Systems*, Vol. 2, No. 2, 1993, pp. 87-94.

Gardner J. W., Varadan V. K., Awadelkarim O. O., *Micro-sensors: MEMS and Smart Devices*, Publisher: Wiley, First Edition, 2001.

Gonin Y., et al., Comparison of a new photo-resist (DiaPlate 133) with SU-8 using both x-ray and ion beam lithographies, *Journal of Vacuum Science & Technology BL Microelectronics and Nanometer Structures*, July 2004, Vol. 22, Issue 4, pp. 1982-1986.

Grimes C. A., Magnetoelastic sensors for remote query environmental monitoring, *Smart Material Structure*, 8(1999), pp. 639-646.

Grimes C. A., Mungle C. S., et al., Wireless Magnetoelastic Resonance Sensors : A Critical Review, *Sensors 2002*, 2, pp. 294-313;

Guisbiers, G., Strehle, S., Wautelet, M., Modelling of residual stresses in thin films deposited by electron beam evaporation, *Microelectronic Engineering 82* (2005), pp. 665-669.

Harendt, C., Graf, H. G., HÖfflinger, B., and Penteker, E., Silicon fusion bonding and its characterisation, *Journal of Micromechanics and Microengineering 2* (1992), pp. 113-116.

Hsu T. R., *MEMS & Microsystems Design and Manufacture*, McGraw-Hill, Inc., 2002.

Ijntema D. J., Feasibility study for a micro machined eye pressure regulator for glaucoma patients, Report from the University of Twente, EL-TDM, Enschede, The Netherlands, 1992.

Jain M. K., S. Schmidt S., et al., Magnetoacoustic Remote Query Temperature and Humidity Sensors, *Smart Materials and Structures,* 9(2000), pp. 502-510.

Jain M. K., and Grimes C. A., A Wireless Magnetoelastic Micro-Sensor Array for Simultaneous Measurement of Temperature and Pressure, *IEEE Transactions on Magnetics,* Vol. 37, No. 4, Jul. 2001, pp. 2022-2024.

Yole Development, *Report: Ultimate MEMS Market Analysis*, Published in May 2005.

Jiguet, S. et al., SU8-Silver Photosensitive Nano-composite, *Advanced Engineering Materials 2004*, 6, No. 9, pp. 719-724.

Karl, W. J., Powell, A. L., A micro-machined magnetostrictive pressure sensor using magneto-optical interrogation, *Sensors and Actuators* 81(2000), pp. 137-141.

Kohlmeier, T., Seidemann, V., Buttgenbach, S., Gatzen, H. H., An investigation on technologies to fabricate micro-coils for miniaturised actuator systems, *Microsystem Technology* 10 (2004), pp. 175-181.

Korvink J. G., Rudnyi E. B., et al., *MEMS and NEMS simulation, MEMS: A Practical Guide to Design, Analysis, and Applications*, William Andrew Publishing (2005).

Kouzoudis Dimitris, Crimes Craig A., The frequency response of magnetoelastic sensors to stress and atmospheric pressure, *Smart Material Structure*, 9 (2000), pp. 1-5.

Lam K. B., Chiao, M., and Lin, L. W., A micro photosynthetic electrochemical cell, *MEMS 2003*, Kyoto, Japan, pp. 391-394.

Lam K. B., Johnson, E. A., Chiao, M., and Lin, L. W., A MEMS Photosynthetic Electrochemical Cell Powered by Subcellular Plant Photosystems, *Journal of Microelectromechanical systems*, Vol. 15, October 2006, pp. 1243-1256.

Lewis M., SAW and Optical Signal Processing, *IEEE Ultrasonic Symposium*, 2005, pp. 800-809.

Lorenz H., Despont H., et al., SU-8: A Low-cost Negative Resist for MEMS, *Journal of Micromechanics and Microengineering*, vol. 7, 1997, pp. 121-124.

Ma G. Y., Yan G. Z., He X., Power transmission for gastrointestinal Microsystems using inductive coupling, *Physiological Measurement*, 28(2007) pp. 9-18.

Maluf, N. and Williams K., *An Introduction to Microelectromechanical Systems Engineering*, second edition, Artech House, Inc., 2004.

Meninger S. et al., Vibration-to-electric energy conversion, *IEEE Trans. VLSI Syst.*, vol. 9, 2001, pp. 64 –76.

Niedermann P., et al., A novel thick photo-resist for microsystem technology, *Microelectronic /Engineering* 67-68 (2003), pp. 259-265.

Park G. S., Yu J. H., et al., Wafer level hermetic packaging for RF-MEMS devices using electroplated gold layers, *Key Engineering Material*, Vols. 326-328, 2006, pp. 617-620.

Pohl A. and Seifert F., Wirelessly Interrogable Surface Acoustic Wave Sensors for Vehicular Applications, *IEEE Transactions on Instrumentation and*

Measurement, vol. 46, no. 4, Aug. 1997, pp. 1031-1038.

Pohl A., Ostermayer G. and Seifert F., Wireless Sensing Using Oscillator Circuits Locked to Remote High-Q SAW Resonators, *IEEE Transactions on Ultrasonics, Ferroelectrics, and Frequency Control*, vol. 45, no. 5, Sep. 1998, pp. 1161-1168.

Puers R., Vandevoorde G., and De Bruyker D., Electrodeposited copper inductors for intraocular pressure telemetry, *J Micromech & Microeng*, 10(2), 2000, pp. 124-129.

Rao V. S., Kripesh V., A thick photoresist process for advanced wafer level packaging applications using JSR THB-151N negative tone UV photoresist, *Journal of Micromechanics and Microengineering*, vol. 16, 2006, pp. 1841-1846.

Reindl L., Wireless Passive SAW Identification Marks and Sensors, *2nd Int. Symp. Acoustic Wave Devices for Future Mobile Communication Systems*, Chiba Univ. 3rd-5th March, 2004, pp. 1-15.

Remon Medical Technologies Inc., website: http://www.remonmedical.com, accessed in Jul. 2007.

Rojanapornpun O., *Microfabrication Technology for an Integrated Monolithic Electromagnetic Microactuator based on Polymer Bonded Permanent Magnet*, Phd thesis, School of Electrical Engineering and Telecommunications, University of New South Wales, Sydney, Australia, Aug. 2006.

Rosengren L., Söderkvist J., Smith L., Micromachined sensor structures with linear capacitive response, *Sensors and Actuators*, A31, 1992, pp.200-205.

Rosengren L., A system for passive implantable pressure sensors, *Sensors and Actuators A*, 43 (1994), pp.55-58.

Sakakibara T. et al., Multi-source power supply system using micro-photovoltaic devices combined with microwave antenna, *MEMS 2001*, Interlaken, Switzerland Jan. 2001, pp. 192 – 195.

Sameoto D., Tsang S. H., et al., Control of the out-of-plane curvature in SU-8 compliant microstructures by exposure dose and baking times, *Journal of Micromechanics and Microengineering*, vol. 17, no. 5, May 2007, pp. 1093-1098.

Saran A., Abeysinghe D. C., Microelectromechanical system pressure sensor integrated onto optical fiber by anodic bonding, *Applied Optics*, Vol. 45, No. 8, Mar. 2006, pp. 1737-1742.

Scherr et al., Quartz Pressure Sensor Based on SAW Reflective Delay Line, *IEEE Ultrasonics Symposium*, 1996, pp. 347-350.

Schmidt F., Sczesny O., et al., Remote sensing of physical parameters by means of passive surface acoustic wave devices (`ID TAG'), *Proc. IEEE Ultrasonics Symp.*, 1994, pp. 589-592.

Scholl G., Schmidt F., and Wolff U., Surface Acoustic Wave Devices for Sensor Applications, *Phys. Stat. Sol.*, (a) 185, No. 1, 2001, pp. 47-58.

Smith T. H., *Device Independent Process Control of Dielectric Chemical Mechanical Polishing*, Phd thesis, Massachusetts Institute of Technology, Sep. 1999.

Søndergård O., Gravesen P., A new piezoresistive pressure transducer principle with improvements in media compatibility, *J. Micromech. 6 (1996)*, pp.105-107.

Stangel K., Kolnsberg S., et al., A Programmable Intraocular CMOS Pressure Sensor System Implant, *IEEE J Solid-State Circuits*, 36(7), 2001, pp.1094-1100.

Sterken T., Baert K., Puers R., Borghs S., Power extraction from ambient vibration, *Proc. SeSens 2002*, Veldhoven, Netherland, Nov. 2002, pp. 680 – 683.

Suzuki S. N., et al., A Proposal of Electric Power Generating System for Implanted Medical Devices, *IEEE Trans. on Magnetics*, Vol. 35, No. 5, Sep. 1999, pp. 3586-3588.

Tan C. S., Chen K. N., et al., Low temperature direct chemical-vapour-deposition (CVD) oxides to thermal oxide wafer bonding in silicon layer transfer, *Electrochemical and Solid-State Letters*, 8(1), 2005, pp. 1-4.

Toh, B. H. W., McNeill, D. W., Gamble, H. S., Characterisation of copper inductors fabricated by dual damascene and electroplating techniques, *Journal of Materials Science: Materials in Electronics* 16 (2005), pp. 233-238.

Uno H., Kumatani I., et al., Synthesis and simulation of digital demodulator for infrared data communication, *Proc. Asia and South pacific Design Automation Conference,* August 1995, pp. 423-427.

Van Schuylenbergh K. and Puers R., Self-tuning inductive powering for implantable telemetric monitoring systems, *Sensors and Actuators A52*, 1996, pp. 1-7.

Williams C.B., Yates R. B., Analysis of a Micro-electric Generator for Microsystems, *Sensors and Actuators A*, Vol. 52, 1996, pp. 8-11.

Wolff U., Dickert F. L., et al., SAW sensors for harsh environments, *IEEE Sensors J.*, vol. 1, Jun. 2001, pp. 4-13.

Wu J., *Inductive links with integrated receiving coils for MEMS and implantable applications*, PhD thesis, the Department of Electrical Engineering, University of Notre Dame, Indiana, America, 2003.

Yang, R., Wang, W., Out-of-plane Polymer Refractive Microlens Fabricated Based on Direct Lithography of SU-8, *Sensor and Actuators A: Physical* 113 (2004), pp 71-77.

Yoon H. J., Jung J. M., Micro devices for a cerebrospinal fluid (CSF) shunt system, *Sensor and Actuators A: Physical*, vol. 110, Issues 1-3, Feb. 2004, pp. 68-76.

Chapter 3
Magnetoelastic Thick-Film Pressure Sensor

Magnetoelastic sensors are very sensitive to a number of environment parameters such as pressure, temperature, humidity, mechanical vibration and liquid viscosity etc. They have attracted considerable interests within the sensor community in recent years. In this chapter, the design of a magnetoelastic thick-film pressure sensor is presented. It consists of a sensor array with a flat sensor and a folded sensor which are made of ferromagnetic alloys. The characteristic resonant frequencies of the two sensors as well as their frequency shifts in response to pressure changes are calculated.

3.1 Introduction

Magnetoelastic sensors allow the monitoring of environmental parameters without the use of direct physical connections. Therefore they have the potential for medical applications where wires are either inadvisable or prohibited. When placed in a magnetic field, a magnetoelastic material changes its dimension thereby translating magnetic energy into elastic energy. Conversely, it alters the magnetisation in the material when subjected to a mechanical load. The use of magnetoelastic materials for sensing pressure, temperature, stress, flow velocity,

humidity, liquid viscosity and mass loading was suggested in a number of researchers [Karl, 2000; Kouzoudis, 2000; Jain, 2001].

The most commonly used magnetoelastic materials for sensing applications are iron-rich ferromagnetic alloys such as $Fe_{40}Ni_{38}Mo_4B_{18}$ (Metglas^{TM} brand 2826MB) or $Fe_{81}B_{13.5}Si_{3.5}C_2$ (Metglas^{TM} brand 2605SC) [Grimes, 2002]. They are usually prepared in amorphous states which can be made through a rapid quenching process to prevent atoms to arrange themselves. Initially, all amorphous alloys have stresses because of this fabrication process. However, these stresses can be reduced or eradicated through heat treatment. For example, by heat treating ferromagnetic amorphous alloys at 400°C for 1 hour, all the stresses can be eliminated.

When used for sensors, ferromagnetic materials can be either in thin-film or thick-film form. Thin ferromagnetic film can be produced by sputtering [Wallace, 1993], a micromachining process in MEMS which a flux of inert-gas ions (usually argon) is employed to physically bombard target materials in a vacuum chamber in order to deposit these materials onto a wafer [Maluf, 2004]. Karl reported a magnetostrictive membrane-type pressure sensor which was based on a pressure sensitive membrane coated with the thin-film ferromagnetic material, $Fe_{81}B_{13.5}Si_{3.5}C_2$ [Karl, 2000]. The change of magnetic properties of this thin film caused by pressure difference across the membrane was detected using

Magneto-Optical Kerr Effect. Thick-film ferromagnetic materials can be obtained by spraying molten Fe-based alloys onto a fast spinning wheel, where it quickly solidifies [Hase, 1992].

Thin-film magnetoelastic materials have the advantage of being able to be integrated into a MEMS process and therefore batch fabrication becomes possible. However, this research only focused on the use of thick-film material for pressure sensing because of available resources.

3.2 Thick-film Pressure Sensor

3.2.1 Pressure sensing Principle

A ribbon-shaped magnetoelastic thick-film sensor mechanically vibrates when it is subjected to a time varying magnetic field. The resonant frequency of this vibration is inversely proportional to the sensor length. The relationship between the resonant frequency and the mechanical properties of a magnetoelastic sensor is shown in Equation 3.1[Grimes, 2002]:

$$f_n = \frac{n}{2L}\sqrt{\frac{E}{\rho(1-\nu^2)}} \qquad (n = 1,2,3,...) \qquad (3.1)$$

where L is the length of the ribbon, E, ρ and ν are the Young's modulus, density and Poisson's ratio of the sensor material, respectively. In most applications only the fundamental resonant frequency f_1 (when n=1) is considered because it has higher signal amplitude and lower frequency than other resonant frequencies (n=2, 3,…).

However, a flat ribbon-shaped magnetoelastic sensor is insensitive to pressure changes. In order to make it sensitive, this flat ribbon needs to be elastically or plastically deformed [Kouzoudis, 2000]. Figure 3.1 shows four different methods to create stressed sensors from magnetoelastic ribbons.

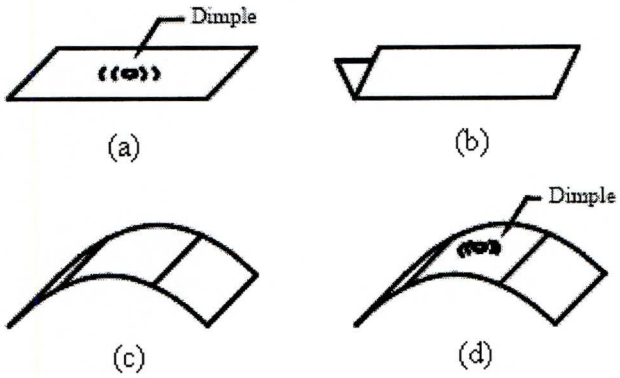

Figure 3.1 Stressed sensor shapes: (a) a flat sensor with a dimple, (b) a folded sensor, (c) a curved sensor, (d) a curved sensor with a dimple [Kouzoudis, 2000].

Kouzoudis explained the reason of the insensitivity of a flat sensor in response to pressure changes [Kouzoudis, 2000]. As shown in Figure 3.2a, a flat sensor only exhibits a longitudinal (x-directional) vibration when it is placed in an interrogation magnetic field. During vibration, the change of normal force applied by the surrounding atmosphere can be only found at the two ends of the sensor (y-z planes). This force causes a damping effect which may result in a decrease of sensor resonant frequency. However, the surface areas of the two ends are quite small compared with its surfaces which are normal to the z direction (x-y planes), as the sensor is usually of 20 to 30μm in thickness.

Therefore, this damping effect can be neglected. As a result, a flat sensor is insensitive to pressure changes.

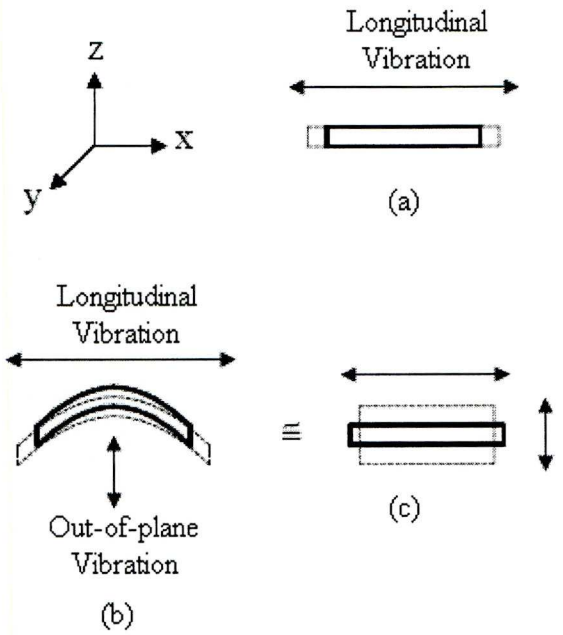

Figure 3.2 Vibrations of magnetoelastic sensors in magnetic fields: (a) a flat sensor with longitudinal vibrations; (b) a curved sensor with longitudinal and out-of-plane vibrations; (c) approximation of a curved sensor by a flat sensor with large Poisson's ratio [Kouzoudis, 2000].

When the sensor is curved as shown in Figure 3.2b, besides the longitudinal vibration, an out-of-plane vibration also occurs in the z direction. This out-of-plane vibration has a much bigger surface area than that of the two ends. Therefore, the damping effects of the normal forces acted on the sensor surface are much greater compared with a flat sensor. Increasing the ambient pressure causes the increase of this damping force and decreases the sensor resonant frequency.

The vibration of a curved sensor with small curvature in a magnetic field can be approximated as a flat sensor with a relatively large Poisson's ratio (Figure 3.2c). As the flat sensor vibrates longitudinally, an out-of-plane vibration also takes place because of the large Poisson's ratio of the sensor. Based on this theoretical model, Grimes calculated the resonant frequency shift of a magnetoelastic pressure sensor when it is placed in a chamber filled with gas [Grimes, 2002]. The resonant frequency shift Δf is expressed as follows:

$$\Delta f = -\left[\frac{1}{\sqrt{3}} \frac{\nu^2 \cdot m_g \cdot \bar{u}}{(1-\nu) \cdot k_B \cdot T \cdot d \cdot \rho}\right] p \tag{3.2}$$

where ν is the Poisson's ratio of the sensor material, m_g is the mass of the gas particle, $\bar{u}$ is the mean velocity of the gas, k_B is Boltzmann's constant (1.38×10^{-23} J/K), T is the temperature and p is the pressure of the chamber, and ρ and d are the density and thickness of the sensor material, respectively. It can be seen from the equation that the resonant frequency shift is linear with the gas pressure and it decreases with the increase of the gas pressure.

As the damping effects are determined by the effective surface area on which the normal forces are applied, the increase of this area can result in an increase of the sensor pressure sensitivity. The pressure sensitivities of four curved sensors which have different curvatures are compared in Figure 3.3. It shows that the sensor with the largest curvature has the highest pressure sensitivity [Kouzoudis, 2000].

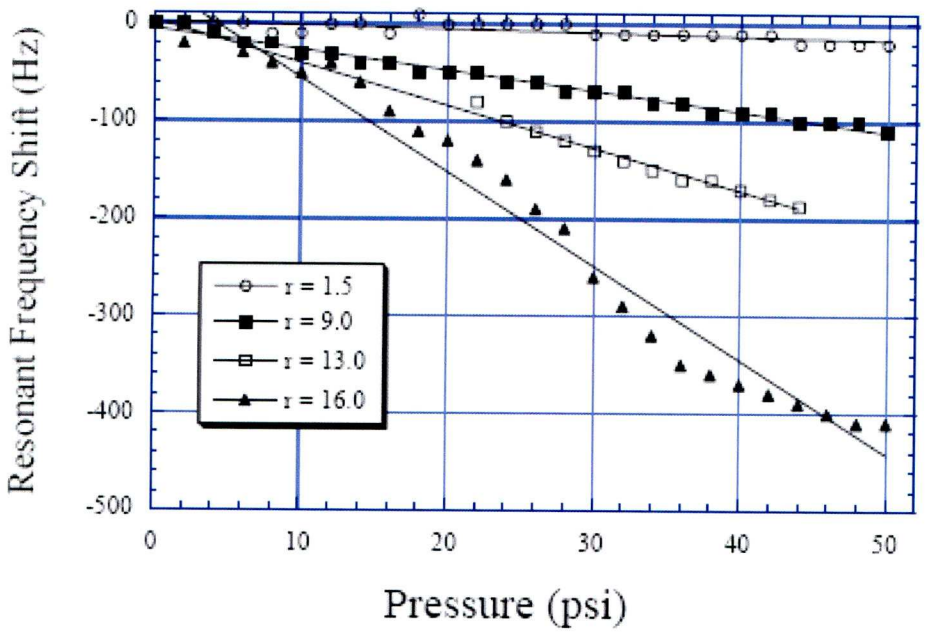

Figure 3.3 The comparison of sensor pressure sensitivity with different curvatures [Kouzoudis, 2000].

3.2.2 Removal of Temperature Effect

As mentioned at the beginning of this chapter, magnetoelastic materials are sensitive to a number of environmental parameters. Therefore, when used for pressure sensing the effects of other parameters need to be removed. In most cases the elimination of temperature effect on a temperature dependent sensor is quite complicated. However, two simple methods were suggested in literature to cancel the temperature dependence of a magnetoelastic pressure sensor.

3.2.2.1 Biasing Magnetic Field

The effect of temperature and applied magnetic field on the sensor resonant frequency is expressed as [Grimes, 2002]:

$$f(T,H)=\frac{1}{2L(T)}\sqrt{\frac{E(T)}{\rho(T)}}\left(1+\frac{9\lambda^2(T)\cdot H^2\cdot E(T)}{M(T)\cdot H_{k\sigma}{}^3(T)}\right)^{-1/2} \tag{3.3}$$

where H is the applied magnetic field, L is the sensor length, $E(T)$ is the modulus of elasticity of the sensing material at temperature T, $\rho(T)$ is the density of the sensor material, λ is the magnetostriction, $M(T)$ is the saturation magnetisation, and $H_{k\sigma}(T)$ is the anisotropy field when the sensor is under a longitudinal stress. Equation 3.3 indicates that the removal of the temperature effect on the sensor can be achieved by applying a DC biasing field of appropriate magnitude. Grimes tested the temperature dependency of a sensor made of Metglas 2826MB with dimensions of 3cm×1.3cm×28μm as a function of varying magnetic field amplitudes and the results are shown in Figure 3.4 [Grimes, 2002]. It shows that the removal of temperature dependency of the sensor can be achieved by applying a biasing magnetic field with strength of 7.01Oersteds.

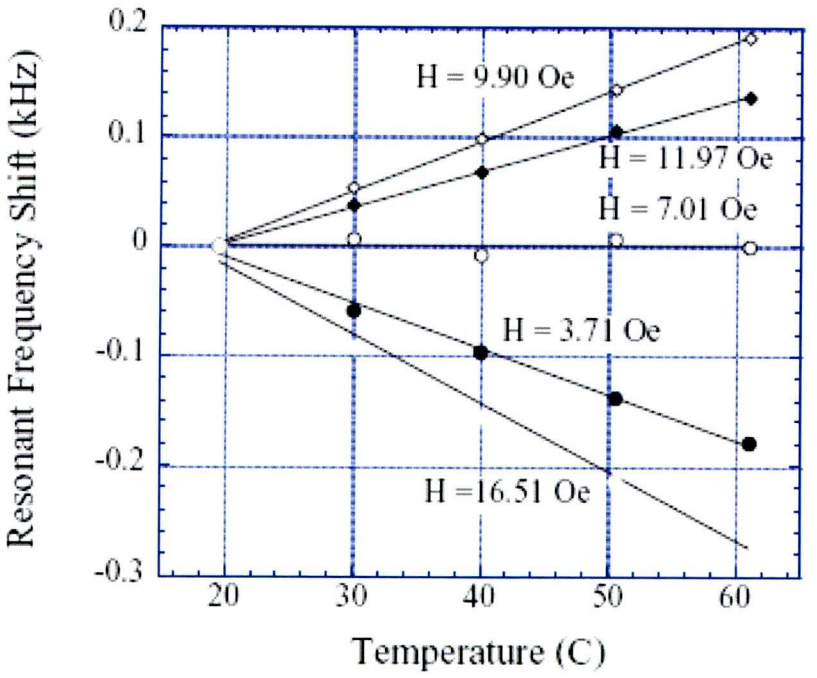

Figure 3.4 The resonant frequency shifts of a magnetoelastic sensor verses temperature and bias field [Grimes, 2002].

3.2.2.2 Sensor Array

Another way of determining the temperature independent pressure is to build a sensor array using a flat sensor and a curved sensor constructed from the same magnetoelastic material. Because the flat sensor is insensitive to the changes of ambient pressure, while temperature affects the flat sensor and the curved sensor equally in the same way, the pressure information can be found from the frequency changes of the two sensors even if there is a temperature change of the environment. Figure 3.5 shows the normalised resonant frequency (f/f_0) shifts of a sensor array consisted of a flat sensor and a dimpled sensor with the change of ambient pressure at temperatures of 23C° and 40C°. It can be observed from the figure that the normalised resonant frequency shifts of each sensor are parallel to each other at different temperatures.

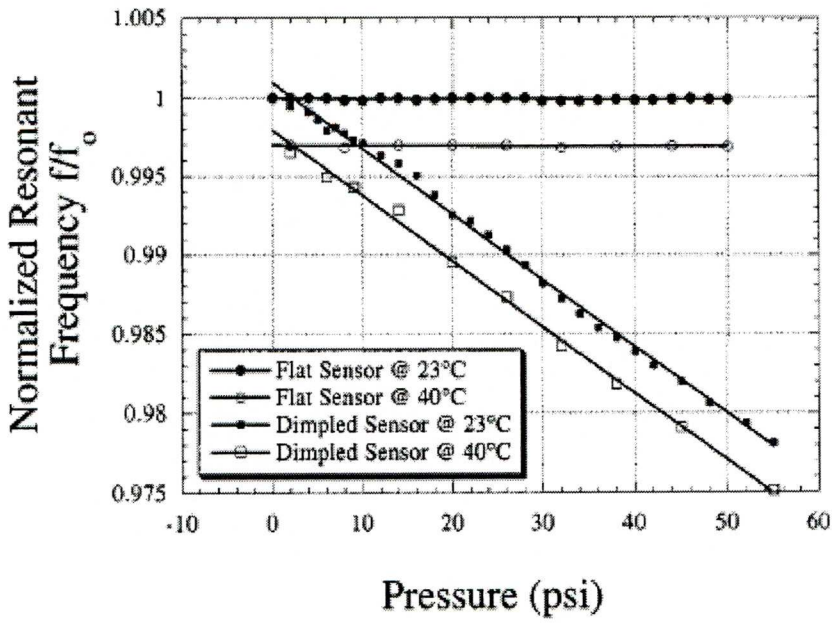

Figure 3.5 Pressure measurement in a changing temperature environment using two 2826MB alloy sensors of different stress levels [Jain, 2001].

3.2.3 Pressure Sensor Structure

Based on the above principle, a pressure sensor array was constructed. It is made of ribbon-like Metglas^{TM} alloys 2826MB with thickness of 30μm. Some physical properties of this material are listed in Table 3.1.

Table 3.1 Physical properties of Metglas 2826MB

Thickness (μm)	30
Poisson's ratio	0.3
Density (g/cc)	7.90
Tensile Strength (MPa)	1,000-1,700
Elastic Modulus (GPa)	100-110
Thermal Expansion (ppm/ $^{\circ}$C)	11.7

The sensor array consists of a flat sensor and a folded sensor. The length of the flat sensor is 2.5mm and the original length of the folded sensor (before folding) is 2mm. The reason of making the lengths of two sensors slightly different is to distinguish the characteristic resonant frequencies of the two sensors so that the frequency ranges do not overlap during operation. The widths of the two sensors are both 0.5mm. After cutting from the Metglas ribbon, the sensors were then mounted onto a plastic base at their non-vibrating midlines using epoxy based adhesive M-bond 610. Figure 3.6 shows the layout of the sensor array and the dimensions of the flat and folded sensors.

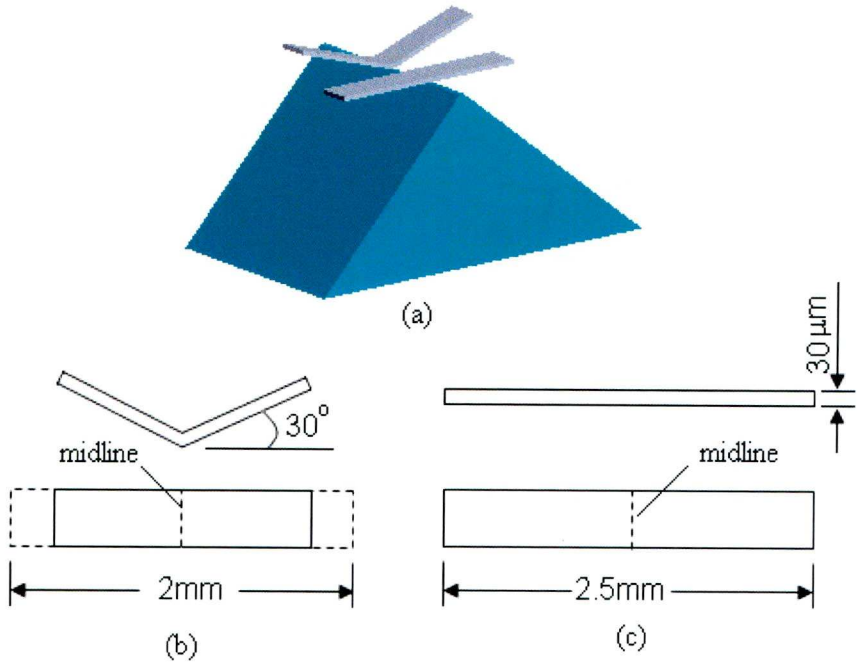

Figure 3.6 Layout of the sensor array and the dimensions of the sensors
(a) Sensor array; (b) the folded sensor; (c) the flat sensor.

3.2.4 Calculated Frequency Response

The characteristic resonant frequencies of the flat sensor and the folded sensor were calculated from Equation 3.1 to be 746kHz and 933kHz respectively. It is assumed that the sensor array is placed in a pressure chamber filled with nitrogen (N_2) and is under room temperature (23°C). The resonant frequency of the flat sensor does not change in response to the pressure changes, while the shift in resonant frequency of the folded sensor can be calculated from Equation 3.2. Using the values from Table 3.2, the result of this shift is derived as -1.36Hz/kPa.

Table 3.2 Values used in Equation 3.2

ν	Poisson's ratio	0.3
m_g	N_2 molecule mass (g)	4.65×10^{-23}
$\bar{u}$	N_2 gas mean velocity (m/s)	380
k_B	Boltzmann's constant (J/K)	1.38×10^{-23}
T	Temperature (K)	296
d	Thickness (μm)	30
ρ	Sensor material density (kg/m^3)	7.9×10^3

3.2.5 Detection of Resonant Frequency

As described in Chapter 2, the resonant frequency of the magnetoelastic pressure sensor can be detected by magnetic, acoustic or optical means. Because the sensor is to be implanted into the human body, the best way is to detect the frequency magnetically as an acoustic wave is hard to transport from liquid to air and an optical source cannot reach the sensor when it is embedded.

The experiment was designed to use a Network Analyser to sweep interrogating signals which have frequencies from 500 kHz to 2 MHz. The sensor will mechanically vibrate and emit a magnetic flux. Using the same Network Analyser and pick up coil(s) to record the measured amplitude of each incremental frequency and the pressure information can be determined. However, as the pressure sensitivity of the sensor was so small, environment noise actually

dominated the result. In order to measure the sensor frequency shift accurately and remove the effect of environment noise, highly precise Network Analyser and metal-shielding room are required. Limited by the available resources in the laboratory this experiment was terminated. In addition, some other problems associated with this technology include possible tissue heating caused by the required DC biasing field and high product costs because of the difficulties for incorporating the fabrication process in MEMS systems. The next step of the research was focused on developing an inductor-capacitor resonant type pressure sensor which will be presented in Chapter 5.

References

Grimes C. A., Mungle C. S., et al., Wireless Magnetoelastic Resonance Sensors: A Critical Review, *Sensors 2002*, 2, pp. 294-313.

Hase H., Shoji R., et al., Oil Pressure Sensor Using Amorphous Magnetic Alloy, *SAE Technical Paper*, No. 920700, 1992.

Jain M. K., and Grimes C. A., A Wireless Magnetoelastic Micro-Sensor Array for Simultaneous Measurement of Temperature and Pressure, *IEEE Transactions on Magnetics,* Vol. 37, No. 4, Jul. 2001, pp. 2022-2024.

Karl, W. J., Powell, A. L., A micro-machined magnetostrictive pressure sensor using magneto-optical interrogation, *Sensors and Actuators* 81(2000) pp. 137-141.

Kouzoudis Dimitris, Crimes Craig A., The frequency response of magnetoelastic sensors to stress and atmospheric pressure, *Smart Material Structure*, 9 (2000), pp. 1-5.

Maluf, N. and Williams K., An Introduction to Microelectromechanical Systems *Engineering*, second edition, Artech House, Inc., 2004.

Wallace, J. L., Applications of sputtered thin films of magnetoelastic amorphous alloys, *Materials and Design* 14 (1993), pp. 285–289.

Chapter 4
MEMS Design Process and CAD Tools

This Chapter focuses on MEMS products design process and computer-aided design (CAD) tools. The first part summarises the characteristics of MEMS design process. In the second part, features of three leading MEMS CAD tools, CoventorWare, IntelliSuite, MEMS Pro (MEMS Xplorer) are presented. Several other modelling and simulation tools for assisting MEMS design are also briefly introduced. At the end of this Chapter, two different MEMS product design methodologies are defined. This is followed by the description of the design flow in CoventorWare and IntelliSuite.

4.1 Introduction

Demand for MEMS-based products has been increasing strongly in the aerospace, automotive, biomedical, defence, consumable, telecommunication and other industries during the last decade. However, although some MEMS products such as accelerometers, gyroscopes, switches, micro-mirrors, pressure sensor, and resonant sensors are well established, commercially available MEMS products are still relatively limited. It is recognised that the main reason is the overlong MEMS product design cycle which has hindered the growth of MEMS

application [Furlong, 2002]. As this design cycle is tightly related to product modelling, analysis, fabrication, and testing methodologies, this chapter will therefore introduce the characteristics of MEMS design process, MEMS design software packages, and two typical MEMS design flows.

4.2 Characteristics of MEMS Design Process

MEMS design process is different from conventional products design and has several unique characteristics.

Firstly, MEMS design requires the integration of related microfabrication processes. As MEMS fabrication technology normally combines physical and chemical treatment processes, it frequently involves a harsh environment such as high temperatures. This can have a significant effect on the performance of the whole system. For example, micro-fabrication processes can affect the tolerance of the finished components and the intrinsic effects such as stresses and strains. Therefore, the selection of fabrication technique for each step and the sequence of these steps has become an integral part of a MEMS design process.

Secondly, MEMS design needs the collaboration of experts in a wide range of classical areas. MEMS design is complicated and generally involves three major tasks including process flow design, electromechanical and structure design, and design verifications [Hsu, 2002]. These require the designers to have knowledge

in multiple disciplines such as microbiology, chemistry, electrical engineering, mechanical engineering, chemical engineering, physics, material sciences, computing sciences as well as experience in industry-specific applications [LaFrenz, 2003]. Obviously it is unusual for an individual to have all the necessary knowledge and expertise. Consequently, a large multidisciplinary design team which incorporates system designers, IC designers, process engineers, and MEMS experts is typically involved in MEMS product design.

Thirdly, MEMS design is an active reworking process [Zha, 2005]. This means it needs several iterations before the required functions and performances of a given device are finally fulfilled. Compared to its macro-scale counterpart, MEMS technology is still in its infancy. The information about material properties at micro level and the fundamental materials parameters which impact the behaviour of microstructures are still limited. Furthermore, there is a lack of standards in design, fabrication and test methodology in MEMS industry [LaFrenz, 2003]. No single facility is capable of handling the fabrication requirements for every MEMS application. For this reason, it is very difficult to predict the outcome of a particular design and the design process is always associated with a high degree of uncertainty.

Because of the inherent nature of MEMS design processes, computer technology that offers higher precision has become an integral part in the design and

manufacturing of MEMS products. The following section will focus on several MEMS modelling and simulation software packages.

4.3 MEMS Modelling and Simulation Tools

Nowadays CAD software packages are widely used for products designed to meet critical time-to-market condition. CAD tools enable designers to model and simulate whether design specifications are met by using virtual rather than physical experiments and therefore can significantly reduce the development and production cycle as well as the total costs. Furthermore, they provide the designer with immediate feedback on design decisions which, in turn, promise a more comprehensive exploration of design alternatives and a better performance of the final product.

A number of CAD software packages exist for conventional products design. However, because of the unique characteristics of MEMS design process which have been described earlier, specifically designed CAD tools are needed to fulfil these requirements. There are several CAD tools commercially available which can be used to assist MEMS designer on material and fabrication process selections, mask layouts, process emulations, and physical-level and system-level simulations. Among these MEMS tools, CoventorWare™ (previously known as MEMCAD) [Coventor, 2007], IntelliSuite™ [IntelliSense, 2007], and MEMS Pro™ [Softmems, 2007] are the leading software packages which are widely

adopted by universities and commercial MEMS developers. In the following sections, an overview of the functionality of these three tools will be given.

4.3.1 CoventorWare

CoventorWare™ is a software suite designed for MEMS, microfluidics and semiconductor process applications. It was originally developed at the Massachusetts Institute of Technology (MIT) in the late 1980s/early 1990s [Hsu, 2002]. In 1996, Microcosm Technologies (now renamed as Coventor Inc.) licensed the code from MIT and sold it commercially under the name MEMCAD.

CoventorWare consists of Materials Properties Database, Process Editor and five other modules: Architect, Designer, Analyzer, Integrator and MEMulator. The functions of these five modules are described as following [Coventor, 2006]:

Architect performs system-level design and simulation. System-level simulation is different from traditional physical-level simulation which is mainly based on finite element method (FEM) or boundary element method (BEM). It simulates the overall behaviour of a complete model rather than the interactive behaviour of many finite elements that comprise the model. The concept of system-level simulation provides a number of advantages over the physical-level simulation and the major advantage is that the simulation time can be reduced by orders of

magnitude. This allows MEMS designers to quickly explore design alternatives and optimise system performance.

Designer is a physical design tool for creating mask layouts and three dimensional (3D) solid models. The completed layouts can be exported into GDS, CIF, IGES, SAT, and DXF format files for mask and wafer fabrication. The 3D models can be imported into Analyzer for meshing and 3D domain and coupled simulation. Alternatively, the models also can be exported to third-party programs for solid model simulation.

Analyzer is a multi-physics field solver which includes electrostatic, mechanical, thermal, fluidic, and coupled solution components. Simulation adopts physical-level approach to compute different types of solutions, including capacitance, charge, mechanical stress and displacement, inductance, and damping effects calculations as well as modal, harmonic, thermal and mechanical transient, hysteresis, piezoelectric, piezoresistive, and package thermomechanical analyses.

Integrator is used to create macromodels, also called reduced-order models, from detailed models generated in Analyzer. These macromodels can be exported to industry-standard integrated circuits (IC) simulators such as Synopsys and Cadence for system-level simulation. This allows for rapid simulation of large

systems involving multiple component and physical domains such as electrical, mechanical, thermal, optical, and fluidic.

MEMulator is used to simulate the impact of fabrication process changes to the designed product. It can perform simulations on different material deposition methods such as physical vapour deposition (PVD), chemical vapour deposition (CVD) and wafer bonding etc., and material etching process including RIE, wet isotropic and anisotropic etch, and chemical and mechanical polishing (CMP) etc.

4.3.2 IntelliSuite

IntelliSuite™ was the first released commercialised MEMS CAD software package developed by IntelliSense Inc [Hsu, 2002]. It was designed for MEMS and microfluidics applications. Similar to CoventorWare, it has built-in material properties databases, process flow editor, mask layouts and 3D model generator and physical and system level simulators. The latest version IntelliSuite 8.5 consists of four parts: Clean Room, Design Tools, Multiphysics and System Simulation [IntelliSense, 2008].

In Clean Room, there are different modules for material databases (MEMaterial), process editing and certifying (IntelliFAB), and different etch process simulation (AnisE, RECIPE and IntelliEtch). AnisE is an anisotropic etch simulation module which can simulate different wafer orientations under different etchant

type, temperature, etch stops, etching time, and concentration parameters. RECIPE is used to simulate reactive ion etch (RIE) and inductive coupled plasma (ICP) etch processes. In addition, it has another unique feature which has the capability of performing an economic analysis for the designed product by using a module called MEMS Cost Mode. This helps managers and designers to understand the impact of the process flow, wafer yield, die size and die yield on the final cost of the production. In Design Tools, modules include IntelliMask for creating mask layouts and 3D Builder for solid model generation and meshing. Multiphysics consist of different physical simulation modules for mechanical, thermal, electrostatic, piezoelectric and electromagnetic analyses etc. IntelliSuite 8.5 has expanded its applications to Nano-Electro-Mechanical Systems (NEMS). The module Nano Simulation^{TM} can perform linear and non-linear static coupled Thermal-Electrical-Stress and Piezoresistive analysis on nanostructures such as Carbon Nano Tubes (CNTs) which are believed to have a potential to provide a breakthrough in a number of disciplines ranging from computing, displays, medical devices, sensing and telecommunications [Monthioux et al., 2006]. In System Simulation part, module SYNPLE is used to carry out the system-level simulation. System Model Extrator performs similar functions as module Integrator in CoventorWare which can build behaviour models from FEM models generated in MultiPhysics and significantly reduces the simulation time. Another feature of IntelliSuite 8.5 is that it can be integrated into electronic design applications (EDA) workflow.

4.3.3 MEMS Pro and MEMS Xplorer

MEMS Pro and MEMS Xplorer are two MEMS design suites provided by SoftMEMS Inc. SoftMEMS was the CAD Business Unit of MEMSCAP, a company providing MEMS-based products for the medical and aeronautic industry. In 2004, SoftMEMS acquired license from MEMSCAP to develop and market its CAD design tools for MEMS.

MEMS Pro was developed at Tanner Research in 1997. It is a PC-based integrated CAD tool suite for the design of microsystems coupled with electronics. MEMS Pro is based on two modules: (1) MEMS Pro DS for mask layout, 3-D solid model verification, and system-level simulation; (2) ROM for generating reduced order models. MEMS Xplorer was released in 2000. It is a customisable MEMS design suite for Unix-based platforms and has three main modules: MEMS Xplorer DS, MEMS Modeler and MEMS Master. They perform the similar functions as MEMS Pro. MEMS Pro is integrated on top of ANSYS and Tanner software tools: L-Edit and T-Spice; while MEMS Xplorer is on top of Cadence, ANSYS and Mentor Graphics.

SoftMEMS CAD tools are open-platform products that support leading electronic design automation environments used for integrated circuit (IC) development. They provide solutions which combines aspects of electronic design automation with mechanical, thermal, optical, electromagnetic and fluidic

CAD. The two tools allow data sharing between system designers, IC designers, process engineers and MEMS experts, permitting earlier and consistent design checks between multidisciplinary teams. Each of the tool suites has easy-to-use graphical interfaces for rapid design.

4.3.4 The Comparison of MEMS Design Tools

Both IntelliSuite and CoventorWare are based on the MEMS analysis tools developed by Professor Stephen Senturia at the Massachusetts Institute of Technology (MIT) in the 1990s. As a result, these two packages have similar structures and functions of their modules. For example, they all have material property databases, built-in design and simulation tools for creating fabrication process flow, mask layouts and 3D models as well as performing fabrication process check and simulation, physical-level and system-level simulation. As for MEMS Pro, because it was developed in Tanner Research, a company specialising in microelectronics design, it has the advantage of integration with EDA tools. MEMS Pro does not have simulation modules integrated in its package and has to be combined with other simulation tools. This can be an advantage for those customers who already have the required simulation tools installed in their systems as the training time can be significantly reduced. Another advantage of MEMS Pro over CoventorWare and IntelliSuite is the cost of license charge. Because it is built on top of several EDA design tools which are widely used in the electronics industry and this considerably brings down the

overall costs. Other differences of these three tools are listed in Table 4.1.

Table 4.1 The comparison of MEMS software packages

	CoventorWare	IntelliSuite	MEMS Pro
Company	Coventor	IntelliSense	SoftMEMS
Origination	MIT, Prof. S.Senturia, late 1980s/early 1990s	MIT, Prof. S. Senturia, late 1980s/early 1990s	Tanner Research, Dr. Maher, 1998
Built-in mask layout tools and physical and system-level simulators?	Yes	Yes	No, integrated on top of Tanner software tools such as L-Edit, S-Edit, W-Edit, T-Spice, and LVS etc.
Licence fee	£4619	£4396	£1434
Integration with EDA?	No	Yes	Yes
Fabrication process simulator?	Yes	Yes	No
Cost evaluation module?	No	Yes	No

4.3.5 Other CAD Tools for MEMS Design

Besides these three leading MEMS design tools, there are also some other tools which are widely used by MEMS designers. For example, I-DEAS, ProEngineer and Patran can be used for developing 3D models; ANSYS and Abaqus are employed for physical-level simulation; Saber, Matlab and Silvaco/SmartSpice can be used as system-level simulation tools. Zha [Zha, 2005] investigated these CAD tools and the results are shown in Figure 4.1.

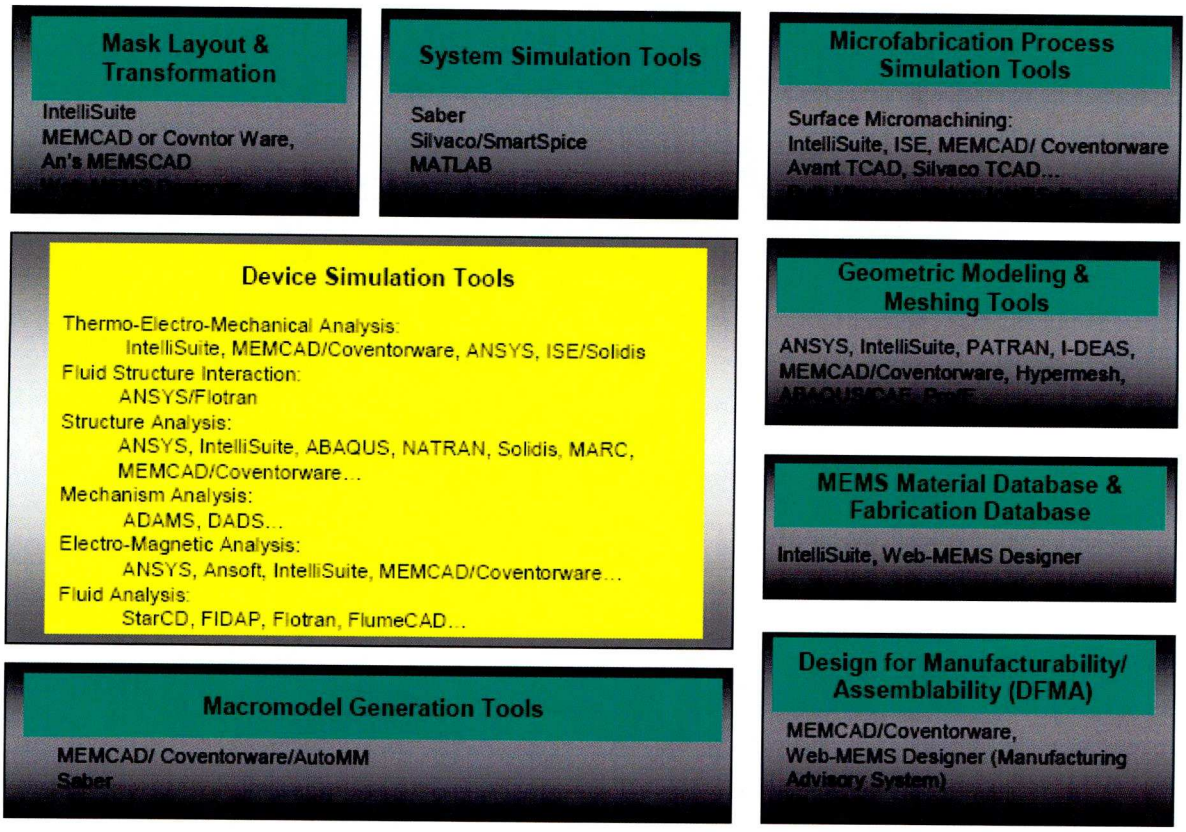

Figure 4.1 Modelling and simulation tools for MEMS design [Zha, 2005].

4.4 MEMS Design Flow

4.4.1 MEMS Product Design Level

Normally, the design of MEMS products can be divided into system, device, component, and element levels [Zha, 2005]. Here we use an airbag trigger as an example to explain these four levels:

An airbag deployment system in a car is used to protect the driver and passengers from injury in the event of serious vehicle collision. This system employs a microaccelerometer to measure the accelerations of the vehicle in different directions. Figure 4.2 illustrates a capacitive type accelerometer which consists of

springs, proof mass and electrostatic combs [Furlong, 2002]. The central part of the accelerometer is a micromechanical proof mass. It is attached to a reference frame using four folded spring pairs. The electrodes on the four sides of the proof mass and the reference frame form four capacitors in two different directions. When external accelerations are applied, the capacitances of these capacitors will change because of the change of relative position between these electrodes. Therefore, by measuring the capacitance change of these four capacitors the applied accelerations can be detected.

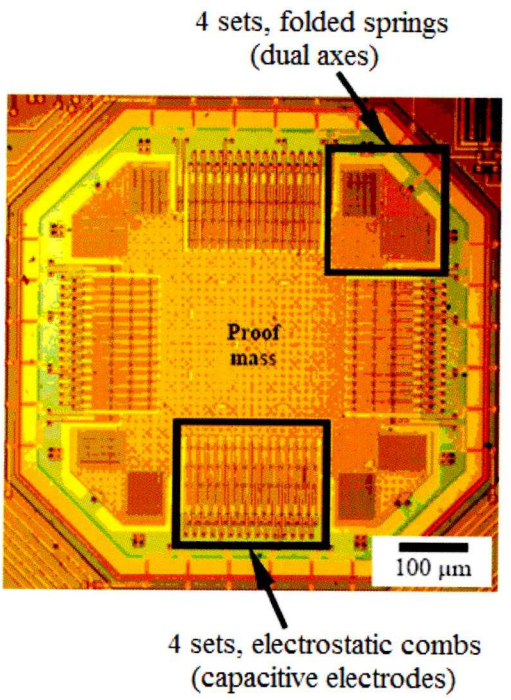

Figure 4.2 A capacitive accelerometer [Furlong, 2002].

The design of this product can be separated into three different stages. The design of the whole deployment system can be considered in system level. The modelling and simulation of the accelerometer is in device level. The development of the

springs and electrostatic combs is in component level. While the design of those beams which form the springs and combs is in element level.

4.4.2 Bottom-up and Top-down Design Flow

Two approaches are adopted for MEMS products design methodology: bottom-up and top-down flows [McCorquodale, 2003]. In the following section, the characteristics of these two approaches and the associated advantages and disadvantages are presented.

In a bottom-up approach, the design flow starts with detailed design of individual components. Components which play key roles in determining the final system performance and functionality will be specified in detail. They are then linked together to form larger subsystems, which then in turn are linked, sometimes in many levels, until a complete top-level system is formed. A top-down design starts from defining the required overall system specifications. These specifications are then described with first-level subsystems. Each subsystem can be further broken down into many additional subsystem levels until the entire specification is reduced to low-level functional elements. Then these elements are specified in great detail.

Bottom-up approach is a 'rather natural' design methodology. Current and past development approaches have been typically bottom-up [McCorquodale, 2003].

This approach is adequate for developing relatively simple systems. However, when developing large and complex system it may result in a tangle of elements and subsystems, developed in isolation, and subject to local optimisation as opposed to meeting a global purpose.

In top-down design, system components are derived from system specifications. The main advantage is that it strongly focuses on specific requirements which helps to make a design responsive to its requirement. Its disadvantage is that project and system boundaries tend to be application or specification oriented. As a result, the system is more likely to miss the benefits of a well structured, simple architecture [Graham, 2001]. Top-down design approach is usually possible only when the designers have a very clear idea of the problem and how to solve it.

4.4.3 MEMS Design Flow in IntelliSuite and CoventorWare

IntelliSuite adopts a bottom-up design flow. Figure 4.3 shows the whole design process [Finch, 2002]. The design process begins with the design of a process flow. This can be a flow selected from a database of standard foundry templates which is provided in the software, or a custom process flow constructed from the database of individual process steps. Mask sets are then created in the IntelliMask module or imported in DXF, GDSII, or bitmap file formats from third-party programs. The verification of the process and mask design are performed using IntelliFAB, AnisE and RECIPE for process simulation. Then the

designer uses 3D Builder to generate and mesh the 3D model which is in turn analysed using different FEA tools. The system-level simulation is carried by SYNPLE which simulates reduced-order models extracted by SME, the system model extractor in IntelliSuite.

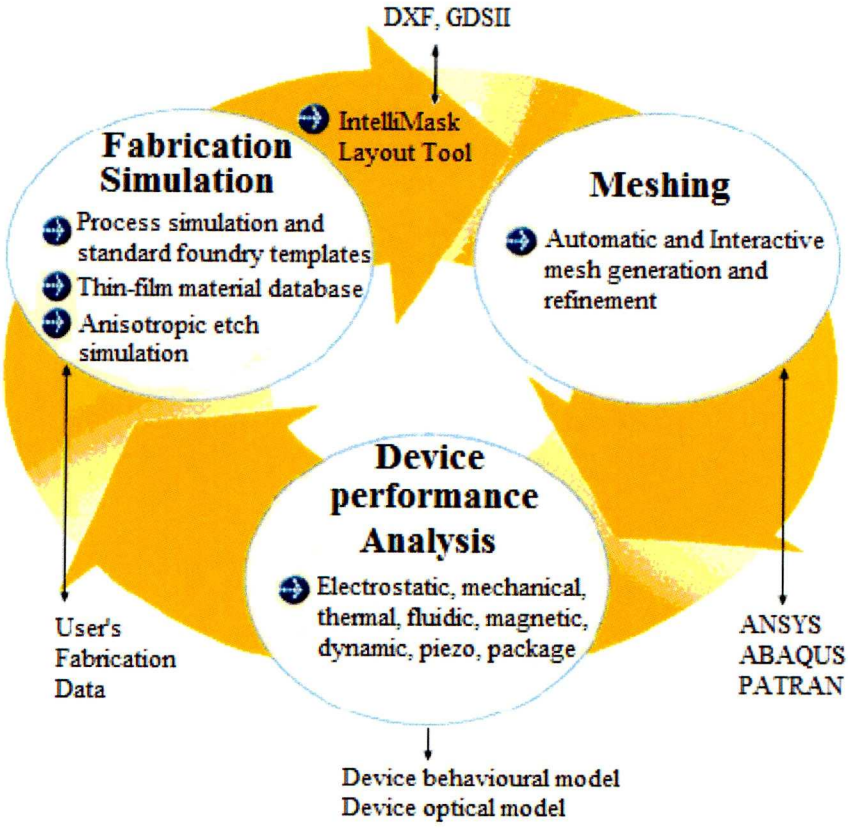

Figure 4.3 Product design flow in IntelliSuite [Finch, 2002].

The design flow in CoventorWare is different from that in IntelliSuite. It supports both top-down and bottom-up design flows. A typical design process in CoventorWare normally starts from specifying the requirements of the proposed MEMS product. The designer then chooses components from the Parametric Library to create a schematic of the desired system configuration. This includes

the MEMS components to be fabricated and other system parts such as drive and sense circuitry, etc. When the schematic capture is complete, the design is netlisted into a format used for simulation and layout extraction. Then Saber, a powerful behavioural system-level simulator module from Synopsys Inc., is used to perform the system-level simulation. This simulation is iterative as the designer normally needs to adjust the geometric or material property parameters of individual components in the schematic, or to change or rearrange the components for optimal performance. After the proof of the final design, the netlist is used to create the 2D layout and 3D model in order to perform detailed analysis.

Alternatively, the design can start from creating a 2D layout in Layout Editor or importing it in CIF, DXF, or GDSII format files created in third-party program. 3D model is then generated for the 3D domain and coupled simulations. The parametric study function provided by CoventorWare is used to optimise the design. This is followed by extracting macromodels from these detailed models using Integrator for system-level simulation. The design flow in CoventorWare is shown in Figure 4.4 [Coventor, 2006].

CoventorWare was used to design and simulate the proposed sensor. Simulations were performed only using physical-level approach because of the relatively simple structure of the sensor as well as the limited resources during the research

(no license was held for the Architect module). The design process and simulation results will be shown in Chapter 5.

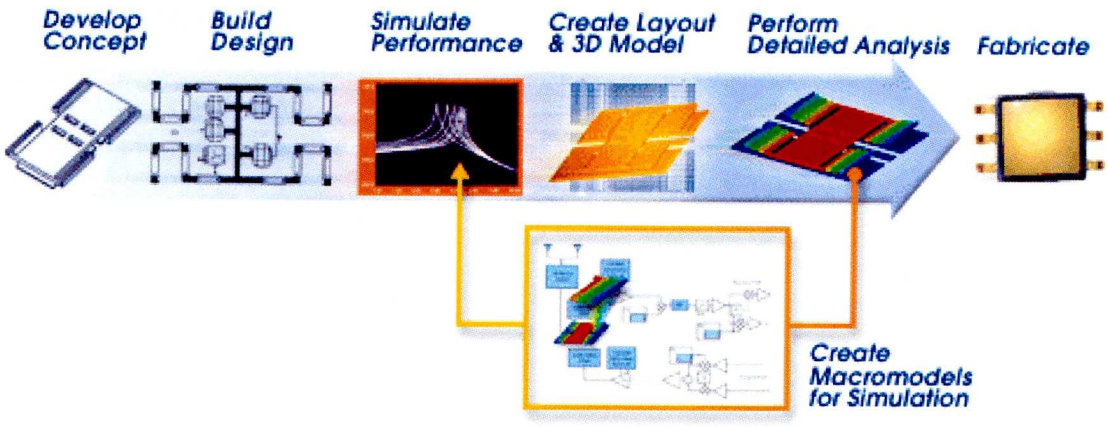

Figure 4.4 CoventorWare components and design flow [Coventor, 2006].

References

Coventor, Websit: http://www.coventor.com, accessed in August 2008.

CoventorWare 2006, Documentation.

Finch N., Marchetti J., and Swiecki A., Intellisense Corporation, Incorporating CAD for MEMS tools into the academic environment, *ASME International Mechanical Engineering Congress and Exposition*, 2000, pp. 1-6.

Furlong C., Pryputniewica R. J., and Yokum J. S., Optimization of optical methodology for high-digital resolution quantitative evaluation of reliability of microelectronics and packaging, *Proceeding of ASME International Mechanical Engineering Congress & Exposition*, New Orleans, Louisiana, Nov. 2002, pp. 1-7.

Graham I., *Object-oriented methods (3rd Edition) : Principles & Practice*, Publisher Addison-Wesley Longman Publishing Co., Inc., Boston, MA, USA, 2001.

Hsu T. R., *MEMS & Microsystems Design and Manufacture*, McGraw-Hill, Inc., 2002.

IntelliSense, Website: http://www.intellisense.com, accessed in August 2008.

LaFrenz J., et al., Starting from scratch: creating an information technology infrastructure for MEMS-related research and development, *Information Theories & Application*, Vol. 10, 2003, pp. 330.

McCorquodale M. S., Gebara F. H., et al., A Top-Down Microsystems Design Methodology and Associated Challenges, *Proceedings of the conference on Design, Automation and Test in Europe : Designer's Forum*, vol. 2, 2003, pp. 20292.

Monthioux M., Kuznetsov V. L., Who should be given the credit for the discovery of carbon nanotubes? *CARBON*, Volume 44, Issue 9, August 2006, Pages 1621-1623;

SoftMems, Website: http://www.softmems.com, accessed in August 2008.

Zha X. F., Sriram R. D., and Gupta S. K., Information and knowledge modelling for computer supported micro electro-mechanical systems design and development, *Proceedings of ASME Design Engineering Technical Conference*, Sep. 2005, Long Beach, California, 2005, pp. 1-11.

Chapter 5
Design and Modelling of Inductor-Capacitor Resonant Pressure Sensor

In this chapter, the design, modelling and optimisation of an inductor-capacitor (*LC*) resonant type pressure sensor will be presented. First, in section 5.1 the principles of passive power transmission, sensor operation and external device (reader) detection in an *LC* pressure sensing system are reviewed. In section 5.2, the considerations of choosing the system operating frequency are presented. Section 5.3 deals with design and modelling of two planar spiral coils. Analytical model of these coils is established to optimise the design. Two square spiral coils constructed on silicon and glass substrates are investigated. Section 5.4 shows the proposed sensor structures. In Section 5.5, the reasons for selecting the materials for the sensor components are explained. The design of the pressure sensing diaphragm, i.e., the movable electrode of the capacitance-variable, parallel plate capacitor is introduced in Section 5.6.

5.1 Theory of Wireless *LC* Resonant Pressure Sensor System

As described in Chapter 2, a wireless inductor-capacitor (*LC*) resonant type pressure sensor consists of an inductor and a capacitor to form a resonant circuit.

This circuit oscillates electrically when subjected to a time varying electromagnetic field according to Faraday's Law. The amplitude of this oscillation reaches its highest value when the frequency of the applied electromagnetic field approaches the resonant frequency of the circuit. The capacitor is configured in such a way that its capacitance changes as the surrounding pressure is varied. The change of capacitance will alter the resonant frequency of the sensor. By detecting this frequency change, the pressure information can be acquired.

The concept of the *LC* resonant type sensor for wireless pressure measurement is not new and has been proposed in previous researchers. However, this method suffers from limited detection distance due to the inefficiency of power transmission within the system. In order to achieve a maximal detection range, considerable research efforts have been focused on improving the link efficiency between the sensor and the reader [Rosengren, 1994; Lee, 2001; Ong, 2001; DeHennis, 2005]. Although different strategies were suggested, the common research goal was to develop planar spiral coils with high quality factors. The characterisation of planar spiral coils will be presented in Section 5.3.4 of this Chapter. First the mechanism of inductive coupling and the detection principle of the pressure sensing system are described.

5.1.1 Principle of Inductive Coupling

Inductive coupling refers to the transfer of energy from one circuit component to another through a shared magnetic field. Figure 5.1 shows the inductive link between two coupled coils [Johnson et al., 1999].

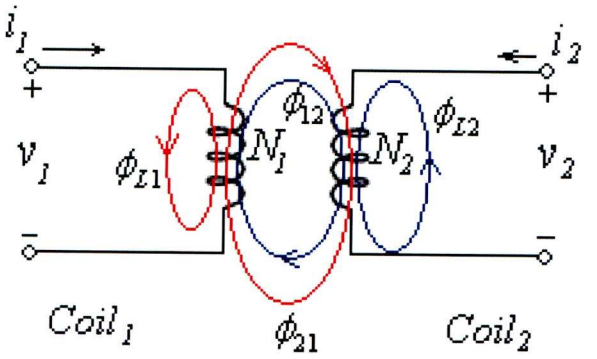

Figure 5.1 Two inductively coupled coils [Johnson et al., 1999].

When a current i_1 flows through Coil 1 (primary coil), a magnetic field is produced and it generates magnetic flux ϕ_1 (represented by the red lines in Figure 5.1). This magnetic flux is the sum of flux ϕ_{L1} through Coil 1 and flux ϕ_{21} through Coil 2. Therefore, the total magnetic flux generated by Coil 1 can be written as,

$$\phi_1 = \phi_{L1} + \phi_{21} \tag{5.1}$$

The magnetic flux through Coil 2 will induce a voltage according to Faraday's Law. This voltage results in a current i_2 flowing through Coil 2 which in turn produces a magnetic field. This magnetic field also generates magnetic flux ϕ_2 (blue lines in Figure 5.1), part of which passes through Coil 1 (ϕ_{12}) and the other

part does not (ϕ_{L2}) as represented by Equation 5.2.

$$\phi_2 = \phi_{L2} + \phi_{12} \tag{5.2}$$

Therefore, the total magnetic flux ϕ_1^T through one loop of Coil 1 is the sum of flux components due to i_1 and i_2:

$$\phi_1^T = \phi_{L1} + \phi_{21} + \phi_{12} = \phi_1 + \phi_{12} \tag{5.3}$$

The total flux linkage λ_1 in Coil 1 is:

$$\lambda_1 = N_1\phi_1^T = N_1\phi_1 + N_1\phi_{12} \tag{5.4}$$

The relationship between the current flowing in a coil and the generated magnetic flux is:

$$i = \frac{N\phi}{L} \tag{5.5}$$

where N is the number of turns of the coil and L is the coil's self-inductance. The flux linkage part $N_1\phi_{12}$ due to i_2 is related to the mutual inductance M between these two coils and can be expressed as:

$$N_1\phi_{12} = \pm Mi_2 \tag{5.6}$$

The sign '$\pm$' accounts for different directions of current flows in the two coupled coils. Substituting Equations 5.5 and 5.6 into Equation 5.4, The following equation is obtained:

$$\lambda_1 = L_1 i_1 \pm Mi_2 \tag{5.7}$$

Similarly, the total magnetic flux linkage in Coil 2 can be written as:

$$\lambda_2 = L_2 i_2 \pm Mi_1 \tag{5.8}$$

where L_1 and L_2 in the above two equations are self-inductance of Coil 1 and Coil 2, respectively. According to Faraday's Law, the relationship between a

varying magnetic field and the induced voltage in a conductor is given by:

$$\oint \bar{V} \cdot d\bar{l} = -\int_s \frac{\partial \bar{B}}{\partial t} \cdot d\bar{s} \tag{5.9}$$

Applying this equation to a coil, the voltage drop across the two terminals of the coil can be expressed in terms of the change of the magnetic flux linkages $N\phi$ with respect to time t as follows:

$$V = -\frac{d}{dt} \int \bar{B} \cdot d\bar{s} = -\frac{d(N\phi)}{dt} \tag{5.10}$$

Equation 5.10 can be used to calculate the voltage drops across in Coil 1 and Coil 2:

$$v_1 = \frac{d(\lambda_1)}{dt} = L_1 \frac{di_1}{dt} \pm M \frac{di_2}{dt} \tag{5.11}$$

$$v_2 = \frac{d(\lambda_2)}{dt} = L_2 \frac{di_2}{dt} \pm M \frac{di_1}{dt} \tag{5.12}$$

These two equations can be used to calculate the voltage drops in the proposed sensor and in its reader. Figure 5.2 shows the electrical model of the sensor and the reader [Johnson, et al., 1999].

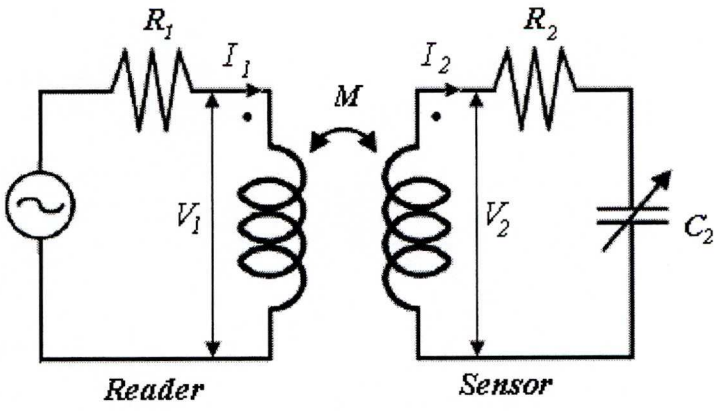

Figure 5.2 Electrical model of the *LC* resonant sensor with readout circuit [Johnson, et al., 1999].

Here the excitation voltage in the reader is assumed to be a sinusoidal waveform with angular frequency of ω. The voltage drop in the reader and the sensor can be derived from Equations 5.11 and 5.12:

$$V_1 = j\omega L_1 I_1 - j\omega M I_2 \tag{5.13}$$

$$V_2 = -j\omega L_2 I_2 + j\omega M I_1 \tag{5.14}$$

The load impedance Z_s of the sensor can be expressed as

$$Z_s = R_2 - \frac{j}{\omega \cdot C_2} \tag{5.15}$$

where R_2 and C_2 denote the resistance and capacitance of the sensor's resistive and capacitive components, respectively. As $V_2 = I_2 Z_s$, Equation 5.14 can be rewritten as:

$$I_2 = \frac{j\omega M I_1}{R_2 - \frac{j}{\omega \cdot C_2} + j\omega L_2} \tag{5.16}$$

Taking Equation 5.16 into Equation 5.13, the following equation is derived:

$$V_1 = j\omega L_1 I_1 + \frac{\omega^2 M^2 I_1}{R_2 + j\left(\omega L_2 - \frac{1}{\omega \cdot C_2}\right)} \tag{5.17}$$

Equation 5.17 expresses theoretically the voltage drops on the reader side. When M=0, that is, there is no coupled coil around the reader antenna, the voltage at the terminals of the antenna is given by the first term of Equation 5.17. When the reader is coupled with the LC sensor coil, the magnitude of voltage change is determined by the second term of the equation.

5.1.2 Reader Detecting Principle

From the previous section, it was shown that when the LC resonance sensor enters the time-variant magnetic field of the reader antenna, a change can be detected in the voltage across the reader coil. The detection of this voltage change is accomplished through monitoring the impedance change in the reader antenna.

The impedance of the reader $Z_r^{\ 0}$ in the absence of the sensor is given by the following equation:

$$Z_r^{\ 0} = R_1 + j\omega L_1 \tag{5.18}$$

However, during operation, the impedance on the reader side becomes:

$$Z_r^{\ C} = R_1 + j\omega L_1 + \frac{\omega^2 M^2}{R_2 + j\left(\omega L_2 - \frac{1}{\omega C_2}\right)} \tag{5.19}$$

At resonant frequency ω_0, i.e. $\omega = \omega_0 = \frac{1}{\sqrt{L_2 C_2}}$, the impedance of the sensor becomes purely resistive [Akar, 2001], which means that the impedance is reduced to R_2. Therefore, the impedance of the reader antenna at ω_0 becomes:

$$Z_r^{\ C}(\omega_0) = R_1 + j\omega_0 L_1 + \frac{(\omega_0 \cdot M)^2}{R_2} \tag{5.20}$$

During operation, a periodic signal, whose frequency is varied over a range around the sensor resonant frequency, is generated to interrogate the sensor. The impedance of the reader antenna is then monitored. At a specific frequency corresponding to the resonant frequency of the sensor, an abrupt change of the

impedance will occur. This resonant frequency is then detected and this provides the information about the pressure to which the sensor is subjected.

The change is more easily detected if the phase of the impedance is monitored. The approximate magnitude of the impedance phase dip $\Delta\varphi_{dip}$ is given by Equation 5.21 [Akar, 2001].

$$\Delta\varphi_{dip} \cong \tan^{-1}\left(\frac{\omega_0 M^2}{L_1 R_2}\right) \tag{5.21}$$

5.2 Selection of System Operating Frequency

The selection of the system operating frequency, and therefore the sensor resonant frequency, is vitally important in the design of an *LC* type pressure sensor because the sensor configuration, system detection range, external reader cost, and operating safety are all influenced by this parameter. Several issues need to be taken into account when selecting the sensor operating frequency which will be discussed below.

5.2.1 Operation Safety

During operation, the proposed *LC* resonant type pressure sensor will be subjected to an electromagnetic field. Therefore, it is necessary to consider the biological effects of the electromagnetic field on the body.

Tissue warming is the most prominent biological effect induced by electromagnetic field. An *LC* resonant pressure sensor operates in the radio frequency (RF) range. The RF spectrum is divided into eight bands according to the wave's frequency (Table 5.1). Each band is associated with different energy and other characteristics [Hickman, 2006]. The SHF and EHF bands are often referred to as the microwave spectrum. The energy of RF waves is relatively low and is unlikely to cause any ionisation, which can break the DNA molecules of a living cell and damage the tissue. However, this energy can be converted into thermal energy, resulting in tissue warming.

Table 5.1 Radio Frequency Spectrum [Hickman, 2006]

Designation	**Abbreviation**	**Frequencies**
Extremely Low Frequency	ELF	3Hz – 30Hz
Super Low Frequency	SLF	30Hz – 300Hz
Ultra Low Frequency	ULF	300Hz – 3kHz
Very Low Frequency	VLF	3kHz - 30kHz
Low Frequency	LF	30kHz -300kHz
Medium Frequency	MF	300kHz - 3MHz
High Frequency	HF	3MHz - 30MHz
Very High Frequency	VHF	30MHz - 300MHz
Ultra High Frequency	UHF	300MHz - 3GHz
Super High Frequency	SHF	3GHz - 30GHz
Extremely High Frequency	EHF	30GHz - 300 GHz

The concept of penetration depth can be used to describe the effect of different frequency of electromagnetic field to the body. An electric field E passing

through a medium of conductivity σ can generate heat at a rate of σE^2.

Table 5.2 EM waves penetrating depth in human tissue [Johnson, 1972]

Frequency (MHz)	**Muscle, skin and tissues with high water content**		**Fat, bone and tissues with low water content**	
	σ (mS/m)	Penetration depth (mm)	σ (mS/m)	Penetration depth (mm)
1	400	913	--	--
10	62.5	216	--	--
27.12	612	143	10.9 – 43.2	1590
40.68	693	112	12.6 – 52.8	1180
100	889	66.6	19.1 – 75.9	604
200	1280	47.9	25.8 – 94.2	392
300	1370	38.9	31.6 – 107	321
433	1430	35.7	37.9 – 118	262
750	1540	31.8	49.8 – 138	230
915	1600	30.4	55.6 – 147	177
1500	1770	24.2	70.8 – 171	139
2450	2210	17	96.4 – 213	112
3000	2260	16.1	110 – 234	97.4
5000	3920	7.88	162 – 309	66.7

Penetration depth is defined as the distance at which the power density of the propagating wave decreases to $1/e^2$ of its value at the surface of the body [Johnson, 1972]. Table 5.2 shows the influences of different body parts on penetration depth. The penetration depth decreases with operating frequency, which indicates that RF waves at high frequencies are more likely to be absorbed

and may therefore to cause more tissue warming. Finkenzeller reported that the absorption rate of 100 kHz RF waves for water or non-conducting substances is lower by a factor of 10^5 than it is at 1 GHz [Finkenzeller, 2003].

5.2.2 Detecting Range

The detecting range of the sensing system is dependent upon several factors such as the reader antenna configuration, sensor power consumption, operating power of the reader, system sensitivity etc. The system operating frequency greatly affects the achievable sensor detecting range.

In general, sensors operating at low frequencies have less communication ranges than those operating at high frequencies. This is because higher frequency is associated with greater energy and thus the RF signal can travel a longer distance. The data transfer rate is also affected by operating frequencies. Lower frequencies have slower data transfer rates. Passive radio frequency identification (RFID) systems operate in radio frequency ranges which employ a similar principle to that of an *LC* resonant sensor. Table 5.3 shows the communication ranges of passive RFID systems at different operating frequencies from LF band to microwave band [Finkenzeller, 2003]. It can be seen clearly that systems operating at microwave band have much longer communication distance than systems at low operating frequencies.

Table 5.3 Communication Range for Passive RFID Systems [Finkenzeller, 2003]

Frequency Band	**Common Frequency**	**Communication Range**
LF	125 to 135 kHz	20 to 100 cm
HF	13.56 MHz	10 to 70 cm
UHF	868 to 928 MHz	3 to 10m
Microwave	2.45 GHz	3m to 30m
(SHF & EHF)	5.8 GHz	3m to 100m

5.2.3 Sensor Size

The selection of the operating frequency is also restricted by the sensor size. Equation 2.2 indicates that the resonant frequency of an *LC* type pressure sensor is inversely proportional to the inductance and capacitance of the sensor components. Consequently, if a sensor is chosen to operate at low resonant frequencies, then its inductance or capacitance will have to be large. However, large inductance or capacitance is usually associated with a large physical size. For example, the increase of a coil's inductance is often achieved by increasing the number of turns. If the coil's line width and spacing have been determined, increasing the number of turns will result in a larger coil size. As the available space for the coil is limited, the allowable size of the sensor is an important consideration in the choice of the sensor operation frequency.

5.2.4 Interference and Licensing

The proposed sensor system generates and radiates electromagnetic waves and is legally classified as a radio system. The use of RF spectrum is governed by legislation. To avoid the possible interference from and to nearby radio frequency users such as television or mobile telephone, the sensor system requires a license from authorised organisations such as European Conference of Postal and Telecommunications Administrations (CEPT) in Europe or the Federal Communications Commission (FCC) in the United States. An alternative is to operate the sensor system in an unlicensed frequency band. There is a frequency range reserved specifically for industrial, scientific or medical applications known as the ISM band. The ISM frequency band in European Union and the United States is set to 402-405MHz for ultra low power medical implants [Finkenzeller, 2003]. It is also known as Medical Implant Communications Service (MICS) band in America.

The required minimum communication distance for the proposed sensor system is approximately 30 to 40cm. Over this short distance, it is unlikely to interfere with other radio services. Therefore, the only requirement is to eliminate disruptions from other radio frequency signals especially when the sensor is for home-based medical monitoring.

In conclusion, the operating frequency of the sensor can be chosen from LF to UHF bands. When operating at low frequency bands, the sensor is unlikely to cause any biological problems to the patient. However, the communication distance between the reader and the sensor will be too limited. Another disadvantage associated with low operating frequencies is the requirement of large sensor size, which is not acceptable for this application where small size is an essential requirement. In contrast, a sensor operating at high frequencies is more easily detectable even over large distances. Another important advantage is that it can be made smaller so that it can be easily deployed in the aorta. The potential disadvantages include tissue warming and higher cost of the reader system. Considering the tradeoffs between energy absorption by the tissue and maximal communication distance, it was proposed that the sensor should be designed to work in HF band at 10-20MHz.

5.3 Design of the Coil

The inductive component is the most important part in an *LC* type pressure sensor since it is directly related to the system power transmission efficiency. This inductive component can be a wire-wound coil or a micro-fabricated coil which is integrated in a substrate such as silicon, glass or gallium arsenide (GaAs). However, a wire-wound coil is too bulky and is therefore unsuitable for implantation in the body. In addition, it requires extra bonding and packaging steps to be connected with other components of the sensor. Hence an integrated

coil is the only choice for the inductive component of the sensor. Nevertheless, due to the planar fabrication process, integrated coils suffer from less flexible layouts and noticeable parasitic effects(see Section 5.3.4.1), namely parasitic resistance and capacitance, which can significantly decrease the power transmission efficiency. Hence one of the main objectives of this project is to develop an integrated micro-coil with low parasitic resistance and capacitance.

5.3.1 Inductor Metrics

An inductor is a component which stores energy in the form of magnetic field. It has an associated inductance and quality factor. Inductance measures how much energy can be stored in this inductor while the quality factor acts as a metric of the energy storage efficiency.

5.3.1.1 Inductance

From Ampere's Law, a current flowing through a conductor produces a magnetic field. This time-varying magnetic filed is capable of producing a flow of current through another conductor – this is called inductance. The inductance L of an inductor is defined as the ratio of the total magnetic flux linkage to the current I through the inductor [Finkenzeller, 2003]:

$$L = \frac{N\phi}{I} \tag{5.22}$$

where N is the number of turns of the coil and ϕ is the magnetic flux. The inductance of an inductor can be simply expressed as:

$$L = \frac{2E_s}{I^2} \tag{5.23}$$

where E_s is the energy stored in the magnetic field.

The inductance of a coil depends on its physical characteristics. From Greenhouse's Theory, inductance can be separated into two parts, i.e., self inductances of metal lines and mutual inductances between these lines [Greenhouse, 1974]. The mutual inductance is positive when the currents flow in the same direction in the lines and negative for currents in the opposite directions. Therefore, a coil has more inductance than a straight wire of the same material and a coil with more turns has more inductance than a coil with fewer turns.

5.3.1.2 Quality Factor

Quality factor is a property associated with all energy storage elements. Fundamentally, it represents the ratio of the amount of energy stored in a device to the amount of energy dissipated in that device. The quality factor Q is generally defined using the energy stored per cycle and the energy dissipated per cycle as:

$$Q = 2\pi \frac{E_{stored}}{E_{dissipated}} \tag{5.24}$$

Depending on the specific application, quality factor can be defined in terms of impedance, bandwidth and phase definition [Peter, 2004]. According to the bandwidth definition, the quality factor Q of a coil can be expressed as follows:

$$Q = \frac{\omega_0 L}{R} \tag{5.25}$$

where ω_0, L and R are the angular intrinsic resonant frequency, self-inductance and resistance of the coil, respectively. For an LC resonant sensor, the quality factor is a measure of the efficiency of the receiver coil. The higher the quality factor, the better the performance with respect to the energy transmission.

5.3.2 Layout of the Integrated Coil

The fabrication of integrated coils for power transfer has been reported in literature [Yue, 1999; Lee, 2001; Danesh, 2002; Wan, 2003]. Different configurations were suggested by these researchers in order to construct integrated coils with high quality factor. There are several topologies available for the layout of the integrated coils such as solenoid, square spiral, circular spiral and multi-layer types etc. These coil topologies will be compared with the aim of selecting the most suitable coil layout for this project.

5.3.2.1 Spiral versus Solenoid Design

An integrated coil can be configured in different geometries such as loop, meander, spiral or solenoid inductors as shown in Figure 5.3 [Carchon, 2003]. Assuming that these four inductors are constructed with the same conductive material and the same length, those with the spiral and solenoid configurations will exhibit much higher inductances than the other two configurations. This is because the positive mutual inductances between the segments of these two

inductors are much higher. Solenoid type inductors can provide larger inductance than spiral type inductors. However, because of the planar fabrication feature of MEMS technology, its fabrication process is far more complicated than that of planar spiral inductors. In addition, the realisation of a solenoid inductor on a substrate needs the building of a large number of vertical lines to connect the planar metal lines lying on each layer. This may introduce prohibitively large resistance values. As for spiral inductors, the nearest metal lines exhibit positive mutual inductance with each other. This allows spiral inductors to create a larger inductance within a given area than other planar layouts.

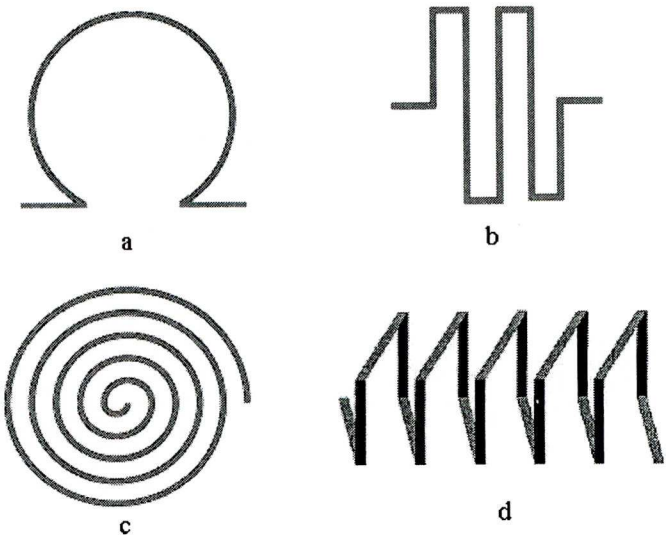

Figure 5.3 Layout topologies of (a) loop inductor; (b) meander inductor; (c) spiral inductor; (d) solenoid inductor [Carchon, 2003].

5.3.2.2 Spiral N-Side Polygon versus Circular Design

Several topologies exist within the domain of spiral inductors. The spiral inductor can be constructed as circular or *n*-sided polygon shape (n≥3). Research

has shown that polygon spiral coils with high value of n and circular spiral coils can produce coils with the highest quality factor and with very uniform magnetic fields [Pieters, 2001]. This is because the sharp corners of low n value polygons result in sharp field discontinuities at these corners. Therefore, circular and high value of n sides polygon spiral shapes are preferred. However, the actual shape of the coil is restricted by another factor. After the completion of wafer-level fabrication, sensors will be separated from the wafer using a process called wafer dicing [Maluf, 2000; Miller, 2005]. The dicing process is accomplished by laser cutting or mechanical sawing, as shown in figure 5.4. Due to this feature, although MEMS components can be any shape generated by straight lines, the most common shapes are rectangular or square.

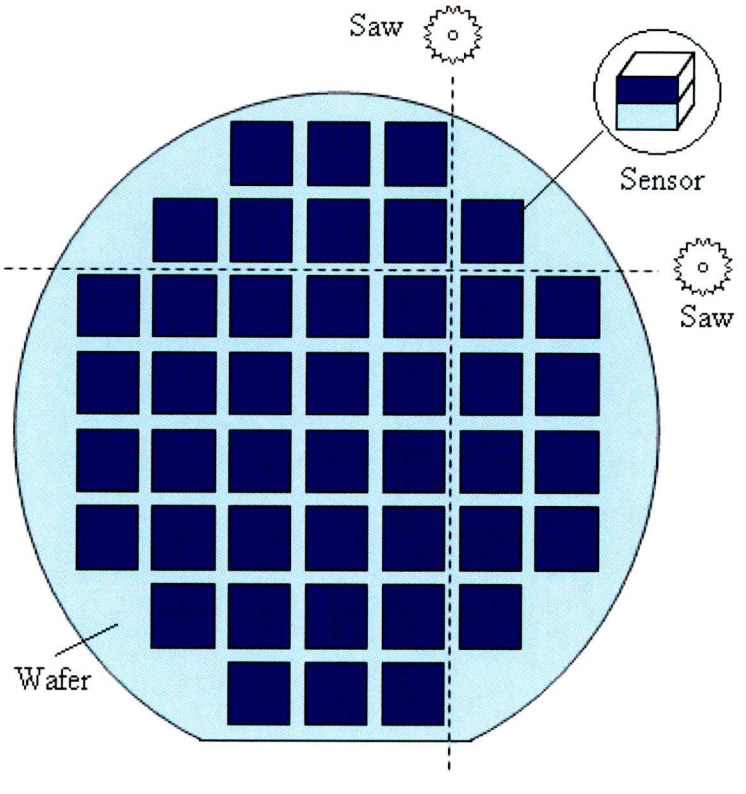

Figure 5.4 Schematic of MEMS micromachining process.

Carchon compared the inductance of a circular spiral coil and a square spiral coil with equivalent areas [Carchon, 2003]. These two coils have the same cross section of metal line and the same distance between two adjacent lines. In the case when the square coil is fabricated on a square substrate while the circular coil is on a circular shape substrate (Figure 5.5a), it was found that the circular coil has higher inductance and quality factor than that of the square one. When both of the two spiral coils are constructed on square substrates with equivalent areas (Figure 5.5b), Carchon found that the square spiral coil had higher inductance per unit area than the circular one.

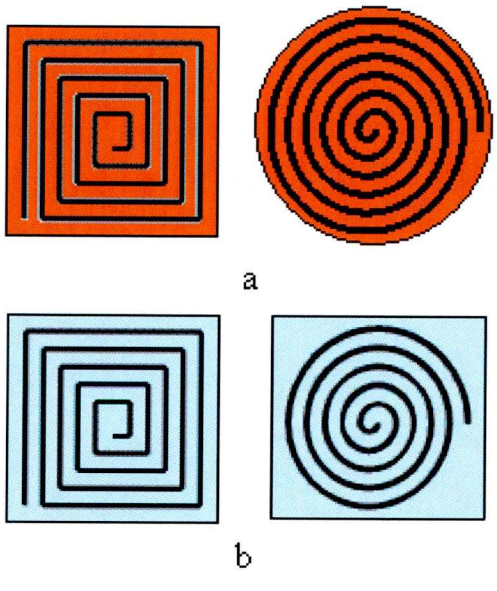

Figure 5.5 A square spiral coil and a circular coil with equivalent area consumption. (a) coils on square and circular substrates; (b) coils on two square substrates.

5.3.2.3 Square versus Rectangular Design

Chapter 1 indicates that the maximum allowed width and length of the sensor are

about 6mm and 10mm, respectively. So the coil can be constructed as a square shape (6mm×6mm) or a rectangular shape (6mm×10mm). The advantage of a rectangular coil is that a larger inductance, and therefore a higher quality factor, can be achieved compared with a square one. However, as mentioned in Section 1.3.2, the proposed sensor was designed to be delivered into the aneurysm sac from a small incision of the femoral artery, a sensor with rectangular shape will be more difficult to be delivered through the artery than a square sensor. This is because during this process, the position of the sensor needs to be constantly adjusted so as to go through the winding artery path smoothly to reach the aneurysm sac. Therefore, a square spiral coil was chosen for this project.

5.3.2.4 Single-layer Square Spiral versus Multi-layer Square Spiral Design

For a given area, the square spiral coil can be designed as multi-layer structure using additional metallisation. Figure 5.6 shows a two-layer square spiral coil which is formed by two single square spiral coils connected in series.

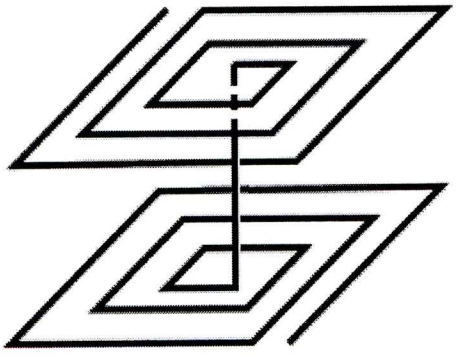

Figure 5.6 Layout of a two-layer coil.

The advantage of this layout is that in a limited planar area, an inductor with higher inductance can be realised compared to a single-layer coil. This results from the positive mutual inductance between the metal lines of these spiral coils on each layer. However, the parasitic capacitive coupling between these single-layer coils can greatly reduce the self-resonant frequency of the coil [Peters, 2004]. Therefore, when the coil is connected to a tuning capacitor to form an *LC* resonant circuit, the resonant frequency of this circuit will be affected by the capacitances of the tuning capacitor and the coil. As a result, the sensitivity of this circuit in response to capacitance changes of the tuning capacitor will be reduced.

5.3.3 Loss Mechanisms in Spiral Coils

In order to establish a physical model to characterise the square spiral coil, the loss mechanisms in spiral coils need to be fully investigated. These include eddy currents, skin effect and proximity effect.

5.3.3.1 Eddy Currents

An alternating current moving through a conductive material will create an alternating magnetic field around it. If this field is intersected by a nearby conductor, a small circular current will be induced within the conductor. These circular currents are called eddy currents. The induced eddy currents create alternating magnetic fields to oppose the change of the original alternating

magnetic field, resulting in a loss in efficiency with which the field can change direction [Peters, 2004].

Eddy currents dissipate energy in the form of heat as they flow through the conductor. The higher the operating frequency, the stronger the induced magnetic field. Consequently, the current that is induced will be greater and hence more energy will be dissipated. Therefore, in order to increase the efficiency of energy transmission, it is preferable to operate the wireless pressure sensor at low frequencies.

5.3.3.2 Skin Effect

The skin effect refers to the phenomenon that an alternating current tends to distribute itself on the surface of a conductor rather than in its core. It is caused by eddy currents which produce opposing magnetic fields in a conductor. When at high frequencies, these opposing fields are strongest in the centre of the conductor, causing the current density in this region to decrease sharply. As a result, currents flow on the surface of the conductor and the effective electrical resistance is increased.

Skin depth is used to describe how deeply the current and magnetic flux can 'penetrate' into a material. At an operating frequency of ω, the skin depth δ of a material can be calculated by the following equation [Cheng, 1989]:

$$\delta = \sqrt{\frac{2\rho}{\omega \cdot \mu}} \tag{5.26}$$

where μ is the magnetic permeability of the substance in which this material is placed and ρ is the electrical resistivity of the material.

Skin effect in a conductor at a particular frequency can be ignored if the skin depth is significantly larger than the thickness of the conductor. For this reason, the radius of metal lines in a coil is normally designed to be smaller than the skin depth at operating frequencies. As an example, consider a spiral coil with copper lines operating at a frequency of 20MHz. From Equation 5.26, the skin depth of the copper wire is calculated to be 14.66μm (the resistivity of copper is approximately 1.7×10^{-8} Ω.m, and magnetic permeability of air is 1.26×10^{-6} H/m). If the width and thickness of the copper lines are designed to be less than 2×14.66μm, then the frequency dependent resistance of the coil will be negligible. However, other constraints also need to be taken into account when determining the actual line thickness or width.

5.3.3.3 Proximity Effect

The proximity effect is also the result of eddy currents. A changing magnetic field induces eddy currents within a conductor. If similar currents are also flowing through one or more nearby conductors, such as within a closely wound coil of wire, the distribution of current within the conductor will be constrained to smaller regions. The resulting current crowding is termed as proximity effect

[Peters, 2004].

Proximity effect in a spiral coil is dependent upon the distance between adjacent metal lines and the operating frequency. The closer the distance, the stronger the proximity effect. Additionally, the higher the operating frequency, the stronger the proximity effect. However, previous research has shown that when operating at frequencies below 1GHz, the proximity effect between the turns of a spiral coil is negligible [Musunuri, 2005]. Since the proposed pressure sensor is designed to operate between 10-20MHz, the proximity effect of the coil metal lines can be ignored.

5.3.4 Characterisation of a Square Spiral Coil

In order to achieve optimal energy transmission efficiency between the sensor and the reader, it is necessary to set up a theoretical model for the square spiral coil. This would also provide a better understanding of the influence of parasitic effects on the sensor performance. In this section, the definitions and calculations of coil's parasitic resistance, parasitic capacitance, self-inductance, and quality factor are introduced.

A spiral coil is characterised by several parameters. The number of turns, metal line width and thickness, spacing between lines and spacing to ground all influence the electrical properties and losses of the coil. Neagu has derived

formulae for the characteristics of a square spiral coil deposited onto a silicon substrate covered with an insulating silicon dioxide (SiO_2) film [Neagu, 1997]. The cross-section of the coil is shown in Figure 5.7.

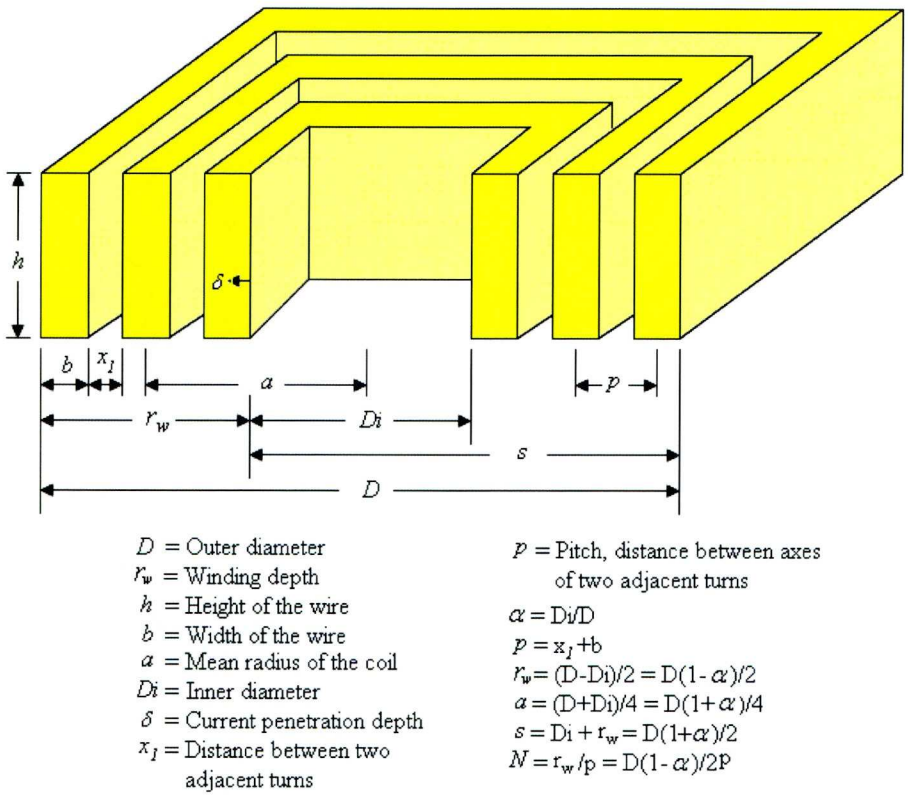

Figure 5.7 Schematic of a square spiral coil [Neagu, 1997].

5.3.4.1 Parasitic Elements

Parasitic elements in an integrated spiral coil include parasitic resistance and parasitic capacitance. Since an inductor is intended for storing magnetic energy, the inevitable resistance and capacitance in a real inductor are undesirable and are therefore considered as parasitic. The parasitic resistances dissipate energy through ohmic loss while the parasitic capacitances store unwanted electric

energy [Yue, 1999].

a. Parasitic Resistance

The parasitic resistance of a spiral coil consists of series resistance and parallel resistance. Series resistance is caused by the electrical resistivity of the coil metal lines, while parallel resistance is due to the finite resistance of the insulating layer on which the coil is placed. The series resistance of a coil can be divided into two parts: frequency independent resistance and frequency dependent resistance. The frequency independent part is the DC resistance of the coil metal lines which can be found by Ohm's Law.

Assume that a is the mean radius of the coil which can be expressed as:

$$a = (D + D_i)/4 = (1+\alpha)D/4 \tag{5.27}$$

where D_i and D are the inner and outer diameters of the coil, respectively, α is the ratio of the inner and outer diameters and $\alpha = D_i / D$, the length of the metal lines is:

$$l = 8Na = 2N(1+\alpha)D \tag{5.28}$$

where N is the number of turns of the coil. If we set the pitch of the coil is denoted as $p = x_1 + b$, where x_1 and b are the distance between two adjacent turns and wire width of the coil, respectively. Then N can be expressed as:

$$N = \frac{(1-\alpha)D + 2x_1}{2p} \approx \frac{(1-\alpha)D}{2p} \tag{5.29}$$

Substituting the above equation into Equation 5.28, the following equation is

obtained:

$$l = \frac{(1-\alpha^2)D^2}{p} \tag{5.30}$$

Therefore, the frequency independent resistance of the coil can be expressed as:

$$R_{DC} = \frac{\rho l}{hb} = \frac{\rho \cdot D^2(1-\alpha^2)}{h \cdot b \cdot p} \tag{5.31}$$

where ρ, h and b are the electrical resistivity, the height and width of the coil metal lines, respectively.

The frequency dependent resistance results from the skin effect and proximity effect which have been introduced in previous sections. When the skin depth is smaller than the half width of the wire and the skin effect cannot be ignored, the DC resistance should be corrected accordingly. Butterworth derived an approximation equation for a spiral coil with $N > 35$ considering these two effects [Butterworth, 1926]:

$$R_{total} = R_{DC}\left(1+\frac{1}{48}\left(\frac{b/2}{\delta}\right)\left(1+u\cdot 12\left(\frac{b/2}{\delta}\right)\right)\right) \tag{5.32}$$

The variable u in the above equation depends on the value of the ratio of the coil's winding depth r_w and the outer diameter D. Table 5.4 gives the values of u in different coil configurations.

The parallel resistance of an integrated coil is determined by the resistance of the substrate on which the coil is placed. Considering the integrated coil is placed on a substrate with an insulating layer which has a thickness of x_2 and electrical

resistivity of ρ_{in} as shown in Figure 5.8, then its parallel resistance R_p can be expressed as [Neagu, 1997]:

$$R_p = \frac{\rho_{in} \cdot x_2}{b \cdot l} \tag{5. 33}$$

Table 5.4 Correction parameter u [Butterworth, 1926]

$\frac{r_w}{D}$	u	$\frac{r_w}{D}$	u
0.000	3.290	0.250	4.749
0.025	3.315	0.275	5.041
0.050	3.373	0.300	5.364
0.075	3.459	0.325	5.718
0.100	3.567	0.350	6.104
0.125	3.702	0.375	6.523
0.150	3.859	0.400	6.968
0.175	4.042	0.425	7.436
0.200	4.251	0.450	7.911
0.225	4.486	0.475	8.638
0.250	4.749	0.500	8.638

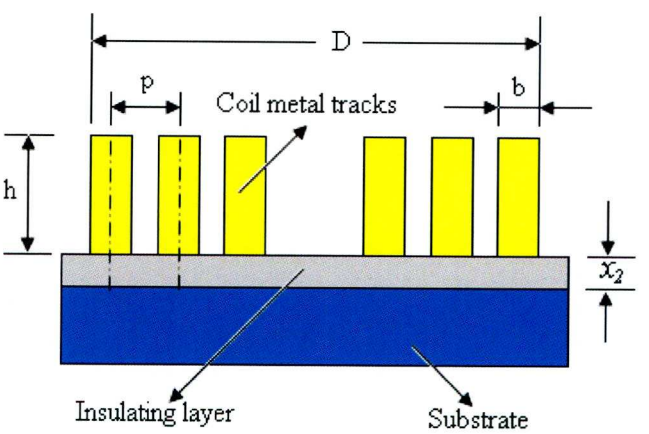

Figure 5.8 Parallel resistance of an integrated coil [Neagu, 1997].

Substituting Equation 5.28 into the above equation:

$$R_p = \frac{\rho_{in} \cdot x_2}{b} \cdot \frac{p}{D^2(1-\alpha^2)} \tag{5.34}$$

The parallel resistance can be ignored in most practical situations as it is much greater than the series resistance.

b. Parasitic Capacitances

The parasitic capacitances of the square spiral coil consist of three parts: (1) the capacitance between the segments of the coil, C_{ss}, (2) the capacitance between the coil and its substrate, C_{cs}, and (3) the capacitance between the coil's contact pads and substrate, C_{ps}. Figure 5.9 shows these parasitic capacitances and their electrical equivalent circuit [Neagu, 1998].

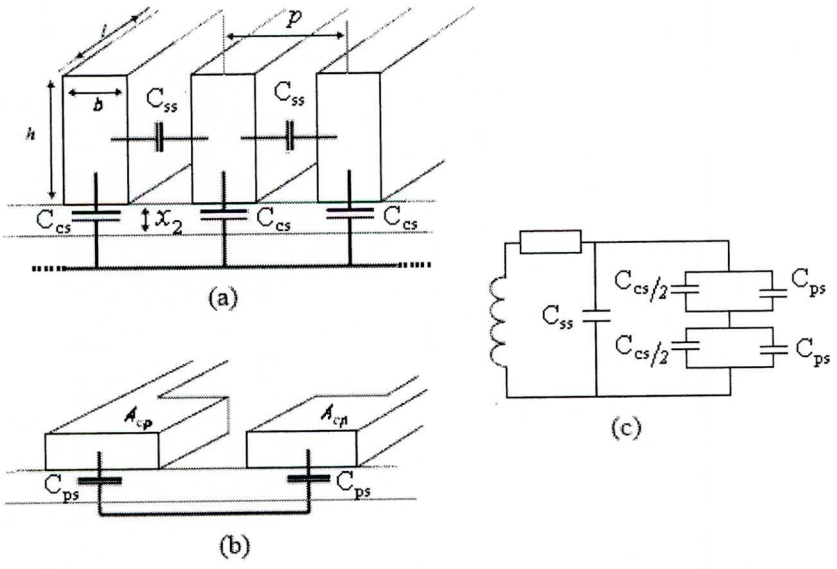

Figure 5.9 Parasitic capacitances of a spiral coil between (a) coil's segments C_{ss}, coil and substrate C_{cs}; (b) contact pads and substrate C_{ps}; (c) electrical equivalent of parasitic capacitances [Neagu, 1998].

These parasitic capacitances can be calculated from the following equations:

$$C_{ss} = \frac{2\varepsilon_1 \cdot hD}{p-b}\left(1+\alpha-\frac{4p}{D(1-\alpha)}\right) \tag{5.35}$$

$$C_{cs} = \frac{\varepsilon_2 \cdot bD^2}{x_2 p}(1-\alpha^2) \tag{5.36}$$

$$C_{ps} = \frac{\varepsilon_2 \cdot A_{cp}}{x_2} \tag{5.37}$$

where ε_1 is the permittivity of the material between the coil segments, ε_2 is the permittivity of the insulating material, and A_{cp} is the area of contact pads. The total parasitic capacitance C_{tp} can be determined from the equivalent circuit shown in Figure 5.9(c) and is given by:

$$C_{tp} = C_{ss} + \frac{1}{4}C_{cs} + \frac{1}{2}C_{ps} \tag{5.38}$$

5.3.4.2 Self-Inductance

The self-inductance of coils of various shapes and structures can be calculated by using different techniques. Some of them are readily available from references [Maxwell, 1954; Terman, 1943; Grover, 1946; Welsby, 1960; Greenhouse, 1974]. In the following sections, three techniques are briefly introduced including approximate forms, Greenhouse approach and finite element method. These approaches will be used to calculate the self-inductance of the proposed square spiral coil shown in Figure 5.13.

a. Approximation Forms

Approximation forms are widely used in calculating the inductance of coils with

different shapes such as circular, rectangular, multiple-layer, and solenoid coils. For a square spiral coil operating at low-frequencies, the approximate equation of its self-inductance can be expressed as [Neagu, 1997]:

$$L = \frac{\mu \cdot D^3}{4\pi \cdot p^2} \cdot (1-\alpha^2)(1-\alpha) \cdot \left[\ln \frac{(1+\alpha)}{(1-\alpha)} + 0.2235 \cdot \frac{(1-\alpha)}{(1+\alpha)} + 0.726 \right] \qquad (5.39)$$

where μ is the relative permeability of air, ($\mu = 4\pi \cdot 10^{-7}$ H/m). It can be seen from this equation that at low frequencies, the inductance of a spiral coil does not change with metal line thickness.

b. Greenhouse Method

Greenhouse introduced a simple method for estimating the inductance of rectangular spiral coils. The Greenhouse's method states that the overall inductance of a planar coil can be derived by calculating inductance of each straight segment and the mutual inductance between these segments [Greenhouse, 1974].

A schematic explanation of Greenhouse model is shown in Figure 5.10 with arrow direction corresponding to the direction of the current flow in each segment of a two-turn planar coil. The total self-inductance of these straight segments L_o can be expressed as:

$$L_0 = Ls_1 + Ls_2 + Ls_3 + Ls_4 + Ls_5 + Ls_6 + Ls_7 + Ls_8 \qquad (5.40)$$

where $Ls_1 \ldots Ls_8$ are the self-inductance of each straight segment.

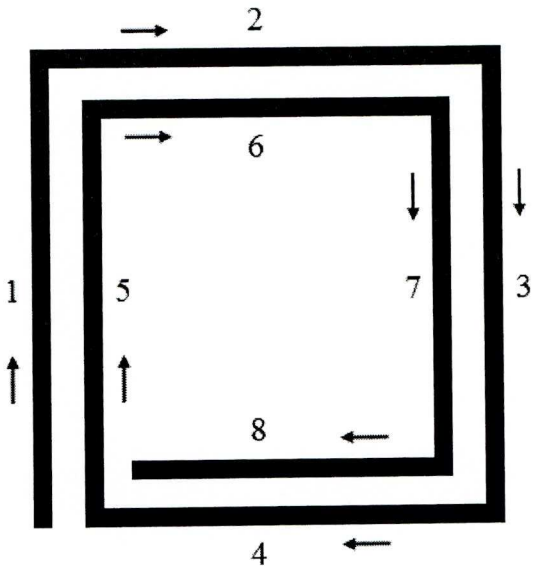

Figure 5.10 A schematic explanation of Greenhouse's model [Greenhouse, 1974].

For a straight conductor with length l, width b and thickness h, its self-inductance L_s is given by:

$$L_s = 0.002l \cdot \left[\ln\left(\frac{2l}{b+h}\right) + 0.50049 + \frac{b+h}{3l} \right] \tag{5.41}$$

The total mutual inductance of these segments M is the sum of the mutual inductance between two straight segments:

$$M = Ms_1s_2 + Ms_1s_3 + \ldots + Ms_1s_8 + \ldots + Ms_8s_1 + Ms_8s_2 + \ldots Ms_8s_7 \tag{5.42}$$

where $Ms_1s_2, Ms_1s_3, \ldots Ms_8s_7$ are the mutual inductance between two straight segments.

The mutual inductance between two segments of a coil depends on their angle of intersection, length and separation. It is positive when the directions of current on

these segments are in the same direction, and negative when the directions of currents are opposite directions. For example, in Figure 5.10 the mutual inductance between Segment 1 and Segment 5 is positive, while it is negative between Segment 1 and Segment 3. Two segments orthogonal to each other have no mutual inductance since the magnetic flux is not linked together. The mutual inductance between two conductor segments with equal length of l is given by:

$$M = 2lF \tag{5.43}$$

where F is the mutual inductance parameter which is expressed as:

$$F = \ln\left\{\left(\frac{l}{d}\right)+\left[1+\left(\frac{l}{d}\right)^2\right]^{1/2}\right\}-\left[1+\left(\frac{d}{l}\right)^2\right]^{1/2}+\frac{d}{l} \tag{5.44}$$

The total self-inductance of the coil can be calculated from the following equation:

$$L = L_o + M \tag{5.45}$$

c. Finite Element Method

The approximation and Greenhouse methods have shown their advantages in estimating the inductances of relatively simple coil shapes and structures. However, for complicated coils, for example, coil formed with varied cross-section wires, or multi-layer coils, it is difficult to accurately estimate their inductances by using these techniques. In such cases, the most appropriate solution is to use the finite element method.

The first step of any finite element simulation is to discretize the actual geometry of a structure using a collection of finite elements. Each finite element represents a discrete portion of the physical structure. The finite elements are joined by shared nodes. The simulation results are based on these nodes and elements.

Many commercial or open-source software packages are available to simulate integrated coils such as FastHenry [Fastmodel, 2007], ASITIC [Meyer, 2000], Sonnet Lite [Sonnet, 2007] and CoventorWare. These software packages employ different algorithms to calculate the coil inductance, resistance, capacitance or self-resonance by solving Maxwell's equations, which govern the relationship between the electric fields and magnetic fields. Each software package has its advantages and limitations. For example, FastHenry reduces the computing time significantly compared to other packages. However, it can only model eddy currents and proximity effect but not high frequency capacitive loss or self-resonance. In addition, the fabrication process of an integrated coil cannot be specified in FastHenry which has influence on the coil substrate losses. ASITIC can specify coil fabrication process and the effects of nearby conductive or dielectric materials on the losses and quality factor, but it is time consuming for simulating coils with large numbers of turns and small track widths [Peters, 2004]. Simulation module MemHenry is employed in CoventorWare to solve integrated coils. It can rapidly complete the extraction of frequency-dependent resistance and inductance for micro-coils with complicated 3-D structures. The

main feature of MemHenry is that it can perform parametric study analysis which allows the designer to be able to analyse inductance dependence on position, dimension, or mechanical deformation. The major disadvantage is that the information of capacitive loss and self resonance of integrated coils are not available.

5.3.4.3 Quality-Factor of the Sensor

The coil in the sensor has two functions. It serves as a means of acquiring power via inductive coupling as well as a means of transmitting the measured data to outside detection system. In the medical environment, the sensor is required to achieve a sufficient communication distance between the sensor and the reader. This distance is affected by a number of factors. The quality factor of the sensor plays a key role in ensuring a maximal operating distance. Equation 5.25 defines the quality factor of a coil. For an *LC* resonant circuit, the coil is connected with a tuning capacitor. Figure 5.11 shows the equivalent circuit of an *LC* resonant sensor, where *L, R, C_{tp}* are the self-inductance, parasitic resistance and parasitic capacitance of the coil, respectively, and C_{tune} is the capacitance of the connected capacitor. In this situation, the Q-factor of the sensor needs to be calculated.

From Equation 2.1, the resonant frequency of the sensor is:

$$\omega_s^{\,0} = \frac{1}{\sqrt{L(C_{tp} + C_{tune})}} \tag{5.46}$$

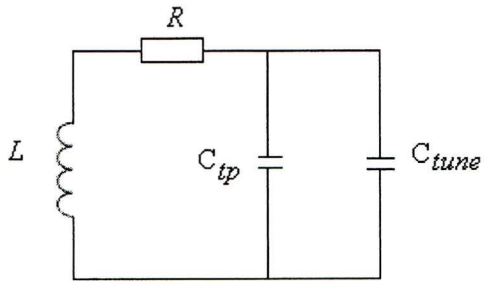

Figure 5.11 Equivalent circuit of an *LC* resonant sensor.

This equation implies that when a coil is connected in series with a capacitor to form an *LC* circuit, the resonant frequency of this circuit is lower than the intrinsic resonant frequency of this coil. Substituting the above equation into Equation 5.25 the following equation is obtained:

$$Q_s = \frac{L}{R\sqrt{L(C_{tp}+C_{tune})}} = \frac{1}{R}\sqrt{\frac{L}{(C_{tp}+C_{tune})}} \tag{5.47}$$

In practice, the parasitic capacitance of the coil should be kept as low as possible so as to minimise the energy dissipation. This can be achieved by constructing the coil on a thick insulating layer. Another benefit is the sensitivity of the sensor will be improved when the parasitic capacitance is kept low as the sensor's resonant frequency will mainly depend on the tuning capacitor.

When the parasitic capacitance of the coil is much smaller than that of the tuning capacitor, Equation 5.47 can be simplified as:

$$Q_s = \frac{\omega_s^{\,0} L}{R} \approx \frac{1}{R}\sqrt{\frac{L}{C_{tune}}} \tag{5.48}$$

The above equation can be used to optimise the design of the square spiral coil.

In order to get a high quality factor, i.e., high energy transmission efficiency, the series resistance of the coil should be made as small as possible so that the dissipation of energy at resonance is minimised. In addition, its inductance should be designed to be as large as possible in order to store sufficient energy. The increase of inductance can be achieved by increasing the number of turns of the coil. However, increasing the number of turns also increases the coil's series resistance. Therefore, tradeoffs must be made between these two parameters. Another constraint of increasing the inductance is the available technology for fabricating the coil in a limited space with a large number of turns.

The next step is to define the ratio of the inner and outer diameters of the coil in order to obtain a maximum quality factor. Substitute Equations 5.31 and 5.39 into Equation 5.48, the following equation for Q is obtained:

$$Q = \frac{\omega_0 \cdot \mu Dhb(1-\alpha)}{4\pi\rho p}\left[\ln\frac{(1+\alpha)}{(1-\alpha)} + 0.2235\frac{(1-\alpha)}{(1+\alpha)} + 0.726\right] \qquad (5.49)$$

Equation 5.49 gives a useful guide for designing high quality factor square spiral coils because the ratio α can be optimised to achieve a maximum Q value. Assuming a square planar coil has an outer diameter of 5030μm, line width and thickness of 30μm, line space of 10μm, at resonant frequency 20MHz the relationship between its quality factor Q and the ratio of its inner and outer diameters α can be found in Figure 5.12. It can be seen clearly that a maximum value of Q is reached at $\alpha \approx 0.256$.

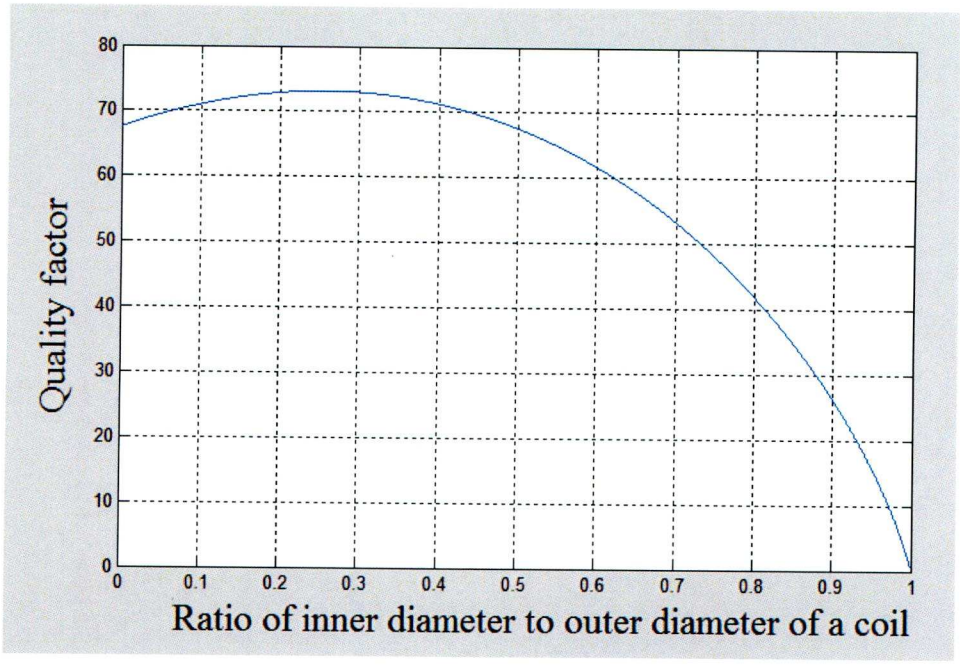

Figure 5.12 The relationship between the quality factor and the ratio of the inner and outer diameters of a planar square coil.

5.3.5 Coil Configuration

Based on the above considerations and design principles, two square spiral coils were designed for the inductive component of the proposed sensor. The dimensions of these two coils are shown in Figure 5.13. Both coils have 46 turns and the outer and inner diameters (as the coil is spiral, the term 'diameter' is used rather than 'lateral length' for describing its geometry) are 1370μm and 5030μm, respectively. Copper was chosen for the coils' metal lines (reason will be explained in Section 5.5.3). It has an electrical resistivity of 1.78×10^{-8} Ω.m. The metal lines in Coil 1 are 30μm thick and wide, with 10μm gap between two adjacent lines. Coil 2 has the same configuration as Coil 1 except that its line thickness is 100μm. The ratio of the inner and outer diameters of the coils,

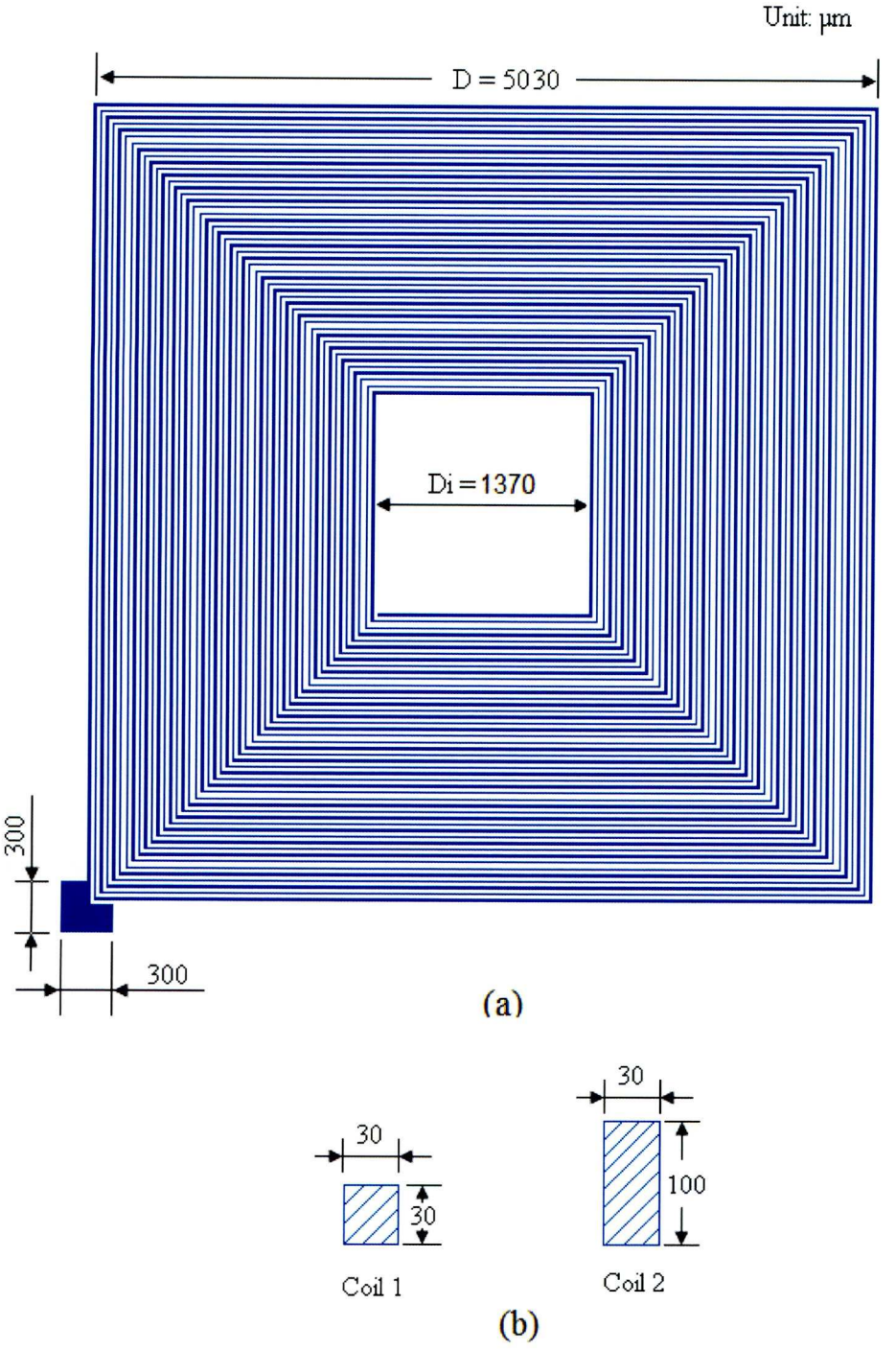

Figure 5.13 Dimensions of the square spiral coils. (a) layout of the coil tracks and the contact pad; (b) the cross sections of the coil tracks for both coils.

α, was chosen as 0.272 rather than 0.256, which is the optimised dimension for a square spiral coil for achieving an optimum quality factor. This is because that in order to achieve α=0.256, extra turns of the coil would be required. This,

however, would have an impact on the size of the electrodes of the capacitor component. As the capacitance of a parallel plate capacitor is determined by the area of overlap of its electrodes and the distance between the electrodes, a smaller electrode size will result in a small capacitance value if the distance between the two electrodes is decided. The value of 0.272 was then considered to be acceptable as it affects very little on the quality factor of the coil (see Figure 5.12) and the proposed pressure sensor can be operated within the preselected resonant frequency range (10-20MPa). More details of the capacitor will be revealed in Section 5.6.

Approaches and equations presented in Section 5.3.4 were used to calculate the self-inductances of these two coils. These results are shown as follows:

5.3.5.1 Coil Resistance

The frequency independent resistances of these two coils were derived from Equation 5.31 and the results are 11.58Ω and 3.48 Ω for Coil 1 and Coil 2, respectively. The frequency dependent resistance of the Coil 1 was ignored as the metal lines are only slightly thicker than the skin depth of copper (14.66μm) at 20MHz which was calculated in Section 5.3.3.2. The frequency dependent resistance of Coil 2 was derived from the simulation result as showing in Fig. 5.14. Its resistance at 20MHz is about 9.41 Ω.

CoventorWare was also used to simulate the coils' resistances for operation frequencies in the range from 100kHz to 10GHz and the results are shown in Figure 5.14. It can be seen that the resistances of the two coils do not change much from 100kHz to 10MHz. This means that the series resistance of a coil is mainly contributed by its DC resistance at low operation frequencies. However, the resistances increase slightly from 10MHz to 100MHz, which indicates that

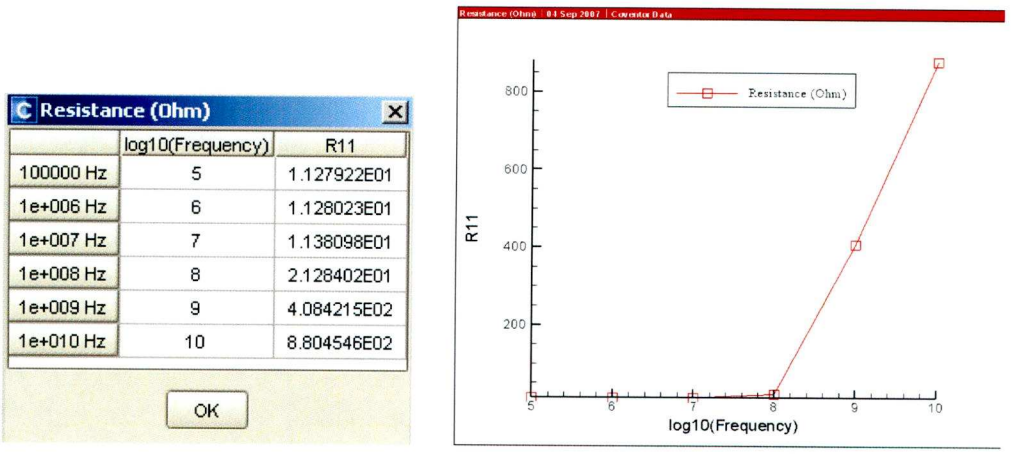

a

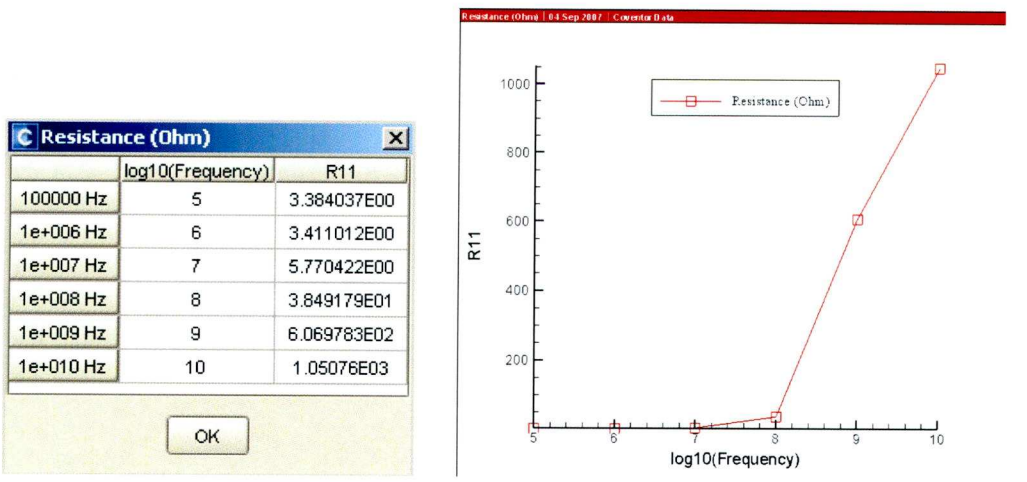

b

Figure 5.14 Resistance simulation results from CoventorWare for (a) Coil 1; (b) Coil 2 for operating frequencies from 100kHz to 10GHz.

the skin effect and proximity effect start to contribute to ohmic losses. When the operation frequency is over 100MHz, the resistance increases dramatically as it then becomes dominated by the skin and proximity effects.

Comparing coil resistances computed by simulation to those calculated from Equation 5.31, it can be seen that there is a close match at low operation frequencies. This indicates that the simulation result is reliable. It is also notable that the rate of increase in resistance of Coil 2 is higher than that of Coil 1, especially at high frequencies. This is attributed to the proximity effect. At high operation frequency, the proximity effect generates induced current densities in each copper turn. Therefore, the ohmic losses integrated over the cross-sectional area of each turn are larger for thicker coils.

5.3.5.2 Self-inductance

The self-inductance of the two coils was derived from the approaches discussed in Section 5.3.4.2. The inductance for both of the coils calculated using Equation 5.39 was 7.57μH. When using Greenhouse method, the value was 7.55μH. It is clear that these results agree quite well. A Matlab™ (from Mathworks Inc.) computing programme was written to calculate the inductance of these coils and is shown in Appendix A.

The simulation results from Conventorware are shown in Figure 5.15. It shows

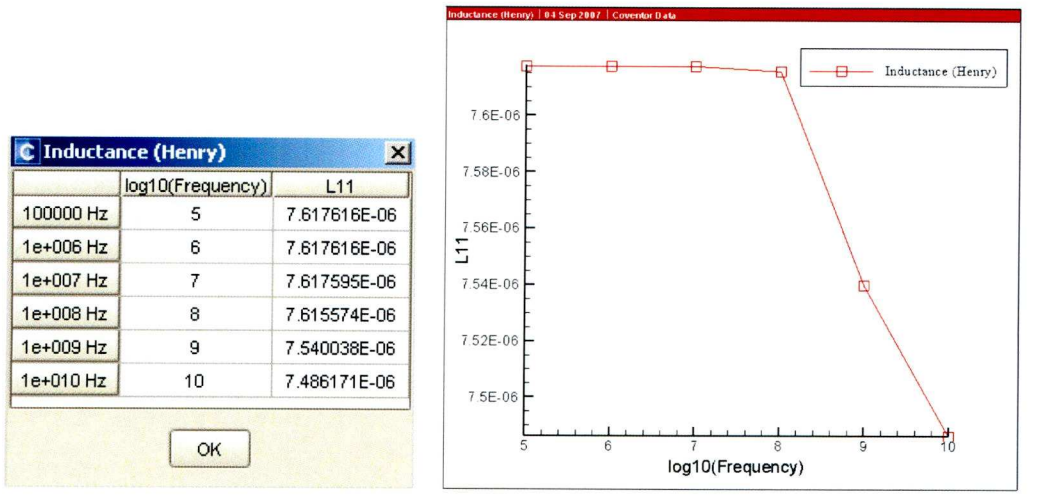

a

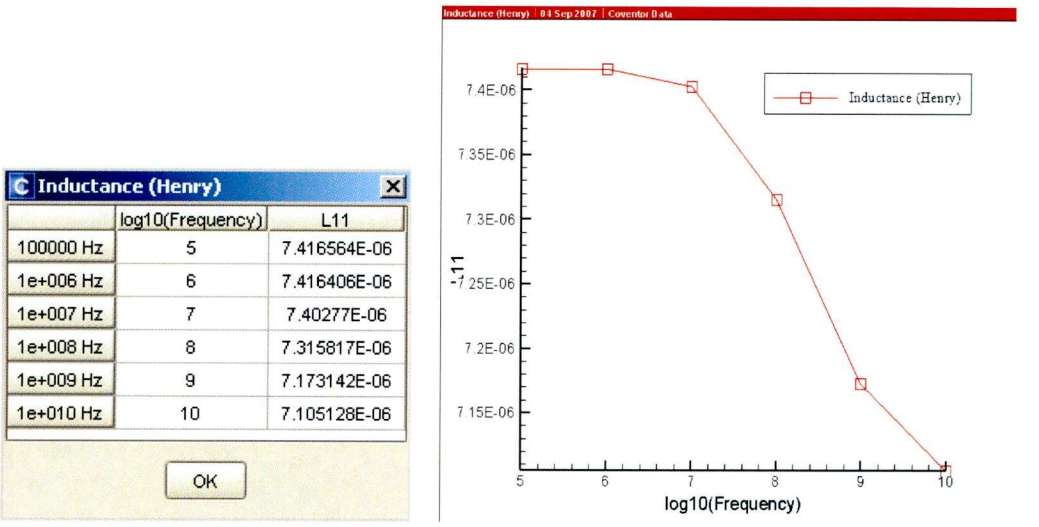

b

Figure 5.15 Self-inductance simulation results from CoventorWare for (a) Coil 1; (b) Coil 2 at operating frequencies from 100 kHz to 10GHz.

that inductance is not affected much by the operation frequency. The difference in inductance in the range of frequencies 100kHz-10GHz for Coil 1 was less than 2 per cent and about 4 per cent for Coil 2. This contrasts with the coil resistances which show 2-orders of magnitude difference over the same frequency range.

It can also be seen that these results derived from different methods show a high degree of agreement. In this design, the inductance results of the two coils were adopted from the finite element method. However, the real self-inductance of an integrated coil may differ from the calculated result because of distributed capacitance. For this reason, inductance calculations are generally used only as a starting point in the final design.

The parameters of the two spiral square coils and calculated results are shown in Table 5.5.

Table 5.5 Coils' parameters and calculated results

	Parameters and results	**Coil 1**	**Coil 2**
1	Number of turns (*N*)	46	46
2	Inner diameter D*in* (μm)	1370	1370
3	Outer diameter *D* (μm)	5030	5030
4	Width of metal lines *b* (μm)	30	30
5	Height of metal lines *h* (μm)	30	100
6	Line space x_1 (μm)	10	10
7	Series resistance R_{total} at 20MHz (Ω)	11.58	3.48
8	Inductance *L* at 20MHz (μH)	7.62	7.40

5.4 Proposed Sensor Structures

Two sensor structures were designed in this research as it was the aim to compare the effect of substrate losses on the sensor overall performance, as well

as exploring the use of different advanced micro-fabrication techniques for developing high quality factor integrated coils. Figure 5.16 and Figure 5.17 show these two proposed sensor structures. In order to make the view more clearly, the 46-turn coils are replaced with two 3-turn coils in these figures.

5.4.1 Sensor 1

As shown in Figure 5.16, Sensor 1 consists of a square spiral coil and a pressure sensitive diaphragm. The coil is embedded in a silicon substrate. It has 46 turns and is made of copper. Both the width and thickness of its metal lines are 30μm. The distance between two adjacent lines is 10μm. A square copper layer is located in the central part of the silicon substrate. It is connected to the coil and acts as the lower electrode of the capacitive component of the *LC* sensor. The diaphragm is of a 'bossed' type which has a thick and rigid part in the middle. It functions as a pressure sensing element as well as the upper electrode of the capacitor. The use of bossed diaphragm is intended to increase the linearity of the capacitance of the capacitor. The dimension of this bossed diaphragm can be found in Figure 5.22.

The coil is deposited on the silicon substrate using electroplating technique. Moulds for the electroplating are fabricated by etching trenches into silicon substrate using deep reactive ion etching (DRIE) technology. The diaphragm is made of silicon and is fabricated by a wet anisotropic etching process. Its back

side is doped with boron (B) through ion implantation to make it electrically conductive. Silicon fusion bonding technique is used to attach the diaphragm to the coil. The fabrication process of the coil and the diaphragm will be presented in Chapter 6.

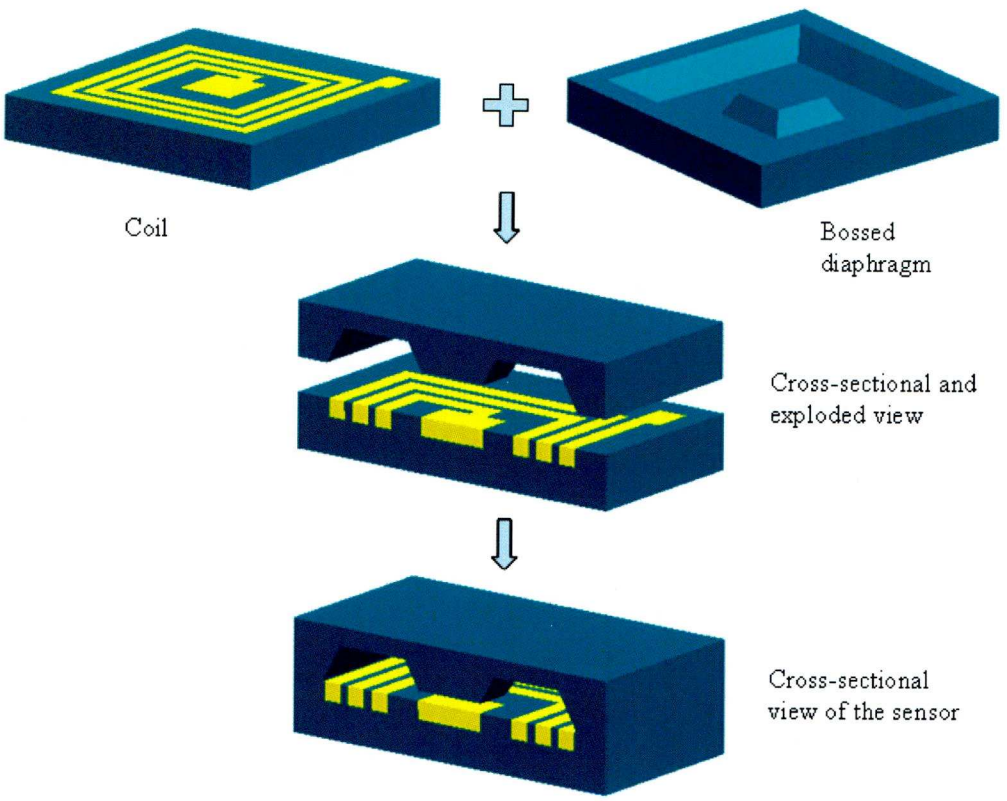

Figure 5.16 Proposed structure of Sensor 1.

5.4.2 Sensor 2

Sensor 2 has the similar structures as Sensor 1. However, its coil is built on a glass substrate as shown in Figure 5.17. The thickness of the coil metal lines is 100μm. Thick-film photo-resist is used to form the electroplating mould for the deposition of the copper layer. In contrast to the bossed diaphragm in Sensor 1,

the silicon diaphragm in Sensor 2 is of a uniform flat type (see Figure 5.22). Anodic bonding technique is used to join these two parts together.

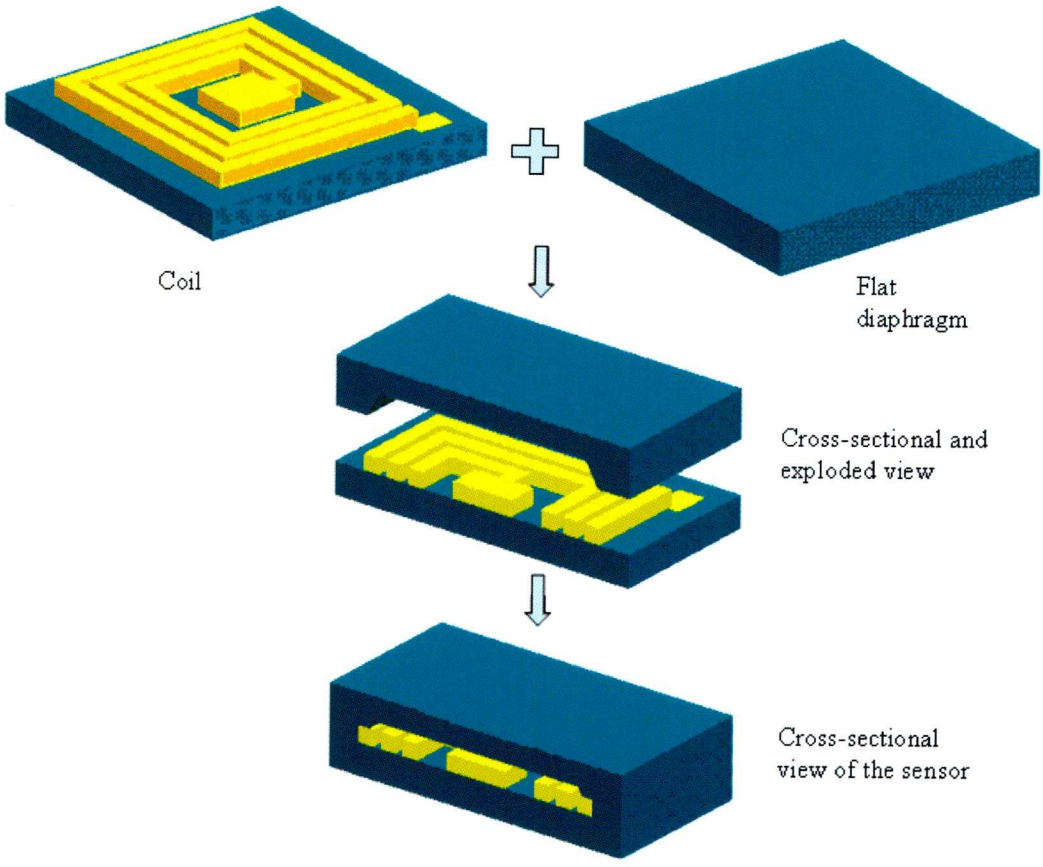

Figure 5.17 Proposed structure of Sensor 2.

5.5 Considerations for Selecting Sensor Structural Material

Several issues need to be taken into account when choosing the structural material for the sensor. The first is the material long-term stability in harsh environment. As the sensor will be implanted in the body over a long period, the sensor has to be unaffected by this corrosive saline environment and should function accurately over the lifetime of the patient. The second is the material compatibility with current micro-fabrication techniques. As the sensor is to be developed by employing MEMS technology, the fabrication and packaging

techniques for this material have to be well established. Another concern is the material biocompatibility. If the external surface of the sensor is not biocompatible, then it has to be coated or encapsulated with biocompatible material.

In Chapter 2, it was mentioned that the current fabrication technologies used in MEMS were derived from those of microelectronics. As a result, many MEMS products use microelectronics materials such as silicon and gallium arsenide for the sensing or actuating elements. However, in recent years, many other materials have been used in MEMS products such as quartz, glass, plastics, polymers, and ceramics etc. The fabrication processes of using these materials for different applications are well developed and documented. Therefore, one of the objectives was to explore the use of highly electrical insulating materials as the coil's substrate in order to minimise its resistive and capacitive losses.

5.5.1 Substrate Material for Sensor 1

In Sensor 1, silicon was chosen for both the coil substrate material and the pressure sensing material. Silicon is the most widely used substrate material for MEMS products. It has excellent mechanical properties with Young's modulus as high as 197GPa. Silicon is a highly stable single crystal material and shows nearly no ageing. Insulating or protecting material such as silicon dioxide (SiO_2) and silicon nitride (Si_3N_4) can be easily deposited on silicon. All these features

make silicon an ideal material for long-term medical implantation purposes. By making the same material for the entire sensor structure, the problem of creep caused by different coefficient of thermal expansion can be eliminated.

5.5.2 Substrate Material for Sensor 2

Borosilicate glass Pyrex^{TM} 7740 was chosen for the glass substrate in Sensor 2. Pyrex glass is electrically insulating. The substrate losses due to low material resistivity are avoided, and therefore, integrated coils with high quality factor values can be realised. This material is resistant to many chemicals and can endure exposure to harsh environment. Pyrex glass can be joined to many different metals and is compatible with MEMS fabrication processes [Hülsenberg, 1994]. It contains easily movable positive sodium ions to perform anodic wafer bonding. The thermal expansion coefficient of Pyrex glass (α=3.3 at 20°C) matches well with that of silicon (α=3 at 20°C) [Kim et al., 2006], so thermal stress in the sensor structure can be minimised.

5.5.3 Coil Material

The selection of coil material must consider the electrical resistivity of the material and its compatibility with current MEMS thin-film deposition processes. A low material resistivity is the primary concern in realising high quality-factor micro-coils. There are several techniques available for depositing metal film on silicon or glass substrate, including electroplating, epitaxy, chemical vapour

deposition (CVD), evaporation, and sputtering. However, the thickness of the coil metal lines is over 30μm which is too thick for some of the above techniques. Therefore, electroplating is the appropriate technique for depositing the coil material.

Although many metals or metal alloys can be electroplated on silicon or glass substrate, the most commonly used materials for integrated coil structures are gold and copper. This is because they have low electrical resisitivities with excellent adhesion to silicon. Another merit of using gold for micro-coil structural material is its high chemical resistance when the coil is exposed to corrosive environment. Table 5.6 shows the electrical resisitvity of seven metals which are compatible with electroplating process [Serway, 1998]. Among them, silver has the lowest resistivity, but its electroplating process on silicon has not been well established and documented.

Table 5.6 Electrical properties some metals at 20°C [Serway, 1998]

Material	**Resistivity** ($\times 10^{-8}$ Ωm)	**Conductivity** ($\times 10^{7}$ /Ωm)
Silver	1.65	6.06
Copper	1.78	5.62
Gold	2.42	4.13
Aluminium	3.21	0.31
Tungsten	5.4	0.19
Nickel	6.9	0.11
Chromium	13.2	0.08

5.6 Capacitor Design

The capacitor in this design is of the variable parallel plate type which consists of a fixed electrode and a movable electrode. Its capacitance should satisfy the requirement of the designated resonant frequency of the proposed sensor. This capacitance should be also relatively large as it is desirable to have the sensor's resonant frequency dominated by variable capacitor rather than the parasitic capacitance of the coil. For a parallel plate capacitor, large capacitance can be achieved by keeping the distance between the two electrodes as small as possible. Another benefit of this arrangement is the improved sensitivity of the sensor to pressure changes. In this section, the size of these two electrodes and the gap between them as well as the dimensions of the diaphragm used for pressure sensing will be determined.

5.6.1 Electrodes and Gap

In Section 5.2, the system operating frequency at zero-pressure has been chosen to be 20MHz. The inductance for Coil 1 and Coil 2 was found through simulation to be 7.62μH and 7.40μH, respectively. Therefore, the required capacitance of the tuning capacitor for each sensor can be calculated from Equation 2.1 and this gives 8.32pF for Sensor 1 and 8.56pF for Sensor2. For a parallel plate capacitor, the capacitance is determined by the area of overlap of the electrodes A and the distance d between the two electrodes according to the expression below:

$$C = \frac{\varepsilon \cdot \varepsilon_0 A}{d} \tag{5.50}$$

where $\varepsilon_0 = 8.8542 \times 10^{-12} F \cdot m^{-1}$ is the permittivity of free space and ε is the relative permittivity. For air, ε=1.

As shown in Figures 5.16 and 5.17, both of the fixed electrodes are located inside the square spiral coils. The maximum available construction area for each electrode is 1370×1370μm. Allowing the necessary gap between the electrode and the coil turns, the actual size of the these two fixed electrode was chosen to be 1320×1320μm. Figure 5.18 shows the layout of the lower part of the pressure sensor which includes the fixed electrode, coil, contact pad, and silicon substrate.

The sizes of the movable electrodes of the two sensors were designed to be slightly bigger than the fixed electrodes (1330×1330μm). This is to account for the tolerance of wafer bonding. Given the above area of overlap, the required gap between the electrodes for Sensor 1 and Sensor 2 determined from Equation 5.50 is 1.83μm and 1.80μm, respectively. However, in the final design, the gap was chosen as 2μm for both sensors.

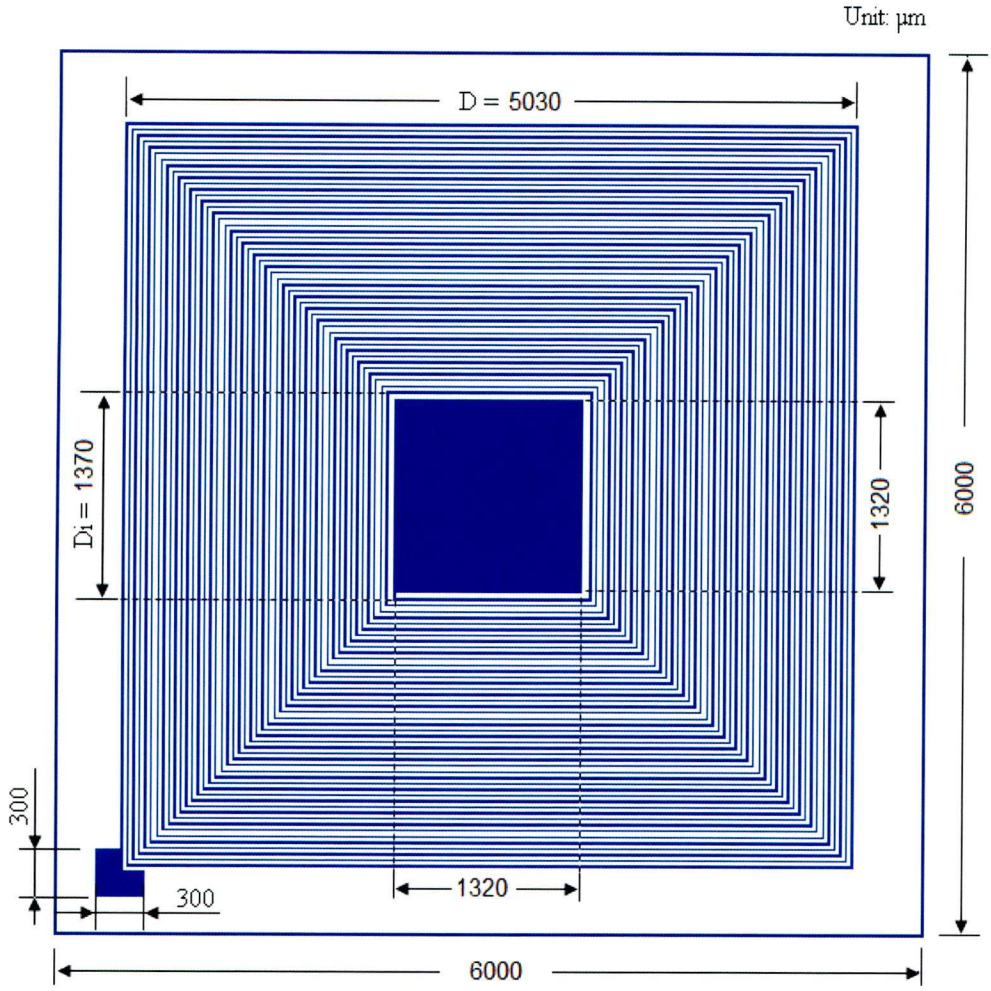

Figure 5.18 Layout and dimensions of the lower part of Sensor 1 and Sensor 2.

5.6.2 Diaphragm

5.6.2.1 Diaphragm Types

The movable electrode is a pressure sensitive diaphragm which can cause the capacitor to change its capacitance in response to pressure changes. Diaphragms are used as sensing elements both in traditional and MEMS-based pressure sensors. In general, three types of diaphragms are frequently used in pressure sensing. These include the flat diaphragm, the bossed diaphragm and the corrugated diaphragm. Figure 5.19 shows the cross-sections of these three types

of diaphragms.

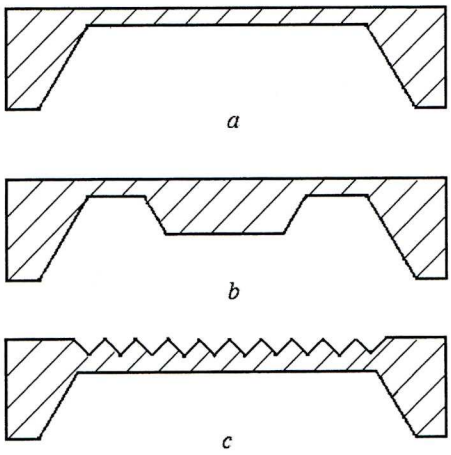

Figure 5.19 Cross-section of a (a) flat diaphragm;
(b) bossed diaphragm (c) corrugated diaphragm.

Flat diaphragms are the most commonly used sensing elements in pressure sensors because of its simplicity. It is a popular choice for MEMS-based pressure sensors due to the planar nature of MEMS fabrication processes. The main drawbacks of this type are the relatively small displacement and non-linearity.

A bossed diaphragm is also a flat diaphragm but with a thicker centre portion. The reason of making a boss in a diaphragm is to increase the rigidity in the centre so as to get higher stresses for a given deflection compared with flat diaphragms. This is particularly useful when strain gauges are mounted on the diaphragms for electrical signal transduction [Park, 2002]. Other advantages include improved linearity and sensitivity, which is suitable for sensing low pressures.

Corrugations can increase the sensitivity and linearity of a diaphragm especially when the diaphragm is subjected to large displacements. As flat diaphragms frequently have built-in stresses, the corrugated structure is an effective way to release these stresses. Therefore, the mechanical sensitivity of the diaphragm can be significantly improved. Employing corrugated diaphragms for different applications has been reported in a number of researches. Wang et al. developed a deeply corrugated silicon diaphragm for a condenser microphone [Wang, 2003]. Neagu suggested a corrugated silicon nitride membrane for a medical micro-actuator [Neagu, 1996]. Different types of corrugations can be etched into diaphragms such as triangular, rectangular, trapezoidal, etc. The behaviour of such a diaphragm is affected by the corrugation depth, wavelength, and the thickness and material property of the diaphragm.

In this research, only the performance of flat diaphragm and bossed diaphragm was studied. This is because the main interest was to compare the influence of the deflection of different diaphragms to the capacitance, and in turn, to the resonant frequency of the sensor.

5.6.2.2 Theory of Diaphragms

Before establishing analytical models for the flat and bossed diaphragms, the following assumptions need to be made:

- The materials of the diaphragms are homogenous and isotropic

- The edges of the diaphragms are clamped and can be modelled by built-in boundary conditions;
- The residual stress is neglected;
- The applied pressure is uniform and is normal to the plane of the diaphragm;
- The deflection of the diaphragm is smaller than its thickness;
- The elastic limit of the material is not exceeded.

a. Deflection of the Square Flat Diaphragm

Figure 5.20 shows the cross-section of a square flat diaphragm:

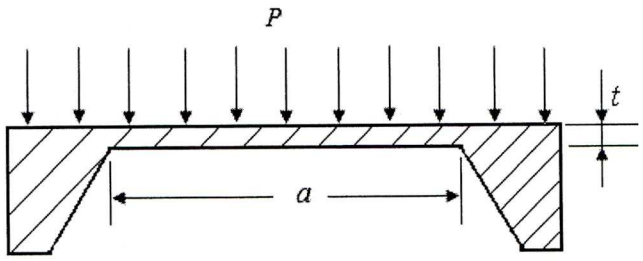

Figure 5.20 Cross-section of a square flat diaphragm.

Based on the theory of flat plate with small deflection, the deflection of any point on a rectangular diaphragm under uniform pressure could be calculated by solving the following partial differential equation [Bin, 1987]:

$$\nabla^4 d(x,y) = \frac{P}{A_s} \tag{5.51}$$

$$A_s = \frac{E \cdot t^3}{12(1-\nu^2)} \tag{5.52}$$

$$\nabla^4 = \frac{\partial^4}{\partial x^4} + \frac{\partial^4}{\partial x^2 + \partial y^2} + \frac{\partial^4}{\partial y^4} \tag{5.53}$$

where P is the applied pressure, A_s is the bending stiffness of the diaphragm, E and ν are the Young's modulus and Poisson's ratio of the diaphragm material, respectively, and t denotes the thickness of diaphragm. For a square diaphragm with side length of a under uniform pressure P, the maximum deflection w_c occurs at the centre of the diaphragm and can be calculated by the following equation [Beeby, 2004]:

$$w_c = \frac{0.0138Pa^4}{Et^3} \tag{5.54}$$

The deflection of the diaphragm at coordinate (x, y) is governed by [Beeby, 2004]:

$$w(x,y) = w_c\left(1 + 0.401\frac{x^2+y^2}{a^2} + 1.161\frac{x^2y^2}{a^4}\right)\cos\left(\frac{\pi \cdot x}{2a}\right)\cos\left(\frac{\pi \cdot y}{2a}\right) \tag{5.55}$$

From the above equation and Equation 5.50 the capacitance of a parallel plate capacitor can be obtained by the surface integration over the diaphragm:

$$C = \int_x \int_y \frac{\varepsilon_0 \varepsilon}{d - w(x,y)} d_x d_y \tag{5.56}$$

where d is the gap between the two electrodes of the capacitor at zero pressure. By substituting Equation 5.55 into the above equation, the following equation is obtained:

$$C = \int_x \int_y \frac{\varepsilon_0 \varepsilon}{d - w_c\left(1 + 0.401\frac{x^2+y^2}{a^2} + 1.161\frac{x^2y^2}{a^4}\right)\cos\left(\frac{\pi \cdot x}{2a}\right)\cos\left(\frac{\pi \cdot y}{2a}\right)} d_x d_y \tag{5.57}$$

b. Deflection of the Square Bossed Diaphragm

The cross-section of a bossed diaphragm is shown as follows [Beeby, 2004]:

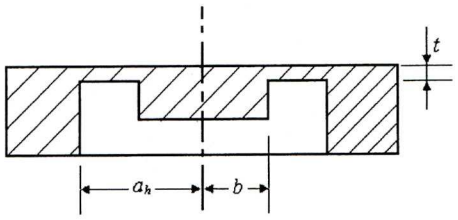

Figure 5.21 A flat diaphragm with a central boss [Beeby, 2004].

The deflection in the centre of the bossed diaphragm under pressure P can be expressed as [Beeby, 2004]:

$$w_c = A_p\left(\frac{Pa_h^{\,4}}{Et^3}\right) \tag{5.58}$$

where a_h is the half side length of the square diaphragm, b is half side length of the boss, t is the thickness of the diaphragm, and A_p is a stiffness coefficient which depends on the solidity ratio b/a:

$$A_p = \frac{3(1-\nu^2)}{16}\left(1-\frac{b^4}{a_h^{\,4}}-4\frac{b^2}{a_h^{\,2}}\log\frac{a_h}{b}\right) \tag{5.59}$$

After deflection under pressure, the rigid part of the diaphragm is still parallel to the fixed electrode. Therefore, the changed capacitance can be calculated from Equation 5.50:

$$C = \frac{\varepsilon_0\varepsilon\cdot A}{d-w_c} \tag{5.60}$$

5.6.2.3 Dimensions of the Diaphragms

The sensor was assumed to be under no pressure when determining the dimensions of the diaphragms. This means that the pressure inside the cavity (formed by the two electrodes) is at atmospheric pressure. Both the flat diaphragm and the bossed diaphragm are made of silicon and their cross-sections are shown in Figure 5.22.

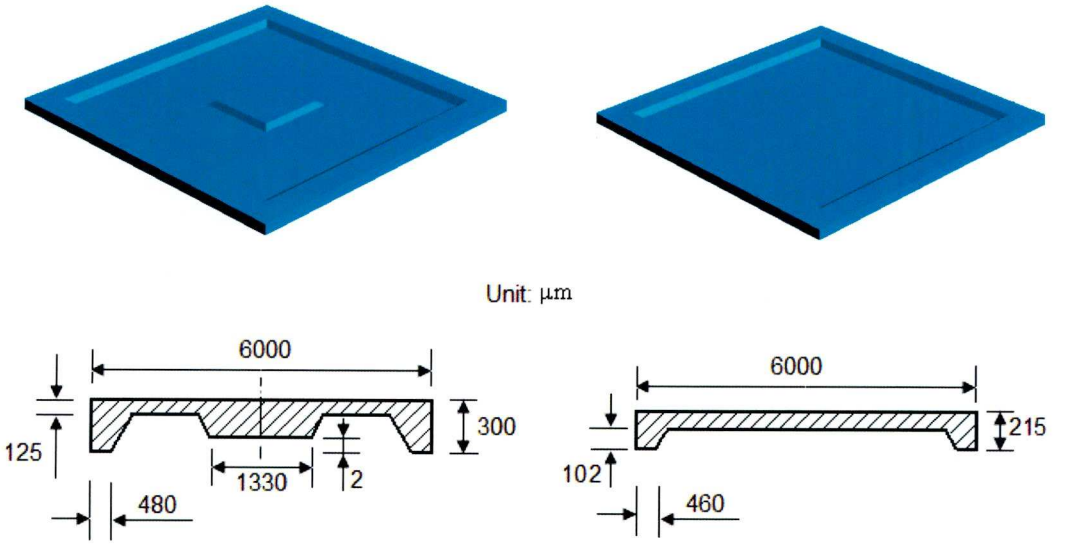

Figure 5.22 Dimensions of the flat and bossed silicon diaphragms.

5.6.2.4 Diaphragm Displacement

As the two diaphragms have a relatively complex geometry, the deflections under applied pressure are more readily determined by the finite element method. CoventorWare was used to simulate the displacement of the two diaphragms when a pressure of 350mmHg is applied. Because of the symmetry of the diaphragms, only one quarter of the diaphragms needs to be modelled in order to

save the simulation time. The results are shown in Figure 5.23.

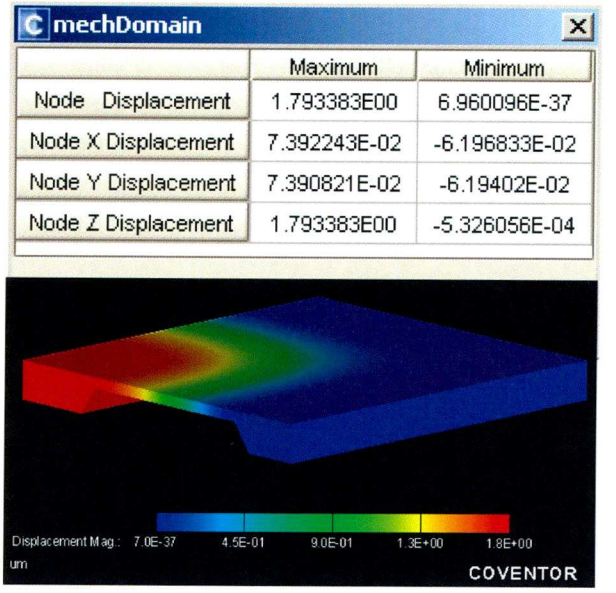

a

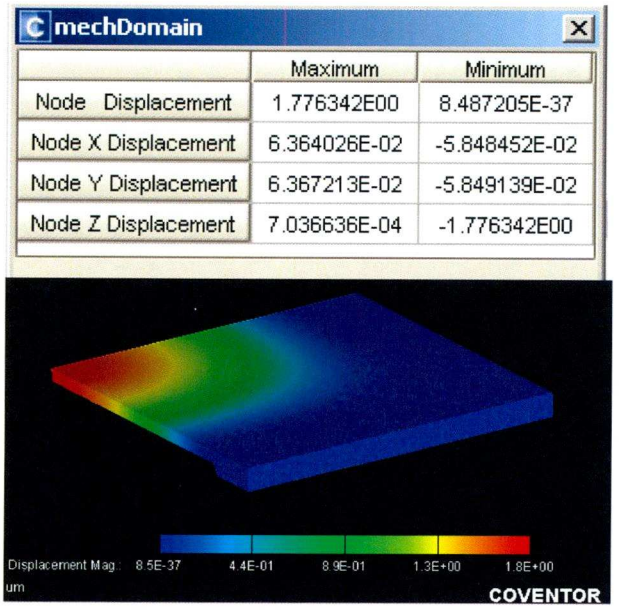

b

Figure 5.23 Displacement of the (a) bossed diaphragm; (b) flat diaphragm under the maximum applied pressure of 350mmHg (0.047MPa).

It can be seen from the figure that the maximum displacement (Z direction) occurs at the central point of each diaphragm. This value is 1.79μm for the

bossed diaphragm and 1.78μm for the flat diaphragm. As discussed in Section 5.6.1, the gap between the two electrodes of Sensor 1 and Sensor was set as 2μm. Hence the two moveable electrodes do not touch the fixed electrodes at the maximum designed pressure (350mmHg). Figure 5.23 also reveals that the deformation is more uniform in the central portion of the bossed diaphragm than that in the flat diaphragm.

CoventorWare was also used to compare the linearity of the maximum displacement of the bossed diaphragm and the flat diaphragm with applied pressure from 0 to 350mmHg and the result is shown in Figure 5.24. It can be seen that the displacement in the central point of each diaphragm shows a high degree of linearity. This is because the displacements are quite small compared to the thicknesses of these diaphragms (the ratio of the displacement to diaphragm thickness is 1:70 for the bossed diaphragm and 1:63 for the flat diaphragm). In general, when this ratio is less than 30%, the displacement of a diaphragm can be considered as linear [Beeby, 2004(1)].

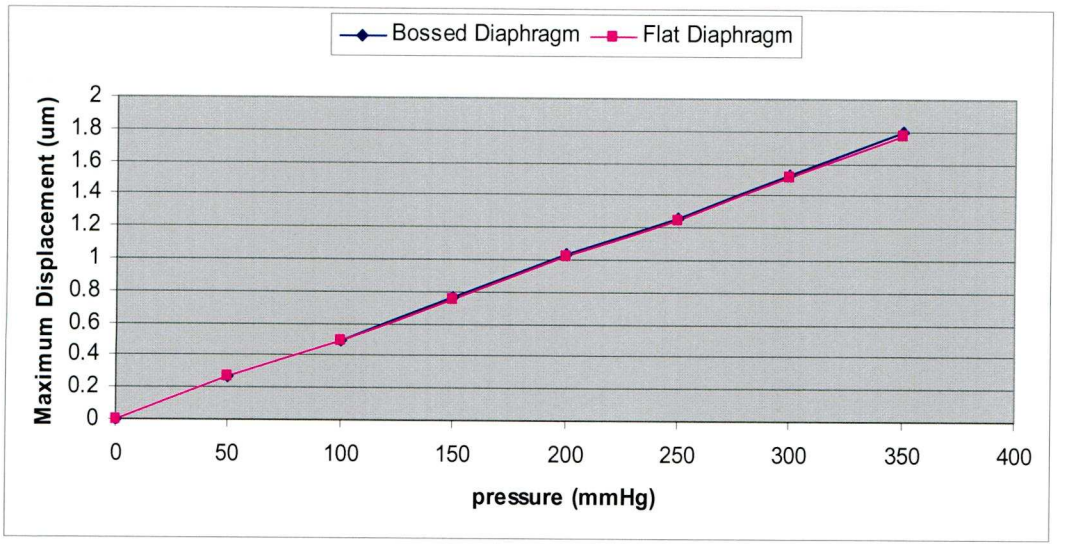

Figure 5.24 Comparison of the linearity of displacement for the bossed and flat diaphragms at their central points.

5.6.3 Capacitance Change

The change of capacitance of the sensors' capacitive components in response to applied pressures can be found in Figure 5.25. Finite element method was used to carry out the simulation for Sensor 2 which has the flat diaphragm. The two electrodes of Sensor 1 are assumed to be still parallel with the applied pressures. Therefore, the calculation of the capacitance changes was based on Equation 5.60.

It can be seen from the figure that the capacitance changes of each sensor in response to applied pressure is nonlinear, especially when the pressure is over 250mmHg. The linearity of Sensor 1 is lower than Sensor 2 in terms of capacitance changes.

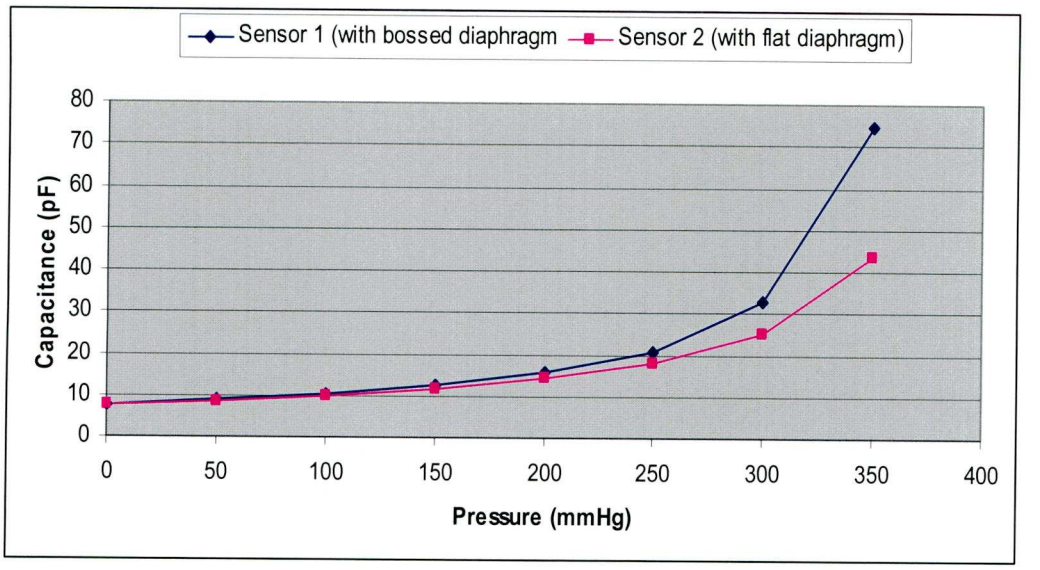

Figure 5.25 Capacitance change with applied pressure for Sensor 1 and Sensor 2.

5.6.4 Frequency versus Capacitance

The shift of resonant frequency of each sensor in response to capacitance changes was calculated from Equation 2.1. Figure 5.26 shows the relationship between the resonant frequency and the capacitance for Sensor 1 and Sensor 2. The capacitance values in these figures were based on the applied pressure from 0 to 350mmHg. These results show that change of the capacitance for both sensors are not linear, which is totally different from the maximum displacement of these two diaphragms.

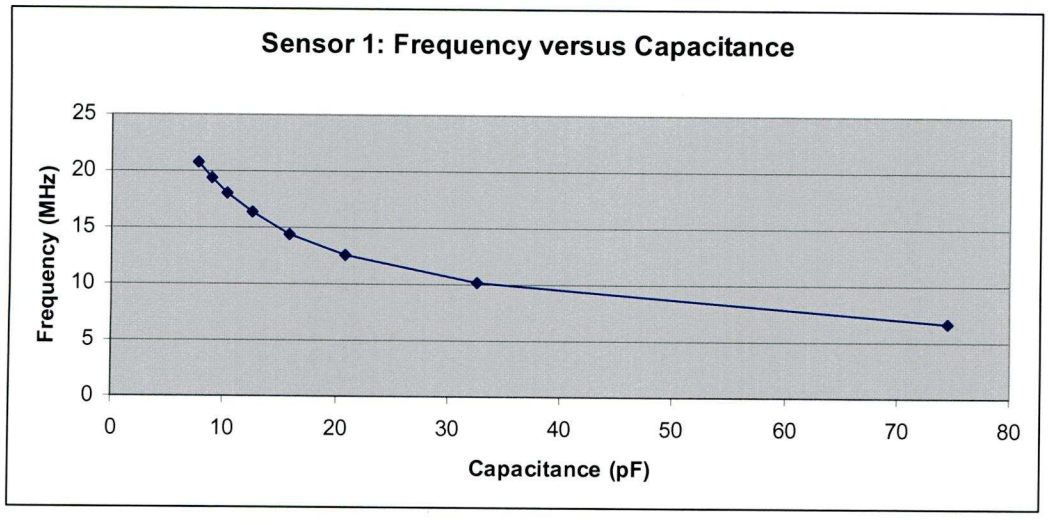

a

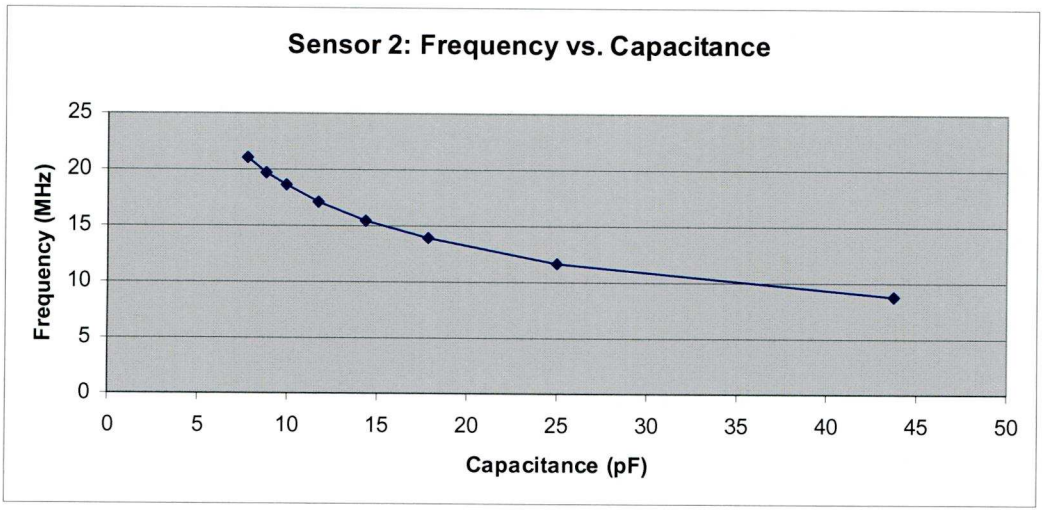

b

Figure 5. 26 Frequency change in response to capacitance changes for (a) Sensor 1; (b) Sensor 2.

5.6.5 Frequency versus Pressure

The changes in resonant frequency of each sensor in response to pressure changes in the range of 0-350mmHg are shown in Figure 5.27. It can be seen that although the relationship between the resonant frequency and pressure for the two sensors is nonlinear, they may be assumed to be linear over the range

0-350mmHg. It is also notable that Sensor 1 has a higher pressure sensitivity than Sensor 2. This is because the bossed diaphragm in Sensor 1 causes greater capacitance changes with applied pressure. The sensitivity for Sensor 1 is 40.27kHz/mmHg and for Sensor 2 is 34.95kHz/mmHg.

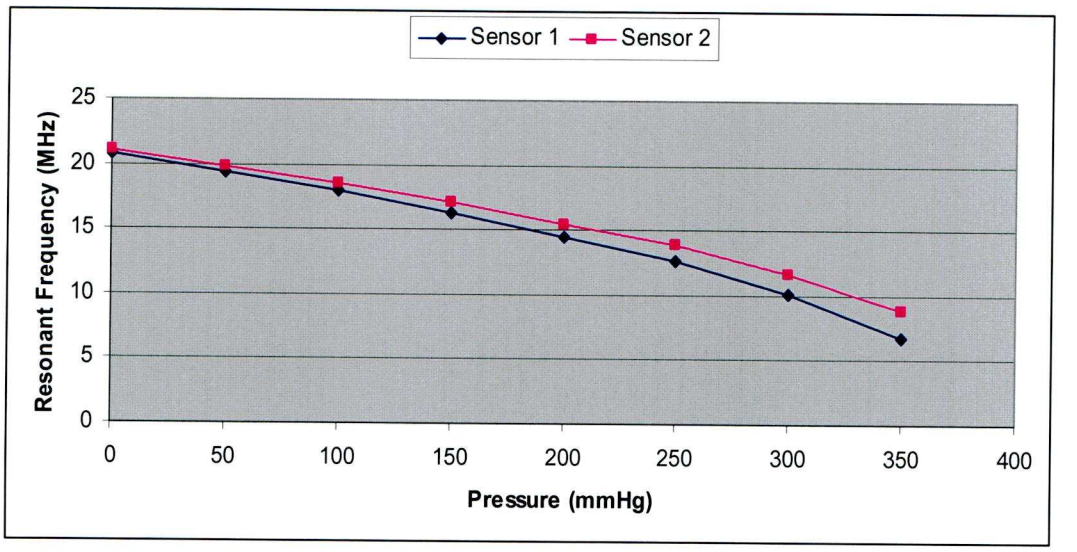

Figure 5.27 Resonant frequency of Sensor 1 and Sensor 2 with applied pressure.

References

Akar O., Akin T., and Najafi K., A wireless batch sealed absolute capacitive pressure sensor, *Sensors and Actuators A95*, (2001) 29–38.

Beeby, S. P. etc., *MEMS Mechanical Sensors*, Publisher: Artech House, Inc., Norwood, America, 2004.

Bin T. Y., Huang R. S., A thin diaphragm capacitive pressure sensor simulator, *Sensors and Actuators*, 11 (1987), pp. 1-22.

Butterworth S., Effective resistance of inductance coils at radio frequency, Parts I&II, *Experimental wireless and the wireless engineer*, April 1926, pp. 203-210 & 309-316

Carchon G.J., Raedt W. De, Integrated inductors, Integrated Passive Component Technology, chapter 10, *IEEE Press*, Piscataway, NJ, 2003, pp. 191–245,

Cheng D. K., *Field and wave electromagnetics*, Publisher: Addison-Wesley, USA, 1989.

Danesh M., and Long J. R., Differentially driven symmetric micro-strip inductors, *IEEE Trans. Microwave Theory Tech.*, Vol. 50, 2002, pp. 332 – 341.

DeHennis A. D., and Wise K. D., A wireless microsystem for the remote sensing of pressure, temperature, and relative humidity, *Journal of Microelectromechanical System*, Vol. 14, No. 1, Feb. 2005, pages 12-22.

Fastmodel, Version 1.30, Software package, accessed in August 2007, available website: http://www.fastfieldsolvers.com/fastmodel

Finkenzeller K., *RFID Handbook*, 2nd Ed., John Wiley & Sons, 2003.

Ghatak A. K., Thyagarajan K., Electromagnetic Analysis of the Simplest Optical Waveguide, *Optical Electronics*, Cambridge Univ. Press, 1989, pp.315-342.

Greenhouse H. M., Design of planar rectangular microelectronic inductors. *IEEE Trans. Parts, Hybrids, Packaging*, PHP-10(2), June 1974, pp. 101-109.

Grover F.W., *Inductance calculations: working formulas and tables*, Van Nostrand, Princeton, NJ, 1946; Reprinted by Dover Publications, New York, NY, 1962.

Hickman I., *Practical Radio-frequency Handbook*, Publisher: Newnes, 4th Edition, Sep. 2006.

Johnson C. C., and Guy A. W., Nonionizing electromagnetic wave effects in biological materials and systems, *Proc. IEEE*, vol. 60, 1972, pp. 692-720.

Johnson D. E., Johnson J. R., et al., *Electric Circuit Analysis*, Chapter 15, Publisher: John Wiley & Sons, Inc., 1999.

Kim E. H., Kong Y. J., et al., Temperature changes caused by 13-MeV Proton Irradiation at the Interface of a Pyrex Glass and a Silicon Wafer, *Journal of the Korean Physical Society*, Vol. 48, No. 4, Apr. 2006, pp. 859-861.

Lee J. M., et al., Comparison of frequency responses of spiral inductors with different figures, *Semiconductor Science and Technology*, 16(2001), pp. 66-71.

Maluf, N., Williams, K., *An Introduction to Microelectromechanical Systems Engineering*, second edition, Publisher: Artech House, Inc., 2004.

Meyer R. G., Niknejad A.M., *Design, Simulation and Applications of Inductors and Transformers for Si RF ICs.*, Springer Netherlands, 2000, Chapter 7, pp. 97-101.

Musunuri S., Chapman P. L., et al., Design Issues for Monolithic DCDC Converters, *IEEE Transactions on Power Electronics*, vol. 20, No. 3, May 2005, pp.639-649.

Neagu C. R., Gardeniers J., et al., An electrochemical micro-actuator: principle and first results. *Journal of MEMS*, 51(1996), pp. 2–9.

Neagu C. R., Jansen H. V., et al., Characterization of a planar micro-coil for implantable Microsystems, *Sensors and Actuators A*, 62(1-3), 1997, pp. 599-611.

Neagu C. R., *A Medical Microactuator based on an Electrochemical Principle*, PhD thesis, Micromechanics of the MESA Research Institute, University of Twente, Enschede, the Netherlands, 1998.

Ong K.G. et al., Design and application of a wireless, passive, resonant-circuit environmental monitoring sensor, *Sensors and Actuators A*, 93 (2001), pp. 33-43.

Park Y. K., et al., Dynamic Investigation of a Binocular Six-component Force-moment Sensor, *Measurement Science and Technology* 13 (2002), pp. 1311-1318.

Peters J., *Design of High Quality Factor Spiral Inductors in RF MCM-D*, Master thesis, Engineering in Electrical Engineering and Computer Science,

Massachusetts Institute of Technology, Sep. 2004.

Pieters, P., Truzzi, C., *Thin-film-on-glass technology for the integration of passive devices*, TAP Technology, 2nd edition, 2001, pp. 45–50.

Rosengren L., A system for passive implantable pressure sensors, *Sensors and Actuators A*, 43 (1994), pp. 55-58.

Serway R. A., *Principles of Physics*, 2nd Edition, Fort Worth, Texas, 1998, p. 602.

Sonnet Lite, Version 11.53, Software package, accessed in August 2007, available website: http://www.sonnetusa.com/products/lite/

Terman, F.E., *Radio Engineers Handbook*, McGraw-Hill, London, 1943, pp. 46-78.

Wan N., et al., Design and Modelling of a High-Q On-chip Hairpin Inductro for RFIC Applications, *IEEE Radio Frequency Integrated Circuits Symposium*, 2003, pp. 547-550.

Wang W. J., Modelling and characterisation of a silicon condenser microphone, *Journal of Micromechanics and Microengineering*, 14(2004), pp. 403-409.

Welsby V. G., *The Theory and Design of Inductance Coils*, London: Macdonald, 1950.

Yue C. P., and Wong S. S., Design strategy of on-chip inductors for highly integrated RF systems, *Proc. Design Automation Conf.*, June 1999, pp. 982 – 987.

Chapter 6
Recommended Sensor Fabrication Process

This chapter suggests the fabrication processes of the two proposed LC resonant type pressure sensors. In Section 6.1, two techniques for fabricating low resistance micro-coils are reviewed. Section 6.2 describes the fabrication process of the two coils of the proposed sensors. The fabrication processes of the flat and the bossed diaphragms are recommended in Section 6.3. Section 6.4 deals with the wafer bonding processes of the micro-coils and the pressure sensing diaphragms using silicon fusion bonding and anodic bonding technologies. An experiment which measures the change of resonant frequency of an LC circuit is described in Section 6.5. Section 6.6 presents a pilot study of wireless detection technology and finally the estimated cost of the sensor based on the suggested fabrication process is shown in Section 6.7.

6.1 Review of Fabrication Techniques for Low-Resistance Coil

As revealed in Chapter 5, planar spiral coil is the critical component in an LC resonant type pressure sensor. In order to fabricate a high Q coil, substrate and ohmic losses of this coil must be minimised. For Sensor 1, its coil is designed to be built on a silicon substrate; the reduction of substrate loss can be achieved by

adding thick insulating layer between the coil and the silicon substrate. As for Sensor 2, its coil is constructed on Pyrex glass and the substrate loss is negligible. To reduce the ohmic losses of the coils, one strategy is to build thick metal tracks with high aspect ratio, which is the main challenge of the sensor fabrication.

There is no standard procedure for fabricating micro-coil in MEMS industry, especially for coil with thick metal lines. From literature search, two techniques, copper damascene and UV-LIGA have been used to fabricate low-resistance coils [Wu, 2003; Guthrie et al., 2007; Sadler, 2001; Li et al., 2008]. These two techniques will be reviewed briefly in the following sections.

6.1.1 Copper Damascene

Copper damascene was first developed by IBM for the fabrication of chip inter-connect structures [Andricacos, 1998]. The key technique used in a copper damascene process is called 'super-filling'. Due to surface topology, the electric field in the copper plating bath is distributed non-uniformly. As a result, the copper growth rate at the top surface of the substrate is higher than the rate in the trenches, leading to voids in the final structures (Figure 6.1a). Even with conformal electroplating, seams are frequently seen in the structure (Figure 6.1b). In order to enhance the filling capability, levelling agents are added to the electrolyte to enable a higher copper growth rate in the trenches than that on the

top surface and sharp corners (namely 'super-filling') [Chiu, 2000]. By using this technique, void-free and seamless copper deposits can be obtained (see Figure 6.1c).

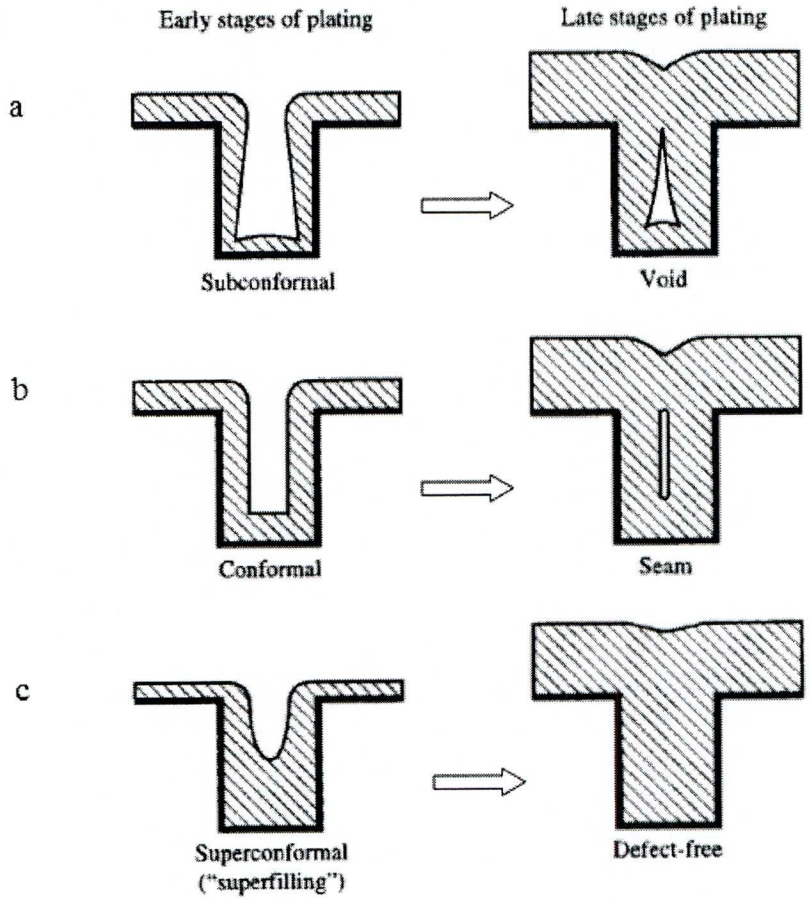

Figure 6.1 Types of profile by copper electroplating [Andricacos, 1998].

The use of copper damascene technique for the fabrication of a planar coil is demonstrated in Figure 6.2. This process starts with etching deep trenches into a silicon wafer either by RIE or DRIE. The surface of these trenches and the wafer is then oxidised to provide an insulation layer for the copper layer to be deposited. This is followed by depositing a seed layer on the insulation layer by an evaporation or sputtering process. This seed layer acts as an adhesive layer

which bonds the silicon substrate and the copper layer. Subsequently, copper is then grown in these trenches and on the top surface of the substrate by electroplating. Finally, the excess copper layer is removed by a chemical-mechanical polishing process.

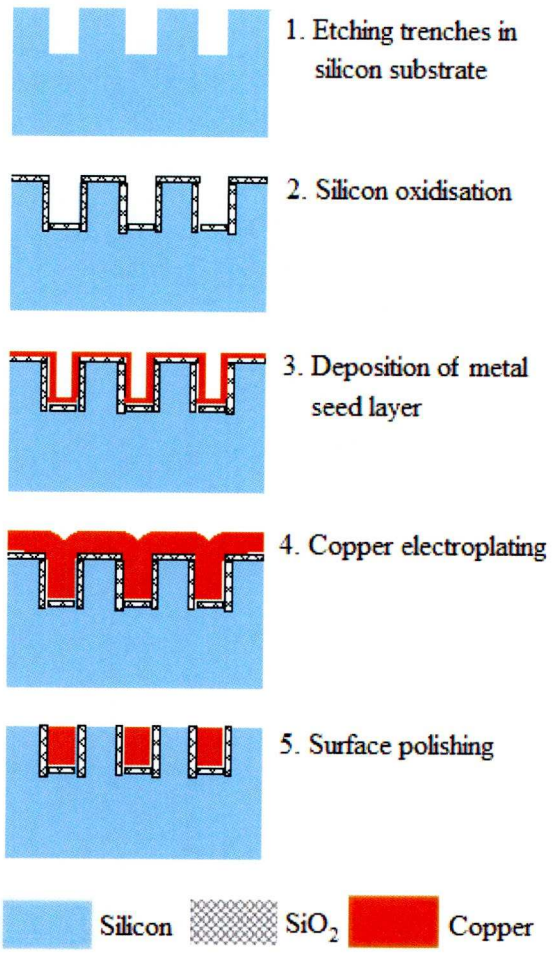

Figure 6.2 Copper damascene technique for planar micro-coil [Wu, 2003].

A limitation of copper damascene is that it is typically used to produce metal lines which are less than a few micrometers thick [Wu, 2003]. This is because thick metal lines will inevitably result in a thick excess metal layer on the wafer surface and a lengthy polishing process is needed to remove this top copper

layer.

6.1.2 LIGA

LIGA is the acronym of the German terms lithography (Lithographie), electroforming (Galvanoformung) and moulding (Abformung). It is a micromachining process for facilitating thick microstructures. Figure 6.3 shows the fabrication steps of a planar micro-coil using this technique [Wu, 2003].

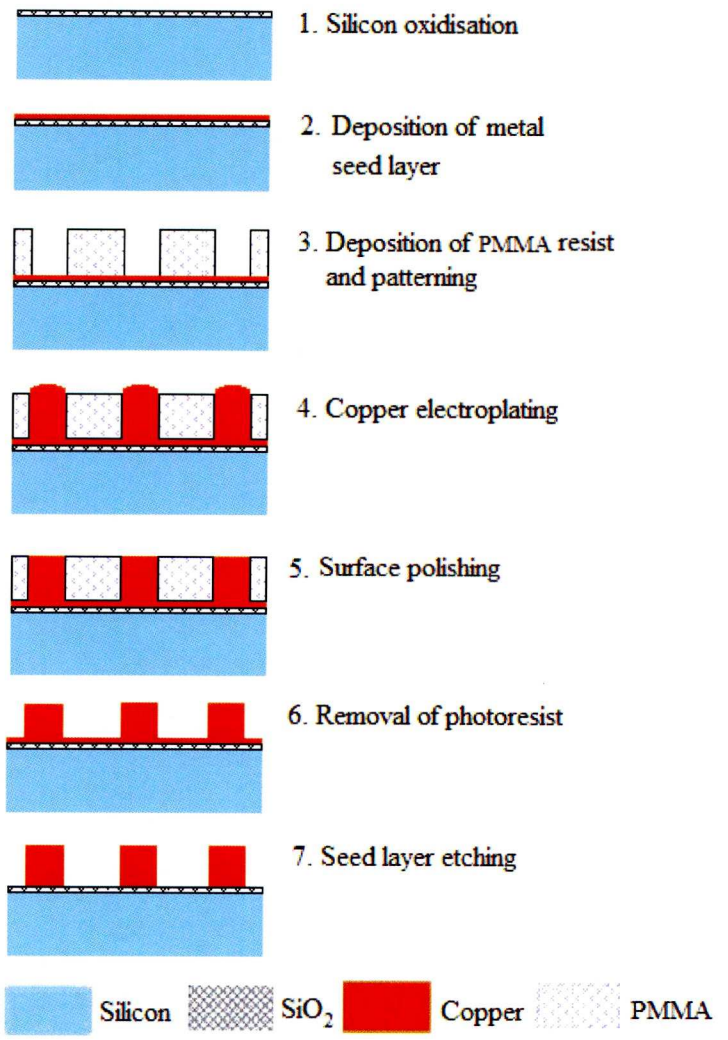

Figure 6.3 A LIGA process for planar micro-coil fabrication [Wu, 2003].

The process starts with the oxidisation of the surface of a silicon wafer, which is followed by depositing of a metal seed layer. A thick resist layer (usually PMMA) is then spun onto the top surface. This resist layer is exposed to synchrotron X-ray radiation through a mask (usually made of gold). The exposed resist layer is then developed to form deep trenches (mould). An electroplating process is followed to grow copper in these trenches. CMP is then used to remove the copper over-plate. Finally, the mould and the exposed seed layer are removed to release the microstructure.

The use of high energy X-ray sources (e.g., synchrotrons or linear accelerators) in a LIGA process enables structures with near vertical sidewalls and aspect ratios of more than 100:1 to be made. Structure with feature as thick as 2mm was demonstrated successfully using this technique [Matteucci, 2006]. LIGA is expensive because of the masks and the X-ray facilities used in this process. However, with the help of thick photo-resists such as SU-8 or AZ9260, thick microstructures can be formed and the high cost X-ray source is replaced by a standard UV light, namely UV-LIGA [Judy, 2001].

6.2 Fabrication Processes of the Coils

Based on the copper damascene and LIGA techniques, two process chains were selected for the fabrication of the coils of the proposed sensors. Figure 6.4 shows the fabrication steps of the glass based square spiral coil.

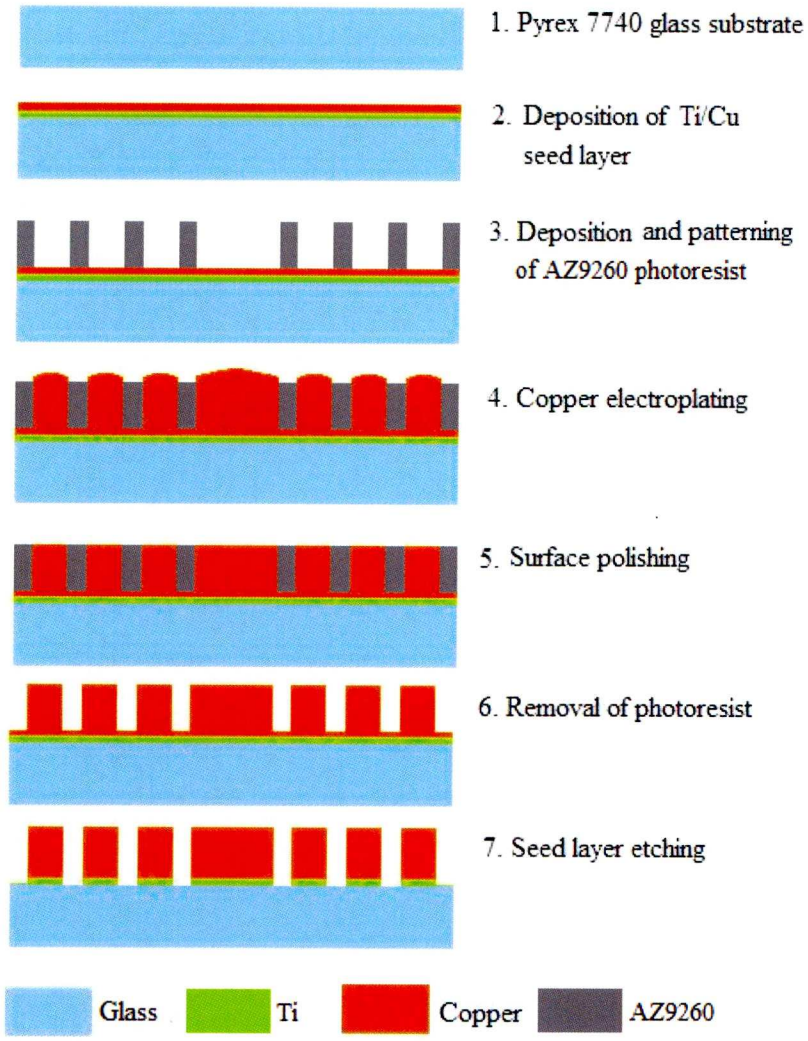

Figure 6.4 Fabrication steps of the glass based square spiral coil.

First, a 15nm titanium (Ti) layer and a 100nm copper (Cu) layer are subsequently sputtered on the surface of a Pyrex 7740 glass wafer, acting as the seed layers for the electroplated copper layer. A 100μm thick of AZ9260 photo-resist layer is then spun onto the wafer. After the development and hard bake of the photo-resist, the wafer is immersed into an acid copper electroplating bath, which mainly contains copper sulphate ($CuSO_4$), sulphuric acid (H_2SO_4), hydrochloric acid (HCl) and suppressor additives, to enable copper growing in these trenches.

After the electroplating process, the wafer is placed on a polisher pad to remove the excess copper deposits by CMP. The photo-resist is subsequently dissolved and removed in acetone, isopropyl alcohol and deionised (DI) water. Finally, the seed layers are etched in $CuSO_4$+NH_4OH solution and HF for the Cu and Ti respectively.

For the silicon based coil, the process starts from depositing a 2μm thick SiO_2 layer by plasma enhanced chemical vapour deposition (PECVD). A 2μm thick AZ9260 photo-resist layer is then spun onto the top surface of the silicon wafer. The photo-resist is patterned and developed in order to etch the SiO_2. The etched AZ9260 and SiO_2 layers act as an etch mask for DRIE. A DRIE process is followed to etch trenches with depth of 30μm. A second PECVD SiO_2 layer with a thickness of 2μm is deposited onto the surfaces of the trenches and the top surface of the wafer as an insulation layer. Afterwards, a 15nm/100nm Ti/Cu seed layer is sputtered. A CMP process is followed to remove the top seed layer. Then copper is electrodeposited in these trenches and finally the excess copper on the top surface of the wafer is removed through CMP. The fabrication process chain is shown in Figure 6.5.

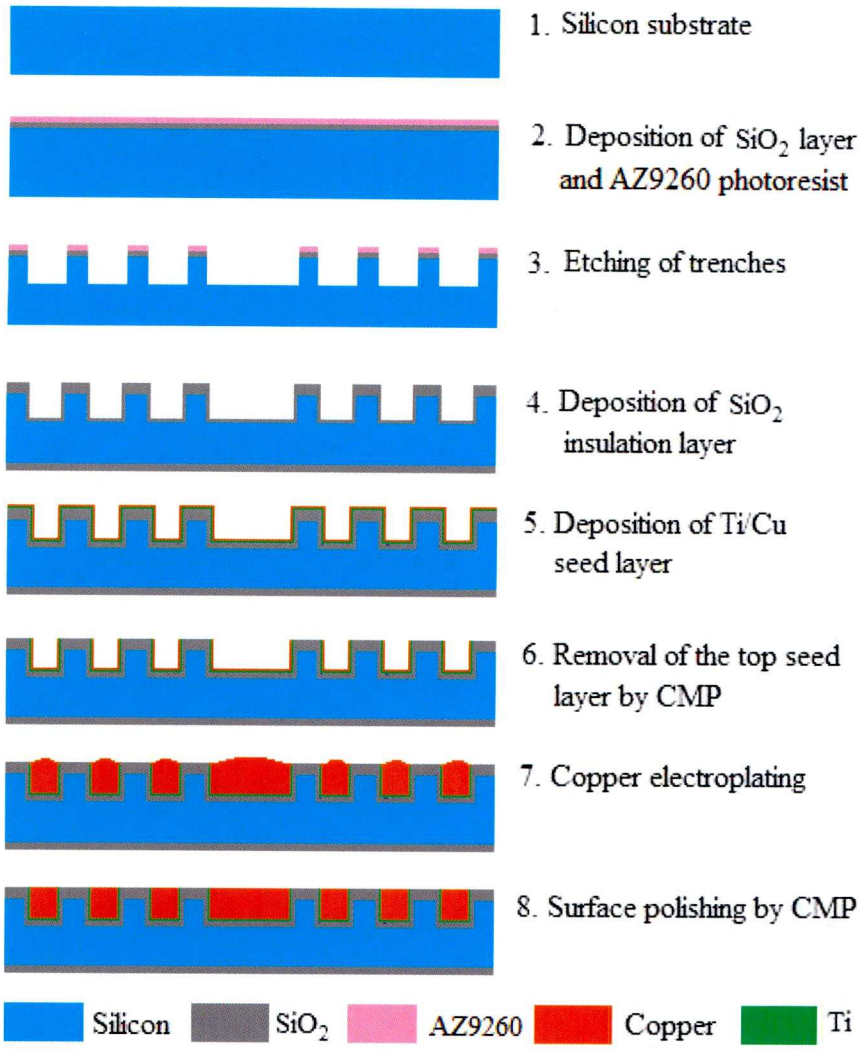

Figure 6.5 Fabrication process of the silicon based planar coil.

6.3 Fabrication Processes of the Diaphragms

The fabrication of the pressure sensing diaphragms is accomplished through anisotropic wet etching. Figure 6.6 shows the fabrication process of the bossed diaphragm. It begins with the oxidation of the front and back of a 300μm thick silicon wafer to grow two 1μm thick SiO_2 mask layers. A 4μm thick AZ9260 photo-resist is spun onto the front side and back side of the wafer. The back of the AZ9260 is patterned and developed as the etch mask of the underneath SiO_2

layer. The wafer is then immersed in a HF solution to etch the SiO_2 layer. This is followed by etching 2μm silicon substrate in a TMAH anisotropic etchant. A second 2μm thick SiO_2 layer is thermally grown on the backside of the wafer. This SiO_2 layer is then patterned and etched. The backside silicon is etched anisotropically in TMAH with the etch depth of 173μm. It is followed by boron doping is to make it electrical conductive and finally the SiO_2 layer is removed.

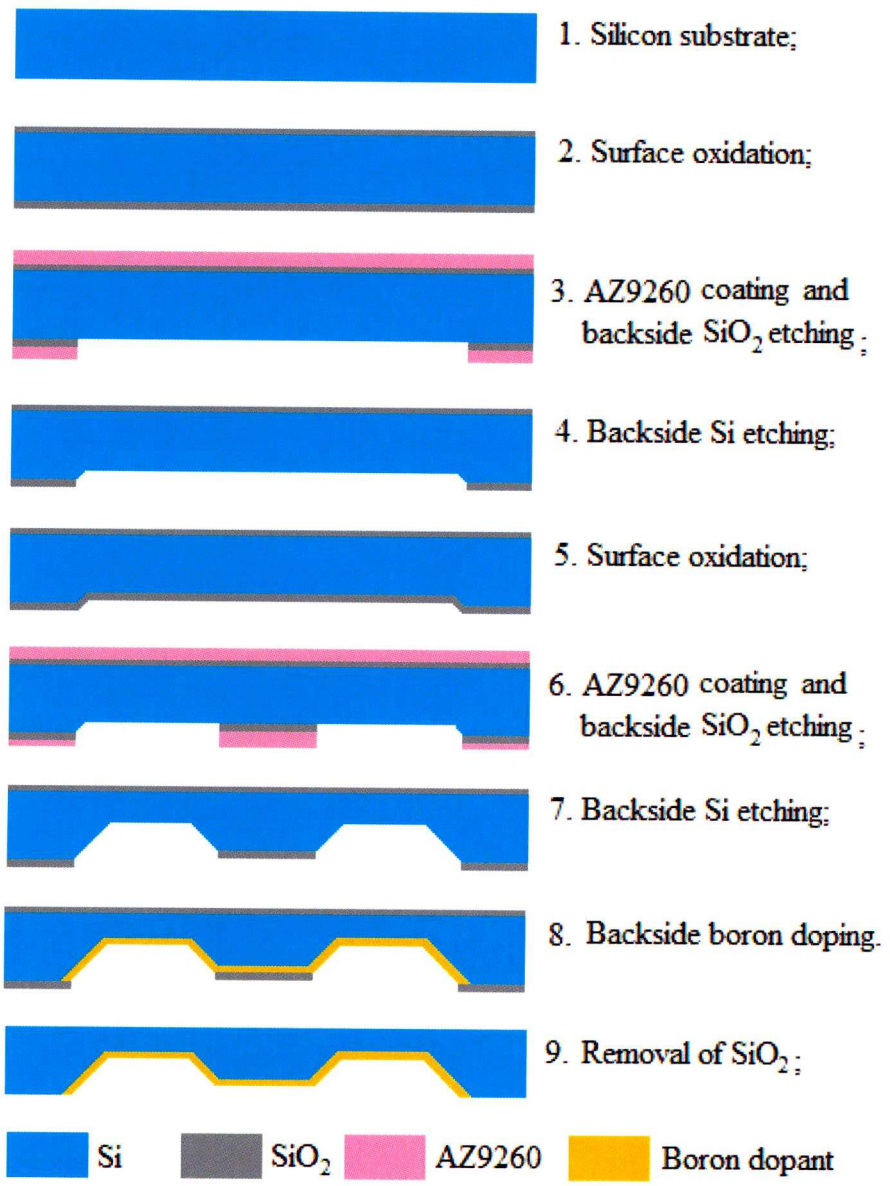

Figure 6.6 Fabrication process of the bossed diaphragm.

The fabrication steps of the flat diaphragm are quite similar to that of the bossed diaphragm. The process is described as follows:

A 300μm silicon wafer is thinned to 215μm through a mechanical polishing process. The wafer is then oxidised on its both sides and the back SiO_2 is patterned and etched in HF. Next, the wafer is immersed in a TMAH etchant to etch the back side silicon with a depth of 102μm. Subsequently, the back side is doped with boron and finally the SiO_2 layer is etched. The fabrication process chain is shown in Figure 6.7.

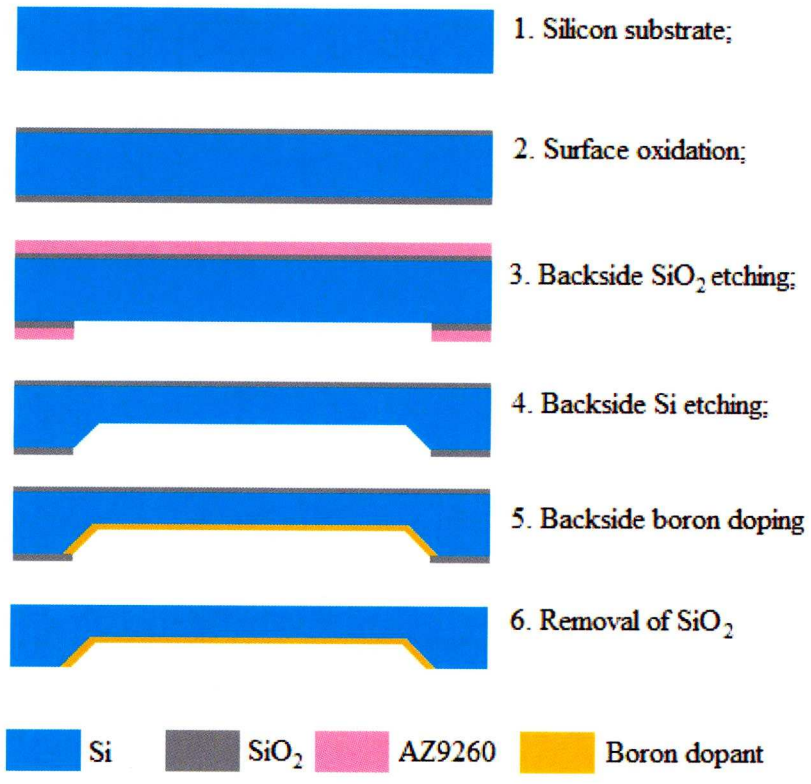

Figure 6.7 Fabrication process of the flat diaphragm.

6.4 Wafer Bonding

The final step is to bond these wafers together to form the sensor structures. First, the two silicon wafers are bonded through a silicon fusion bonding process. The silicon wafer, which has the flat diaphragms on it, is polished on its surface to achieve a high quality of flatness. It is then boiled in ammonia water to make its surfaces hydrophilic.

Afterwards, this wafer is aligned and attached to the silicon wafer which is embedded with the copper coil. The assembly is then heated to about 500°C to strengthen the bond. The cross section of this final structure can be seen in Figure 6.8a. The bonded structure of the silicon wafer and the glass wafer is shown in Figure 6.8b. Anodic bonding technique is used to build this sensor structure. The two wafers are attached together and are heated to a temperature of 350°C. A 1kV DC voltage is connected to them through two electrodes and the wafers are bonded together tightly due to the strong electrostatic forces.

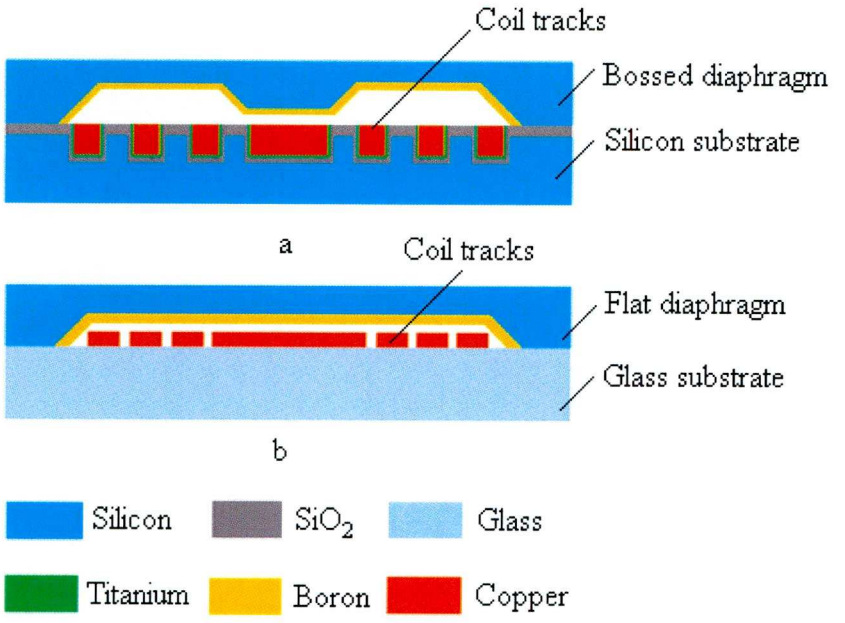

Figure 6.8 Cross-sectional views of the bonded structures. (a) silicon wafer with the bossed silicon diaphragm and the silicon wafer with the embedded coil; (b) silicon wafer with the flat diaphragm and the glass wafer with the coil on.

6.5 Experiment for Detecting Resonant Frequency

6.5.1 Purpose

Due to laboratory and resource constraints, the fabrication and test of the two proposed pressure sensors were outside the remit of this investigation. However, in order to verify the feasibility of the sensor operating principle, an experiment was carried out to measure the changes of resonant frequency of an LC circuit in response to the capacitance changes of its capacitor.

6.5.2 Method and result

A copper wire was wound onto a cylindrical object to form a solenoid coil. It was then connected to a capacitance variable capacitor to form an LC resonant

circuit. The capacitance range of this capacitor was from 0 to 50pF. This LC circuit was connected to a Network Analyzer (HP 8753) using a coaxial cable. Figure 6.9 shows the measurement configuration, including the LC circuit and the network analyzer.

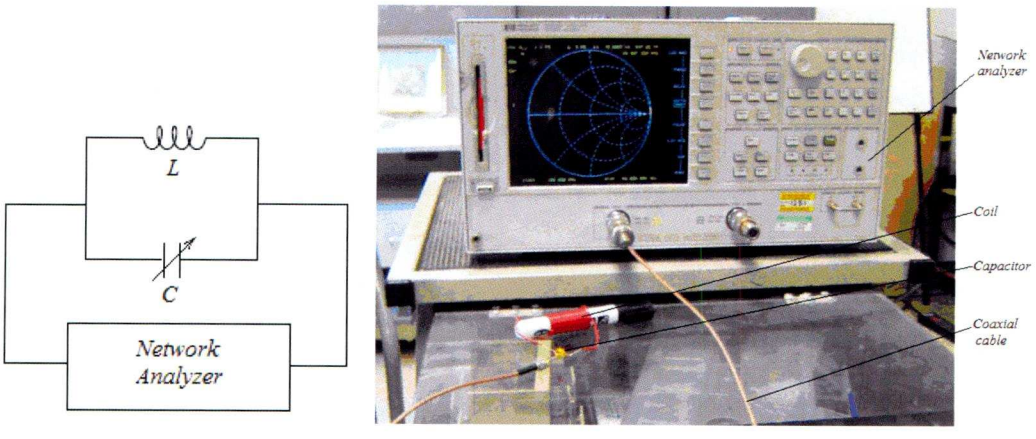

(a) (b)

Figure 6.9 The measurement of the resonant frequency of a LC circuit: (a) measurement configuration; (b) test equipment.

Network analyzers are frequently employed to measure the scattering parameters (S-parameters) of two-port high-frequency electrical circuits. S-parameters are subsequently used to analyse the network properties such as the resistance, capacitance, inductance and resonant frequency of the circuit. The measured resistance and inductance of the solenoid are 0.5Ω and 7.55μH, respectively. The capacitance of the capacitor was adjusted to values from 5pF to 40pF with an increment of 5pF. The resonant frequencies of this circuit at different capacitances were then detected according to the changes of Return Loss S-

parameter (S_{11}). Figure 6.10 shows the change of S_{11} at different frequencies and the resonant frequency is about 26.25MHz where the Return Loss S_{11} is at its lowest. The relationship of the measured resonant frequencies and the capacitances of the capacitive component of the circuit is shown in Figure 6.11.

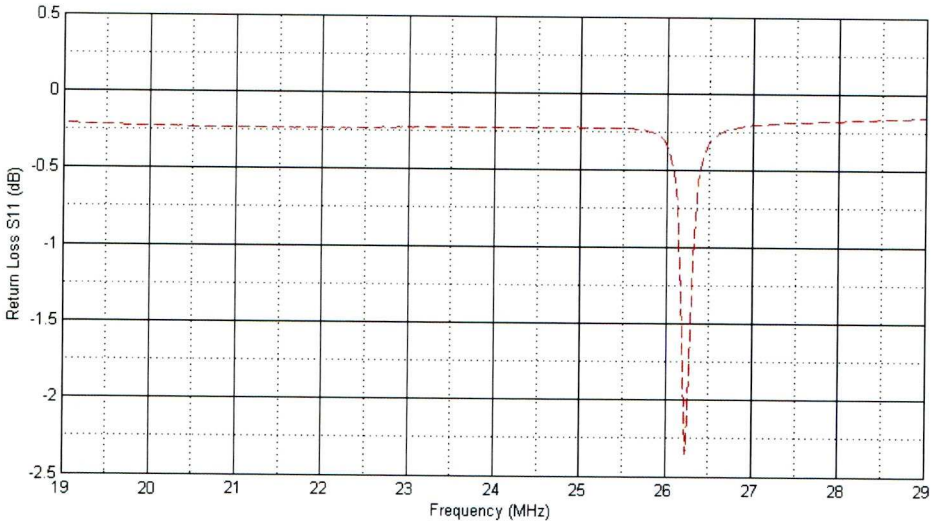

Figure 6.10 The detection of resonant frequency of an LC circuit based on S11.

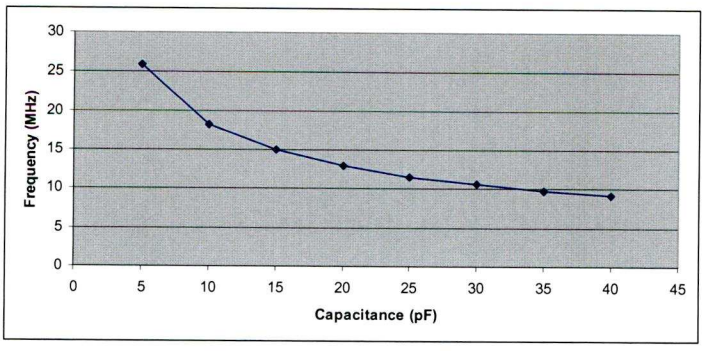

Figure 6.11 Measured resonant frequencies with capacitance changes of its capacitive component.

6.5.3 Discussion

It was intended to use this experiment to prove that an LC circuit has a resonant frequency and this frequency changes with the variation of the capacitance of its capacitor. Figure 6.10 and 6.11 show clearly that the resonant frequency of an LC circuit can be measured using a network analyzer and it varies with the capacitance change. Comparing these results to that which are shown in Figure 5.26, it can be seen that they agree quite well and the frequency change is nonlinear in response to capacitance changes. This nonlinearity can be explained from Equation 2.1 which defines the relationship between the resonant frequency and its capacitance of an LC resonant circuit.

Initially, the construction of the coil was considered to use the metallic structure on a stent-graft to form a solenoid. The advantage of this configuration is that a coil with large inductance and low resistance can be realised and therefore the detectable distance between the embedded sensor and outside detecting device can be maximised. However, it was found that the inductance of the coil changed slightly during the measurement. This is because that the two ends of this coil were not fixed and they changed their positions when the capacitance of the capacitor was adjusted during the experiment. This implies that the idea of fixing a flexible coil on the outside lumen of the stent-graft used for an AAA patient is impractical, because the inductance of this coil would be affected by the relative position of each turn due to the movement of the blood flow and the body.

6.6 A Pilot Study of Wireless Detection Technology

Currently, the author is working as a research assistant and is responsible for developing a wireless force transducer used to measure the axial transmission force and torque exerted on a guide wire or catheter during a medical interventional procedure. The transducer is based on the same principle as the pressure sensor designed for this PhD thesis. In order to investigate the most effective and practical detection system for activating the transducer and receiving signals emitted from it, a pilot study was carried out in collaboration with Dr. Z. M. Huang at the Department of Electrical Engineering and Electronics, University of Liverpool in July 2008. This system comprises of a network analyzer, a computer and a single loop antenna (Figure 6.12).

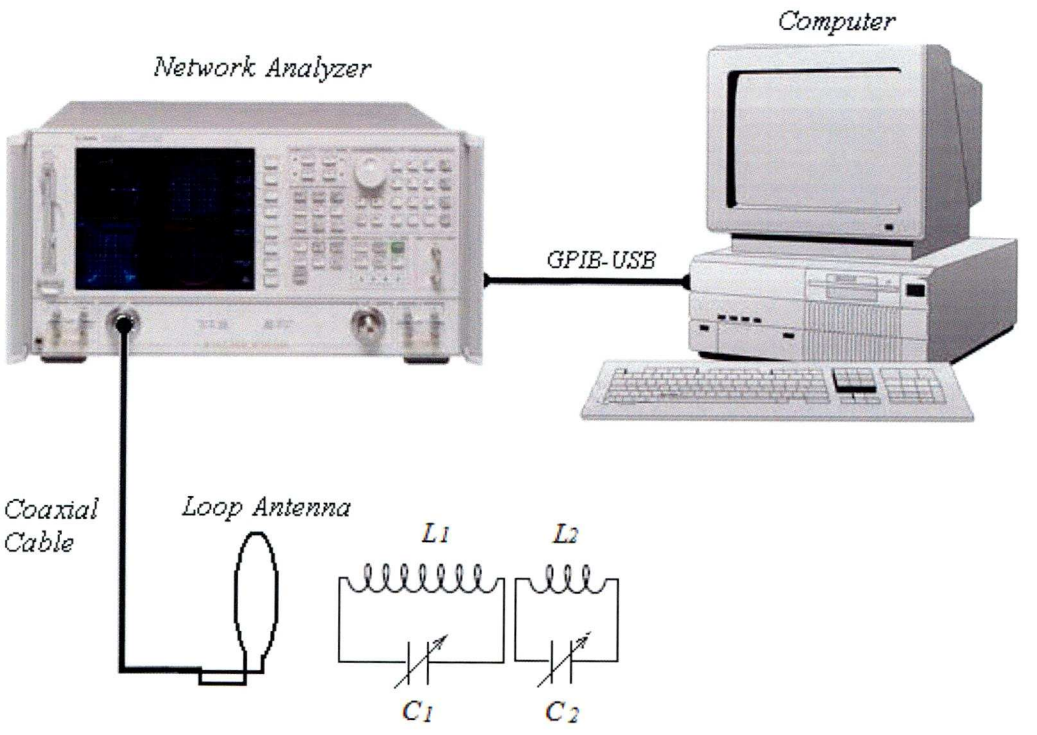

Figure 6.12 A system for wireless detection of the resonant frequencies of two LC circuits

The network analyzer was used to generate a magnetic field through the loop antenna which stimulates the two LC resonant circuits. It was also used to measure the Return Loss S_{11} of the system in order to determine the resonant frequencies of the two circuits. The computer was used to accurately capture the peak value of S_{11}. The two circuits consist of two capacitors and two solenoid coils with diameters of 20mm and have resonant frequencies of 28MHz and 45MHz, approximately. By optimising the size of the reader antenna a maximum detectable distance of 8cm was achieved (Figure 6.13).

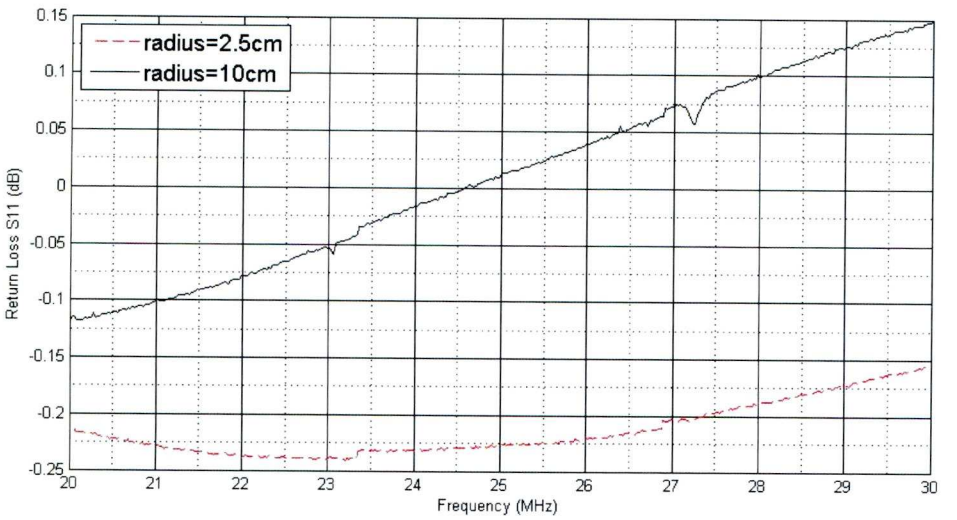

Figure 6.13 The effect of different size of reader antennas to the resonant frequency of an LC circuit placed 8cm away from the reader antenna.

This study shows clearly that the wireless detection of a passive LC type sensor is feasible. However, the maximum detectable distance of this system only reaches 8cm which may not be sufficient for an implantable pressure sensor even if there is not absorption of the RF wave by the body. In addition, the coil size in

the designed pressure sensor is significantly smaller than the coils used in this pilot study. And the alignment of the coil of the embedded pressure sensor with the antenna of the detecting system would be more difficult. Therefore, further studies are needed in order to apply this detection technique for measuring the resonant frequency of the implantable pressure sensor. Future research efforts are required to optimise the geometry of the antenna and improve the sensitivity of the detection system to increase the detectable distance.

6.7 Cost Evaluation

In Sections 6.2 to 6.4 it were shown what the preferred fabrication processes should be used for the proposed sensor. Currently no facilities are available at the University of Liverpool and therefore the manufacture of the sensor should be carried out commercially. Several MEMS companies have been approached in order to obtain estimates of the cost of fabrication. Two companies, SemeFab and Inex provided quotations ranged from £40,000 to £70,000. Clearly the cost of fabrication is likely to be very substantial and these will have to be taken into account in further extension of this project.

References

Andricacos, P. C., Uzoh, C., et al., Damascene Copper Electroplating for Chip Interconnections, *IBM J. Res. Develop.*, Vol. 42, 1998, p. 567-574.

Chiu S. Y., Characterization of additive systems for damascene Cu electroplating by the super-filling profile monitor, *J. Vac. Sci. Technol.*, B 18(6), Nov/Dec 2000, pp. 2835-2841.

Li W., Liang J. Q. et al., Design and fabrication of a micro-optic switch, Optics Express, Vol. 16, No. 9, 28 April 2008, pp. 6324-6330.

Guthrie H. C., Jiang M., Yang J. J., One Step Copper Damascene CMP Process and Slurry, *US Patent No.: US 7287314 B2*, 30 Otc., 2007, pp. 1-20.

Judy J. W., Microelectromechanical systems (MEMS): fabrication, design and applications, *Smart Materials and Structures*, 10 (2001), pp. 1115-1134.

Matteucci M., Perennes F., et al., Compact micro-pumping system based on LIGA fabricated micro-parts, *Microelectronic Engineering*, Volume 83, Issue 4-9, April-September 2006, pp.1288-1290.

Sadler D. J., Gupta S., and Ahn C. H., Micro-machined Spiral Inductors Using UV-LIGA Techniques, *IEEE Transactions on Magnetics*, Vol. 37, No. 4, July 2001, pp. 2897-2899.

Wu J., *Inductive links with integrated receiving coils for MEMS and implantable applications*, PhD thesis, the Department of Electrical Engineering, University of Notre Dame, Indiana, America, 2003.

Chapter 7
Conclusions

This chapter summarises the research results and gives some suggestions for future work.

7.1 Summary

This thesis presents the design and fabrication of a wireless pressure sensor for the detection of the pressure inside an aneurysm sac after an endovascular repair.

Chapter 1 introduced 'open surgical repair' and 'endovascular aneurysm repair (EVAR)', two treatment methods currently used for abdominal aortic aneurysm (AAA) repair. As the standard and well-proven procedure for AAA treatment, open surgical repair method has been widely used across the world since 1950s. Patients undergone this procedure do not need regular postoperative follow-up. However, this procedure is frequently associated with complications and it is not suitable for some high-risk patients. EVAR is an alternative for AAA treatment. It is less invasive and complications can be significantly reduced. The major problems associated with this procedure are stent-graft migration, failure and endoleaks. Therefore, lifetime surveillance after the treatment is needed.

Currently, the main follow-up surveillance techniques after EVAR include computerised tomographic (CT) scan and magnetic resonance imaging (MRI). But both of these techniques have limitations. For example, CT exposes the patient to irradiation and it involves the use of large volumes of nephrotoxic contrast agent; while MRI is a very expensive and time consuming procedure. These limitations led to the requirement of a non-invasive and cost efficient wireless pressure sensor to be developed.

In Chapter 2, wireless power supply methods for a medical implant were first reviewed. Power sources such as light, battery, mechanical vibration and magnetic field were discussed. The use of mechanical vibration, battery or light to provide energy for the proposed sensor is impractical. Because the sensor is supposed to be implanted inside the aneurysm sac which is optically opaque and no light source is available for generating power. It is also expected to remain in operation for a considerable period of time. As the space for implanting the sensor is limited, no such small size batteries are available at present to operate for a sufficiently long period inside the body. Power generated outside the body through mechanical vibrations or movements needs to be transferred wirelessly into the body. Still, technology for making an implantable, miniature kinetic energy generator is also immature. Different types of wireless pressure sensors which have the potential for the monitoring of intra-aneurysm sac pressures in the patients undergoing endovascular repair were introduced. These include

inductor-capacitor (LC) resonant frequency sensors, magnetoelastic thick-film sensors and passive surface acoustic wave (SAW) sensors. LC type wireless sensors have been explored extensively for medical implantation purposes. However, parasitic effects including parasitic resistance and parasitic capacitance are the main concern for developing this type of sensor as they have significantly side effects on sensor sensitivity and energy transmission efficiency. Magnetoelastic thick-film sensors are structural simple and are capable of measuring multiple physical quantities, their sensitivities need to be improved. Passive SAW sensors are attractive to sensing community due to their high performance, small size and good reproducibility. A problem is the SAW propagation path can be affected by different environmental parameters. In addition, MEMS technology and its future market were also introduced. MEMS technology is widely used for a variety of applications. MEMS devices are more reliable and offer higher performance over traditional products. It is expected that the market for MEMS will reach £47.5 billion by 2010. Finally, some microfabrication techniques including anisotropic etching, electroplating, deep reactive ion etching, thick-resist moulding, silicon fusion bonding, anodic bonding, chemical mechanical polishing, evaporation and sputtering were reviewed. These techniques were used to fabricate the proposed sensors and the fabrication processes were shown in Chapter 6.

The use of thick-film magnetoelastic material for the wireless pressure sensor was presented in Chapter 3. A sensor array made of ribbon-like ferromagnetic alloy was fabricated and tested. Result shown that although magnetoelstic thick-film pressure sensor has the advantage of simplicity in its structure, it has low pressure sensitivity and the measurement can be easily affected by environmental noises. In order to detect the change of resonant frequency of the sensor, analytical instrument with much higher resolution than current device is needed.

In Chapter 4, the features of three MEMS product design software packages: CoventorWare, IntelliSuite and MEMS Pro were introduced and compared. Both IntelliSuite and CoventorWare originated from Massachusetts Institute of Technology (MIT) in the 1990s and therefore they have similar structures and functions of their modules. They all have material property databases, built-in design and simulation tools for creating fabrication process flow, mask layouts and 3D models as well as performing fabrication process check and simulation, physical-level and system-level simulation. However, during these years they have also developed their unique features. For example, CoventorWare has a module 'SEMulator3D' for helping designers to localise and classify faults and defects. IntelliSuite has a module to estimate the overall cost of the designed product and it has extended its application to NEMS. MEMS Pro was developed in Tanner Research, a company specialising in microelectronics design. As a

result, it has the advantage of integration with electronic design automation (EDA) tools. MEMS Pro is built on top of several EDA design tools such as L-Edit, S-Edit, W-Edit, T-Spice, and LVS etc. These tools are widely used in the electronics industry. This feature considerably brings down the license fee and makes it quite easy to learn for those EDA tool users.

The investigation of LC type pressure sensor was presented in Chapter 5. Two sensors were designed which use silicon and glass as the substrate materials and flat and central bossed diaphragms as the pressure sensing elements. In order to optimise the sensor performance, different types of coil layouts including loop coil, meander coil, solenoid coil, polygon spiral coils, circular spiral coil, single layer spiral coil and multi-layer spiral coil, were introduced and compared. Result shows that a single layer square spiral coil is more suitable for the inductive component of the LC resonant circuit because of the feature of MEMS fabrication process as well as the requirement from the sensor delivery procedure. Three methods for calculating the self inductance of planar spiral coils were introduced and were used to estimate the inductance of the designed square spiral coil. Results from these methods show a high degree of agreement. Among them, 'Approximation Forms' method is readily to use but is restricted to inductors with simple and regular shapes. 'Greenhouse' method can be used for spiral rectangular coils. For coils with complex and irregular shapes the 'Finite Element' method has to be used. Finally, the expected resonant frequency

changes of these two sensors in response to applied pressures were predicted. Result revealed that both sensors show relatively linear response to pressure changes and sensor with bossed diaphragm has higher sensitivity.

Chapter 6 recommended the fabrication processes of these two LC type pressure sensors. Deep reactive ion etching technique and AZ9260 thick-photoresist were chosen to form the moulds for the microcoils of the sensors. In order to acquire void-free copper tracks and to minimise the resistive losses, features of 'Copper Damascene' and 'LIGA' techniques were combined into the coils' fabrication processes. Anisotropic wet silicon etching method was used to fabricate the pressure sensing diaphragms and the final sensor structures were formed using silicon fusion bonding and anodic bonding techniques. At the end of the chapter, two detection methods, direct and wireless measurement, were performed to demonstrate the feasibility of the sensor operating principle. The result from the wireless detection method shows a maximum distance of 8cm in the air was achieved between the sensor and the reader. It was concluded that this distance may not be sufficient for implantation applications and other techniques need to be used to improve the reader system.

7.2 Research Contributions

The major contributions of this research can be concluded as follows:

- A thick-film magnetoelastic pressure sensor array was developed

successfully. The expected resonant frequency response of this sensor array was calculated.

- The features and design flows of three leading MEMS design tools CoventorWare, IntelliSuite and MEMS Pro were presented and compared in this research. Although the comparison of the first two software packages can be found in literature, it the first time to compare all these three in one research. Result shows that CoventorWare is the most used MEMS design tool among universities and industry. IntelliSuite has similar structures and functions as CoventorWare because they have the same origin. MEMS Pro is easy to learn and this is particularly true for those EDA tool users. This provides useful information for MEMS designers especially for beginners when choosing an appropriate tool for their product design.
- Two LC resonant type wireless pressure sensor were proposed. Although this kind of pressure sensor for medical implants was investigated by a number of researchers, design techniques and considerations were rarely mentioned in their reports. In this research, the whole design process and considerations associated with this process are presented. The dimensions of the coils of these two sensors were optimised in order to achieve a maximum detectable distance between the sensor and the reader.
- The effect of different types of diaphragms on the performance of an LC pressure sensor was compared in this research. Results show that the linearity of capacitance change in a sensor with a bossed diaphragm or a

sensor with a flat diaphragm is relatively poor. However, it was shown that the relationship between resonant frequency change of the sensor and the applied pressure may be assumed to be linear. This result can be used as a rule of thumb when design high sensitive LC pressure sensors.

- The Matlab programme developed in this research can be readily used to calculate the inductance of a rectangular spiral coil. It can be also used to assess the simulation result from CAD tool. However, users should bear in mind that this programme is not applicable for other shapes of polygon spiral coils such as pentagon or hexagon spiral coils. This is because any two adjacent conductor segments in these types of coils are not perpendicular and therefore the mutual inductance between these segments needs to be considered.

7.3 Future Work

Four recommendations are proposed to extend the current investigation:

Firstly, the use of magnetoelastic material for pressure sensing can be further explored. Although the idea of employing a thick-film magnetoelastic sensor for detecting the AAA sac pressure was abandoned due to the low pressure sensitivity of this sensor and the limited facilities in the laboratory, it is still possible to use magnetoelastic material to detect the pressure in a repaired AAA. Figure 7.1 suggests an alarm device which consists of a small piece made of

thick-film magnetoelastic material and is mounted on a plastic base. It is placed in a cavity which is sealed by a pressure sensitive diaphragm. This device can be delivered into an aneurysm sac during the endovascular repair. A magnetic field is generated to make the magnetoelastic part mechanically vibrate at a certain frequency. If the blood pressure inside the sac increases due to endoleaks or other causes, the diaphragm will move downwards and eventually touch the magnetoelastic piece at a specific pressure value. Then the vibration will be stopped and this change can be detected by using a microphone. By setting the distance between the diaphragm and the magnetoelastic part to a proper value, high pressure inside the repaired aneurysm sac can be alarmed in time.

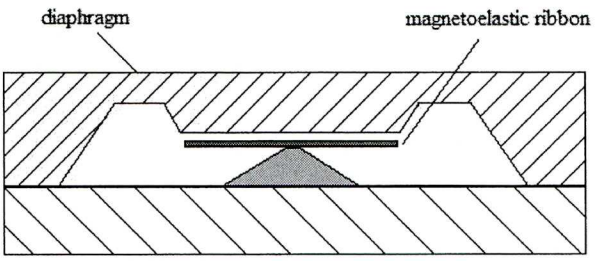

Figure 7.1 An alarm device for detecting endoleaks

Secondly, the outside shape of the two LC sensors should be optimised for the delivery. In order to protect the sensor and also the environment in which the sensor is deployed, it should be encapsulated with soft and biocompatible material such as soft silicone (polydimethylsiloxane). As the proposed sensor was designed to be delivered into an aneurysm sac with the same process as the deployment of the stent-graft or immediately after the deployment, this requires

that the sensor is provided with fixation means to the stent-graft or to the appropriate delivery system. The delivery of the sensor was beyond the scope of this project.

Thirdly, the two LC resonant type pressure sensors can be fabricated and the wireless interrogation and detection device can be set up in future work. Testing of the sensors should include environment-related effects such as temperature, liquid viscosity, distance and angular position of the sensor coil and the interrogation system coil on the sensor performance.

Last but not least the wireless detection method needs to be further explored. As concluded in Chapter 6, the detectable distance of the wireless detection device used in the pilot study may not be sufficient for this pressure sensor application. In addition, this distance was also largely affected by the alignment between the coils of the sensor and antenna of the readout device. Therefore, the improvement of the detection device would be necessary.

Previous clinical measurements of pressure in patients after endovascular aortic aneurysm repair have shown that pressure in the aneurysm sac is not uniformly distributed [Dias et al., 2007]. Therefore, a single pressure measurement at one point in the aneurysm may not provide a reliable account of the actual pressure to which the aneurysm is subjected. It would be advantageous if a multi-sensor

array could be developed which employs the same LC resonant principle and can measure pressure in different parts of the aneurysm sac. The resonant frequencies of the individual sensors of the array would have to be sufficiently far apart so that the interference does no affect the measurement.

Although the sensor is designed for measuring AAA sac pressure after an EVAR, it can be used for other applications in the body. For example, the continuous tracking of intracranial pressure for some patients with neurological diseases is necessary. A traditional pressure measuring method is to drill a hole in the skull of the patient and a pressure sensor is inserted into the skull to acquire the pressure information. The sensor needs to be fixed onto the skull and connected to an electrical reading device. This poses a potential safety hazard for the patient. Wireless sensing of the intracranial pressure would be far more advantageous and the proposed sensor is ideal for this purpose.

Reference

Dias N. V., Ivancev K., et al., Endoleaks after endovascular aneurysm repair lead to nonuniform intra-aneurysm sac pressure, Journal of Vascular Surgery 46 (2) ; 197-203, Aug. 2007.

Appendix A
Inductance Calculation of Square Spiral Coils

```
%%%%%% This programme is written for the calculation of the
inductance of a square spiral coil using Greenhouse Theory.

clear all;
format short

D1=0.503;  % the side length of the square coil, its unit is cm
D2=0.503;  % the side length of the square coil, its unit is cm
b=30e-4;   % b is the wire width, the unit is cm, equal to 30um
h=30e-4;   % h is the height of the wire, the unit is cm, equal
             to30um
x1=10e-4;  % x1 is the distance between two adjacent turns, the
             unit is cm, equal to 10um
p=x1+b;    % p is the pitch
N=46;      % N is the number of turns;

L(1)=D1-b; % the unit is cm
L(2)=D2-b; % the unit is cm


L0=0;      % the total inductance of the straight segments, unit
             is microhenry
Mnf=0;     % Mnf is the negative mutual inductance; the unit is
             nanoHenry
Mpf=0;     % Mpf is the positive mutual inductance; the unit is
             nanoHenry


%%%%%%%%%%%%%%%%%%%%%%%%%%%%%%%%%%%%%%%%%%%%%%%%%%%%%%%%%%%%%%%%%%%%%%%
%%%% the calculation of the track length

for i=3:4*N

    L(i)=L(i-2)-p;
End


%%%%%%%%%%%%%%%%%%%%%%%%%%%%%%%%%%%%%%%%%%%%%%%%%%%%%%%%%%%%%%%%%%%%%%%
%%%%% the calculation of the inductance of straight lines
%%%%% the unit of h,b,L(j) should be in centimetre
%%%%% Lz is the straight segment inductance
%%%%% the unit of Lz and L0 are in microHenry

for i=1:4*N
    Lz=0.002*L(i)*(log(2*L(i)/(b+h))+0.50049+(b+h)/(3*L(i)));
L0=L0+Lz;
end

%%%%%%%%%%%%%%%%%%%%%%%%%%%%%%%%%%%%%%%%%%%%%%%%%%%%%%%%%%%%%%%%%%%%%%%
```

```
%%%% the calculation of the negative mutual inductance

for i=1:4*N
    for j=(i+1):4*N
        if mod(j-i,4)==2      % lines which are at opposite.
                                the mutual inductance is negative;

      d1=L(i+1)-p*(j-i-2)/4; % d1 is the distance between two
                                segments;
      Lk=L(j);
      Lp=p*((j-i+2)/4-1);
      Lq=p*(j-i+2)/4;
      Lkp=Lk+Lp;
      Lkq=Lk+Lq;

      if Lkp==0
         Fkp=0;
      else
         Fkp=log(Lkp/d1+(1+(Lkp/d1)^2)^0.5)-
(1+(d1/Lkp)^2)^0.5+d1/Lkp;
      end
      if Lkq==0
         Fkq=0;
      else
         Fkq=log(Lkq/d1+(1+(Lkq/d1)^2)^0.5)-
(1+(d1/Lkq)^2)^0.5+d1/Lkq;
      end

      if Lp==0
         Fp=0;
      else
         Fp=log(Lp/d1+(1+(Lp/d1)^2)^0.5)-(1+(d1/Lp)^2)^0.5+d1/Lp;
      end

      if Lq==0
         Fq=0;
      else
         Fq=log(Lq/d1+(1+(Lq/d1)^2)^0.5)-(1+(d1/Lq)^2)^0.5+d1/Lq;
      end

         Mkp=2*Lkp*Fkp;
         Mkq=2*Lkq*Fkq;
         Mp=2*Lp*Fp;
         Mq=2*Lq*Fq;

         Mn=0.5*((Mkp+Mkq)-(Mp+Mq));  % Mn is the negative mutual
                                         inductance between two
                                         segments;
         Mnf=Mnf+Mn;                 % Mnf is the total mutual
                                         inductance of the coil;
         end

%%%%%%%%%%%%%%%%%%%%%%%%%%%%%%%%%%%%%%%%%%%%%%%%%%%%%%%%%%%%%%%%%%%%%%%
%%%% the calculation of the positive mutual inductance


        if mod(j-i,4)==0    % lines at the same side, the mutual
                              inductance is positive;

          d2=p*(j-i)/4; % d2 is the distance between two segments;
```

```
            Lk2=L(j);
            Lp2=p*(j-i)/4;
            Lkp2=Lk2+Lp2;

          if Lkp2==0
             Fkp2=0;
          else
              Fkp2=log(Lkp2/d2+(1+(Lkp2/d2)^2)^0.5)-
                   (1+(d2/Lkp2)^2)^0.5+d2/Lkp2;
          end

          if Lp2==0
             Fp2=0;
          else
              Fp2=log(Lp2/d2+(1+(Lp2/d2)^2)^0.5)-
                  (1+(d2/Lp2)^2)^0.5+d2/Lp2;
          end

           Mkp2=2*Lkp2*Fkp2;
           Mp2=2*Lp2*Fp2;
           Mpositive=Mkp2-Mp2;  % Mpositive is the positive mutual
                                  inductance between two segments;
             Mpf=Mpf+Mpositive;

          end

     end
end
L0                          % total inductance of the straight
                              segements
Mnf                         % total negative mutual inductance of
                              the coil,unit is nanoHenry
Mpf                         % total positive mutual inductance of
                              the coil,unit is nanoHenry
Ltotal=L0+2*(-Mnf+Mpf)*1e-3    % total inductance of the coil
```